

Department of Physics and Astronomy

Heidelberg University

**Master Thesis in Physics**

submitted by

**Tobias Hammel**

born in Leonberg

**2021**



**Design and Construction of a New Experiment  
for Programmable Quantum Simulation using  
Ultracold  ${}^6\text{Li}$  Fermions**

This Master thesis has been carried out by

**Tobias Hammel**

at the

**Physikalisches Institut Heidelberg**

under the supervision of

**Prof. Dr. Selim Jochim**



## **Abstract**

In this thesis, the design and the first construction steps of a new state-of-the-art experiment for programmable quantum simulation, using  ${}^6\text{Li}$  fermions, is presented. The fundamental concept is based on compactification of the vacuum set-up and its surroundings, an enhanced control over individual parts of the system and the refinement and expansion of the tool set how to manipulate lithium atoms. The goal is to achieve cycle times of below one second, being one order of magnitude shorter than in existing set-ups, as a result increasing statistics obtainable in a fixed time frame and improving the usability of the experiment. Additionally, the modular design opens the path to uncomplicated implementation of new hardware as well as an increase of complexity of the simulated physical systems in the future.

The thesis focuses on the design and set up of the vacuum apparatus and particularly the cold atom beam source as well as on the design of versatile magnetic field coils and the interplay between these components. Enabled by these improvements, the deterministic preparation of few particle quantum systems with high fidelity shall be expanded to larger atom numbers and to systems in more complex settings.

## **Zusammenfassung**

In dieser Arbeit werden das Design und die ersten Schritte des Aufbaus eines neuen und fortschrittlichen Experiments für programmierbare Quantensimulation mit fermionischem  ${}^6\text{Li}$  beschrieben. Das zugrunde liegende Konzept beruht auf der Kompaktifizierung des Vakuumsystems und der umliegenden Aufbauten, der verbesserten Kontrolle individueller Teile des Experiments und der Verfeinerung und Erweiterung von Möglichkeiten, Systeme aus einzelnen Atomen zu präparieren. Das Ziel dieser Weiterentwicklung ist die Beschleunigung eines experimentellen Zyklus um eine Größenordnung auf unter eine Sekunde, um dadurch höhere Statistik und eine verbesserte Benutzbarkeit des Experiments zu erreichen. Außerdem bietet dieses Design eine modulare Basis, um durch zusätzliche Teile und Erweiterungen und eine dadurch erhöhte Steigerung der Komplexität der simulierten physikalischen Systeme, in Zukunft freies Entwicklungspotential und flexiblen Einsatz verschiedener Subsysteme zu ermöglichen.

Der Hauptfokus dieser Arbeit liegt auf dem Design und der Konstruktion des Vakuum Aufbaus und insbesondere der Quelle der vorgekühlten Atome, sowie den Magnetfeldspulen und dem Einfluss der verschiedenen Teile untereinander. Damit soll die deterministische Präparation von Wenig-Teilchen Systemen mit hoher Güte auf größere Atomzahlen und auf Systeme in komplizierteren Umfeldern erweitert werden.

# Contents

<b>1</b>	<b>Introduction</b>	<b>1</b>
1.1	A brief history of computation . . . . .	1
1.2	Moore's law . . . . .	3
1.3	Programmable Quantum Simulation . . . . .	4
<b>2</b>	<b>Experimental set-up</b>	<b>7</b>
2.1	Overview over the system . . . . .	7
2.2	A global coordinate system . . . . .	10
2.2.1	Mounting and tilt adjustment . . . . .	11
2.2.2	Linear translation stage . . . . .	13
2.3	The vacuum components . . . . .	15
2.4	Construction . . . . .	23
2.4.1	Vacuum Cleaning . . . . .	24
2.4.2	Mechanical set-up . . . . .	26
2.4.3	Bake out . . . . .	27
2.5	The experimental set-up . . . . .	28
<b>3</b>	<b>Magnetic field coils</b>	<b>31</b>
3.1	General principles of coils . . . . .	31
3.2	Requirements on the coil design . . . . .	34
3.2.1	Magnetic field range . . . . .	35
3.2.2	Temperature stability . . . . .	36
3.2.3	Switching times . . . . .	37
3.2.4	Curvature control . . . . .	38
3.3	Features of the design . . . . .	39
3.3.1	Hollow core wires . . . . .	39
3.3.2	Center tap . . . . .	40
3.3.3	Jumping coils . . . . .	41
3.4	Design of first generation magnetic field coils . . . . .	42
3.4.1	Determination of mechanical parameters . . . . .	42

3.4.2	Theoretical performance . . . . .	46
<b>4</b>	<b>The 2D-MOT - A compact cold atom source</b>	<b>49</b>
4.1	Theoretical background . . . . .	50
4.1.1	Atom-Light interaction . . . . .	50
4.1.2	The Magneto-Optical Trap . . . . .	54
4.2	2D-MOT simulations . . . . .	57
4.2.1	Basic principles of the code . . . . .	58
4.2.2	Critical velocity . . . . .	59
4.2.3	Influence of the MOT beam power . . . . .	60
4.2.4	Influence of the push beam . . . . .	63
4.2.5	Conclusions for the design . . . . .	64
4.3	Set-up of the 2D-MOT . . . . .	66
4.3.1	Optical Bow-Tie configuration . . . . .	66
4.3.2	Laser system TA-SHG . . . . .	68
4.3.3	Optical diffuser . . . . .	70
4.3.4	Imaging . . . . .	72
4.3.5	Magnetic quadrupol fields . . . . .	73
<b>5</b>	<b>Conclusion and Outlook</b>	<b>75</b>
5.1	Conclusion . . . . .	75
5.2	Outlook . . . . .	76
5.2.1	Magnetic field coils . . . . .	76
5.2.2	RF and Microwave antennas . . . . .	76
5.2.3	SHG Laser set-up . . . . .	77
5.2.4	532 and 1064 nm laser systems . . . . .	77
5.2.5	Optical modules . . . . .	78
5.2.6	High-NA objective . . . . .	79



# 1 Introduction

In this thesis, the general idea and design process of a next generation quantum simulator, built at Heidelberg university in the framework of the Heidelberg Quantum Architecture project (HQA), is presented. The design of this new apparatus evolves around the vision of implementing the already existing knowledge on deterministic quantum simulation with Lithium-6 fermions into one compact, modularly expandable and fast machine. To achieve this, every part of the machine is designed in a way that enables best performance and speed, with the goal to surpass current limitations, while keeping the range of physics the machine shall be able to simulate as large as possible. However, highest level performance and large versatility are normally mutually exclusive requirements to a system as improvements are typically gained by increasingly specializing all parts of the system to perform one task optimally, at the cost of performance in other tasks. To circumvent this, all parts of the experiment are planned to be as decoupled from each other as possible and are optimized individually. Therefore, limitations in possible designs for one part, imposed by already made design choices, occur only late in the design process. Hence, it serves as an optimized and completely characterized basis, which allows to freely add specified parts to. It turns out that a vital point to make the idea work, is the ability to fully characterize the system and the influence the decoupled degrees of freedom (DOFs) have in the optimization process. With this approach to the setup of a new apparatus the goal is to make a large step towards easily usable, programmable quantum simulation.

## 1.1 A brief history of computation

Since the end of the 19th century, there has been a steady growth of the power and availability of computers of any kind or form up to the point at which they are not replaceable in daily lives anymore. The progress started with simple mechanical engines like the ones of Leibniz [1] or Babbage [2], which were able to perform simple calculations like sums, differences, multiplications and divisions. Elaborating on these engines, Konrad Zuse built a machine running on boolean logic, which was

controllable via punch tapes making it the first programmable computer. The size of such computers was massive compared to today's computers at weights of over 5000 kg of for example the "Mark 1" built by Howard Aiken and collaborators at Harvard university. However, a large team of trained staff was required to run the machines as they had to be rewired constantly to perform different kinds of calculations. As a result, they were quite susceptible to human errors and to natural errors like a moth flying and dying inside the huge machine disrupting the electronics and causing the first ever reported "computer bug".

The change in design to use vacuum tubes to run the computer on a fully digital basis of binary math increased on one hand the calculation capabilities of the computers tremendously, however on the other hand it did not decrease the amount of people needed to maintain it nor did it decrease its size. The computers at that time were not scalable or easy to use, but showed the supremacy of a new tool to solve tasks, which were previously not solvable. Thus, they opened up a field of new ideas and goals, which could come within reach, if the calculation power of the machines was improved. In fact, they acted as a stepping stone for the later innovations by proving the general concept and value of the new tool set.

The essential step towards today's understanding on what a computer is has been done only about a decade later in 1947 when the first transistor was built by John Bardeen and Walter Brattain in the group of William Shockley at Bell labs [3] what they were awarded the Nobel prize in 1956 for. Transistors enabled the design of far more powerful and complex computers, while reducing their size and power consumption by many orders of magnitude. The small size and lower need of maintenance started the development of the first high-level computer languages. Because of the development of compilers, it was not necessary anymore to write computing tasks in machine language or with punch cards, but one was able to write code in the way it is done today. Consequently, compilers paved the way to modern elaborated programming languages. This development also sparked the possibility to interconnect different systems, make their abilities and results comparable and apply improvements done in one system to another.

The last big revolution in this brief timeline is the implementation of transistors into integrated circuits by Jack Kilby [4]. By putting a large number of transistors together onto one board, not having to solder every transistor connection individually, the susceptibility to errors reduced and scalability and economical accessibility greatly increased. An exponential increase in the number of transistors implemented on one chip was the result, effectively reducing the chip size while getting increasingly more powerful. This led Gordon Moore, former Co-Founder of Intel, to formulate a

prediction for this growth, which today is known as Moore's law [5].

## 1.2 Moore's law

In 1965, Gordon Moore published the prediction that the number of transistors on an integrated circuit chip doubles approximately every two years. The trend showed to very precisely match the growth up to this point and still qualitatively fits the developments until today. However, the meaningful aspect is not the good agreement of prediction and data, but the effort put into the development of new techniques to continue achieving this growth. One can imagine the challenges faced in an intuitive way. For transistors to be packed denser and denser onto a chip the transistors themselves have to get smaller and smaller. Therefore, the fidelity of machines has to be high, down to progressively smaller size regimes. Such improvement comes to its limits when the size of features of the integrated circuits becomes small enough for quantum effects to play a role. In this limit, a normally closed gate of a transistor cannot certainly be thought of as closed as electrons have a non-negligible probability to tunnel through the barrier. This poses a fundamental limitation to how dense integrated circuits can become and is one reason why Moore's law started to evolve from a doubling every two years to a doubling every three years in the recent past. Another critical point is to realize that innovation will typically only occur if there is a demand for it. In the case of Moore's law this demand is fairly obvious, as in every part of daily life a faster computer, a larger memory or a more matching suggestion for another sweet cat video is wanted. A little more intricate are the reasons for science to demand increasingly strong computers. The reason is that, although the capabilities of computers rise exponentially, the difficulty of problems scientists want to solve rises exponentially, too. An example is an ensemble of  $N$  indistinguishable fermions on a lattice. To describe the spin wavefunction of one single fermion, two coefficients have to be stored, one indicating the probability to be in the spin up state and one to be in the spin down state. If now a second fermion is added there are four combinations the two spins can realize and there are eight possible states for 3 fermions. In general, there are  $2^N$  coefficients needed to fully characterize the wavefunction of a system of  $N$  fermions. An example: If one would try to print out all coefficients to describe a system of 100 fermions on DIN A4 70  $\frac{\text{g}}{\text{m}^2}$  paper, font Arial 11pt and printed on both sides about  $1.26 \cdot 10^{27}$  pages would be needed. These would stack up to a tower of a height easily reaching beyond the nearest galaxies and would have a weight of about the mass of the earth. Even by using more advanced ways to store data, millions of yottabytes would be needed, which is trillion times the estimated total amount of data stored in the world today. Hence, it is an impossible

challenge to describe such a system classically, but even with the strongest computers the memory consumption would surpass all accessible hardware. Importantly, this is only for a lattice with  $10 \times 10$  lattice sites. Accordingly, there is an urgent need to analyse quantum mechanical systems in a more efficient way than by brute force calculation on classical computers. The central point connecting to this thesis is to realize that systems of that size are already in reach for cold atom experiments. These can hence act as a stepping stone to open up new ideas and goals, how different parts of physics can be explained, and lead to innovations on their own.

Such systems are also of particular interest, because they are in the crossover from simple, well understood systems, like single atoms or electrons, to macroscopic systems of thousands and millions of interacting particles. Often large systems can be explained quite well in an approximate way in for example mean-field theories, but if these approaches fail, it is difficult to deduce the reason from the well-behaved single particles for the large systems without having knowledge about the crossover regime. To surpass the classical calculations there are two promising approaches:

Firstly, there is the idea to replace transistors by so called qubits, which can be in a quantum mechanical superposition of 0 and 1 and are quantum mechanically entangled with all other qubits. Building qubits in a way that the calculations run on a high fidelity needed for computation is, however, a highly involved task and a lot of effort is put into so called "quantum computation" [6][7].

The second approach to the problem is also the approach this thesis is embedded in. The idea has first been proposed by Richard P. Feynman [8] and is known as "quantum simulation". The key difference to the first approach is that there is no digital computation done, but the system of interest is imitated by a similar, well controlled system. From these simulations one can indirectly draw conclusions about the real system, which is often experimentally hard to access.

## 1.3 Programmable Quantum Simulation

In the approach to quantum simulation presented here, real physical systems are simulated with the help of individual atoms captured inside a vacuum chamber by using optical and magneto-optical traps.

At first sight, it is non-intuitive to see why  ${}^6\text{Li}$  fermions interacting in some optical potential landscape of laser light inside a vacuum chamber should be connected to, for example, the behaviour of electrons in a solid piece of metal. Only on a second look it becomes obvious that, although scales might be very different, the way these systems behave and evolve in time is fully determined by their Hamiltonians. Therefore, it is reasonable to think of systems, which are described by similar Hamiltonians, to be

comparable and to draw conclusions from one to another. Cold atoms in particular offer a very clean and versatile system for simulations, because of the high fidelity control of the atoms and the large tunability of parameters in the Hamiltonian. Examples of parameters are the contact interaction strength between the atoms, which can be set via Feshbach resonances, or the exact optical potentials the atoms are located in. The range of physical systems, which can be explored with cold atoms, is therefore inherently very broad.

When designing a new experiment normally the first question, which has to be answered is what scientific problem shall be addressed and its means for the design itself. For example, if one wants to investigate superconductivity one has to think about the materials of interest and how far they have to be cooled to become superconducting. Probing the Quark-Gluon-Plasma at the center of the early universe on the other hand probably requires the need to get funding to build a 27 km circumference particle accelerator. In the case of cold atom experiments there are however different ways to start a new design. Either, the system, which shall be simulated and the challenges to do so are known. Hence, the design has the goal to realize this particular system and similar systems closely connected. Or, in contrast to building up the real system to probe it, for quantum simulators the exact physical system of interest does not necessarily have to be known. Only an idea of what tools are needed to access certain regimes in the broad range of physical systems of interest is required. Examples of tools might be a particular laser or magnetic field coil design, but also optical access in certain angles or at the very basis the selection of the atomic species used. In such an approach more abstract goals have to be set to guide the design process.

These two approaches have a strong parallel to early stages of computer construction summarized in Section 1.1. The first computers were built with the idea to solve a certain task and were difficult to re-program for another task. However, after the supremacy of such machines was demonstrated, tools were developed, which made computers more powerful and in particular easily programmable. This paved the way of the transition of computers to versatile machines with nearly unlimited possibilities. Similarly, this new experiment does not have the simulation of one system or a cluster of systems as its goal, but the implementation of a variety of optimized and modularly exchangeable tools to make quantum simulation more easily re-programmable. This then offers the possibility to interface the quantum simulator via a high-level language, enabling a direct programming of the Hamiltonian onto the atoms without deep knowledge about the mechanical system itself, which would be comparable to the state classical computers are in currently.

### 1.3 Programmable Quantum Simulation

---

The goals for the design of the new experiment are to increase the cycle rate of the realization of one simulation, in other words one computation of a complex quantum mechanical system, to above 1 Hz, to increase feedback rates, simplify debugging and generally decrease "computation" times. Further efforts shall be put into the design of characterization tools to feedback into the system and allow on the run adjustments or remote debugging and optimization. On a longer timescale, a programming interface for the basic preparation steps like loading and cooling the atoms to some particular state shall be implemented.

## 2 Experimental set-up

In this chapter the experimental set-up and in particular the design and construction of the vacuum apparatus is presented. The underlying concepts the design addresses are compactness and the ability to achieve an ultra-high vacuum (UHV) in the glass cell. For this purpose, the vacuum is split in a high vacuum (HV) section to which the oven is attached and an UHV section at the position the quantum simulation will take place by implementing a differential pumping stage (DPS). For HV and UHV section final pressures of  $\sim 10^{-9}$  mbar and  $\sim 10^{-12}$  mbar are the goal, respectively.

### 2.1 Overview over the system

In the introduction, the need to surpass current abilities of classical computers in solving quantum mechanical problems was explained. "Quantum simulation" is one promising candidate for this task. First, the exact terminology what quantum simulation means in the context of this thesis is introduced.

The apparatus will be a quantum simulator for strongly interacting Fermi gases of  ${}^6\text{Li}$  atoms in reduced dimensions. In particular, one-dimensional (1D) and two-dimensional (2D) systems of few fermions in different hyperfine states are of interest. Additionally, more complex settings like a 2D lattice potential or the deterministic assembly of exotic geometries from single optical tweezers, like a  $2 \times 2$  lattice with tunable tunnel couplings between all sites, shall be possible. Furthermore, the use of bosonic  ${}^7\text{Li}$  and even the simultaneous preparation of both isotopes in one systems will be, in general, in reach for the apparatus. In all cases, an imaging procedure with single-atom resolution is required and will be implemented.

To make a versatile quantum simulator work, many requirements have to be met. For the results of a simulation to be meaningful, i.e. comparable to the real system it shall simulate, an exceptional level of control over the atoms is required. Consequently, sophisticated tools are necessary which range from lasers at different wavelengths to magnetic field coils or high fidelity detection set-ups. In general, the basis for any quantum simulation experiment to work reliably is the decoupling from

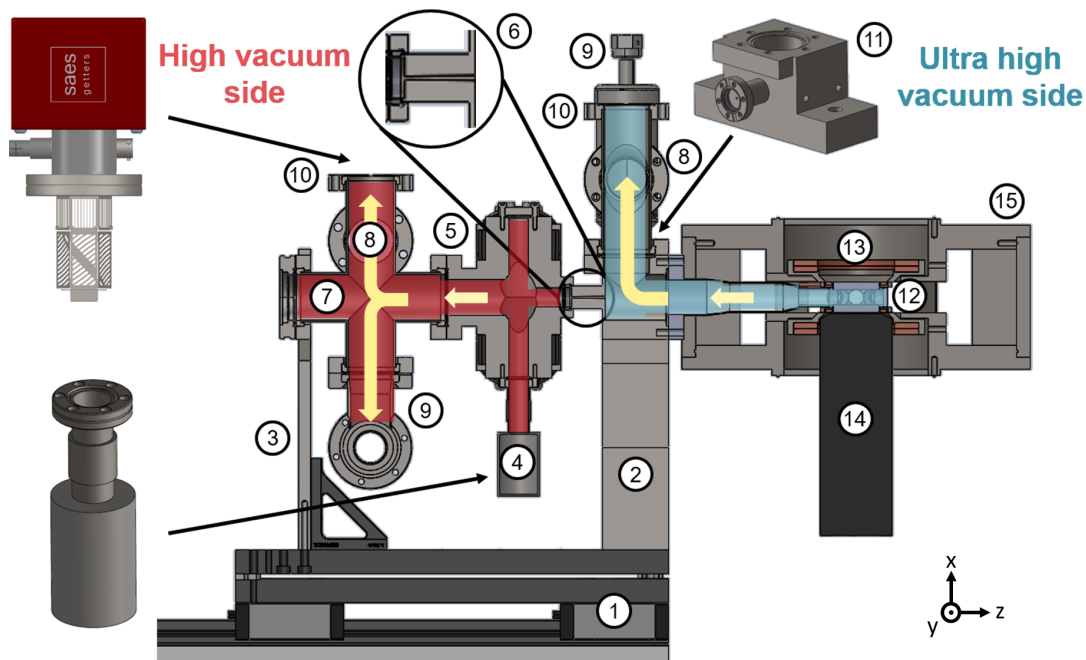


Figure 2.1: A cut-through of the final vacuum design of the HQA experiment. In red the HV section and in blue the UHV section are indicated, respectively. The yellow arrows show the gas flow, while pumping down the vacuum.

the outer world. Reason for that is it ensures all physical conclusions, drawn from the simulation, stem exclusively from the well-controlled atoms and not from unknown influences from the outside. One example for this separation is that the atoms are prepared in a ultra-high vacuum to avoid collisions with other atoms which would effectively destroy the prepared quantum mechanical state.

In the following the apparatus designed to fulfil these goals and requirements is described as well as the general purpose of the different components. Afterwards, the individual components are described in detail. In Fig. 2.1 a cut through the experiment is shown, including all parts to build up a system for versatile quantum simulation.

To outline the purpose of the different components (1) to (15) in Fig. 2.1, one typical experimental cycle is summarized. A quantum simulation cycle starts with the lithium atoms being evaporated from the oven (4) and flying vertically up into the 2D-MOT chamber (5). In the chamber a pressure of around  $10^{-9}$  mbar is maintained constantly. To initially pump down to this pressure regime a turbomolecular pump is connected to the system via an all-metal valve (9), which can be closed after bake-out (see Section 2.4.3). During operation, the residual gas atoms as well as contaminations leaving the oven are pumped by an Ion-Getter pump (10). The pressure is monitored by a high-vacuum gauge (8). These components are connected

to the 2D-MOT chamber via a 5-way cross (7). The remaining arm of the cross on the left hand side in Fig. 2.1 is sealed using a viewport to provide optical access to the 2D-MOT chamber on this axis. In the final set-up the position of (8) and (9) has been switched due to space restrictions.

After being evaporated from the oven, the lithium atoms which enter the 2D-MOT chamber are exposed to laser radiation effectively cooling them in the x-y-plane (the coordinate system is shown in Fig. 2.1). As a result, the atoms seem to make a turn of  $90^\circ$  to the right leaving the 2D-MOT chamber along the z-axis. The probability to leave the chamber to the left is suppressed by shining in a laser from this direction through the viewport attached to the 5-way cross. This laser beam is called "push beam" as it pushes the atoms in the direction of the glass cell (12). Hence, the atoms fly through the differential pumping stage (6) into the glass cell (12) in which they are recaptured in a 3D-MOT. In the glass cell the quantum simulation, including deterministic preparation of a quantum mechanical state as well as probing this state by taking an image, is performed.

In the glass cell a vacuum of  $\sim 10^{-12}$  mbar is present. To achieve such low pressures the same components like on the HV side are required. The reason for the lower pressures in the UHV section is that there is no load like on the HV side (contaminations from the oven) due to the low conductance of the DPS. The parts (8) - (10) are connected to the system via a custom designed connector (11) to which a regular 4-way CF cross is attached. The all-metal valve (9) and the gauge (8) are connected to the cross from the sides (in positive and negative y-direction) and the Ion-Getter pump (10) from the top.

The apparatus itself is mounted on a linear translation stage via two plates (1) which enable precise angle adjustments. The connection to the vacuum system is done at two points: A massive mount (2) to which the connector (11) is screwed and a V-mount (3) which one arm of the 5-axis cross is clamped onto.

Lastly, a preliminary overview of the surroundings of the scientific chamber, i.e. the glass cell (12), is given. To provide magnetic fields for MOT loading and control of the atoms, coils (13) will be set up around the cell. From below, a high NA objective (14) will be attached with a distance of about 1 mm to the lower viewport of the cell. All surroundings of the glass cell, including all optics to prepare MOT and dipole trap beams, will be mounted to an octagonal support structure (15) to interface them to the glass cell.

In the following, the different parts of the system are described in detail.

## 2.2 A global coordinate system

In the spirit of making the experiment compact and modular, it is necessary to think about how to mount the vacuum chamber as well as how to measure its exact final position. Because in order to place modular, pre-aligned optics or coils around the vacuum set-up there has to be a stable interface between module and chamber. The most elegant approach is to define the expected final position of the atoms, i.e the center of the glass cell (see Section 2.3), as the origin of a global coordinate system. The corresponding axes are defined along the atom beam axis, along the high NA objective axis and through the orthogonal viewports of the glass cell. This approach of defining the absolute positioning of all components is different to an approach of matching all laser beams and magnetic fields only relative to each other, therefore only controlling the relative position of the components. An advantage of the former one is that measurements at different points can easily be propagated throughout the system and debugging can be done independently between different parts of the system. Here, an overview of different measurements necessary to fully characterize the system is given:

- **Position** of modules with respect to the glass cell.
- **Tilt** with respect to the glass cell and the optical table.
- **Wavefront** of a laser at all interfaces between modules and between modules and the vacuum apparatus.
- **Magnetic field** in all three spatial directions.
- **Vacuum pressure** in the HV and UHV section.
- **Temperature** of critical components like the magnetic field coils.

As a result of a thorough characterization, modules can be taken out of and put into the system again without realigning them, as long as position and tilt of the module and wavefront of the laser are the same again. Furthermore, for each module an internal alignment is possible by measuring the wavefront of a laser at the in- and output of the module, instead of taking pictures of the influence of the internal alignment steps on the atoms. Hence, a differentiation between the influence of internal alignment within the module and interfacing of the module to the vacuum chamber is possible. This accelerates the feedback rate for debugging and alignment procedure tremendously and disentangles the degrees of freedom for aligning the individual parts of the experiment. The disentanglement is a crucial point if one wants

to automate the alignment of the system in the future.

To realize such control over a system there has to be a possibility to fix the position of components with respect to the vacuum system up to high precision. For this, interfacing via flexure hinges in the style of [10], via micrometer screws or spacers fixing the position can be thought of. It is probable that it will not be possible to completely passively align all optics around the glass cell due to tolerances in the manufacturing process, which are typically on the order of some tens of  $\mu\text{m}$ . Therefore, it is required to have internal DOFs inside a module to fine-tune its alignment, if the manufacturing tolerances show to be limiting. Nevertheless, this enables the connection of the measurements done inside the module with the global coordinate system, meeting the goals set for the design.

As already mentioned, the disentanglement of DOFs is an essential part to make modular design work and the first point at which this issue is addressed is for designing the mounts of the vacuum cell.

### 2.2.1 Mounting and tilt adjustment

To properly mount the vacuum system one has to make sure not to introduce tension into the system. This is of importance, because tension will always have the largest influence on the weakest part of the mechanical set-up. In case of the vacuum apparatus the weakest or most critical links are the connections of two flanges, i.e. the copper gaskets, and the thinnest walls. These parts are the most probable to crack if large tension is applied or, if they do not crack, to become leaky. Therefore, the mounting is done in a way that the system is fixed in a completely relaxed state. In Fig. 2.2 the mounting set-up of the vacuum is shown. It consists of the base plates which are connected by horseshoe-shaped spacers of variable height, a massive mount on the right and a thinner mount (so called V-mount, due to the V-shape on top) on the left hand side, right angle brackets to support the V-mount at its base, a clamp to fix the vacuum to this mount and small wedges made from Teflon (not shown in this picture) to support the vacuum flange set onto the V-mount.

To fix the vacuum to the mount, the connector of 2D-MOT and glass cell is screwed onto the mount on the right hand side. This defines the anchor point of the whole set-up!

To ensure to not put tension into the system, the assembly of 5-way cross, 2D-MOT chamber and connector is first screwed down on the right hand side and then not directly fixed on the V-mount, but before a gauge indicator which can detect very small vertical displacements is put on top of the push beam viewport flange. Then, the wedges are pushed below the flange, until the indicator shows a signal. Hence,

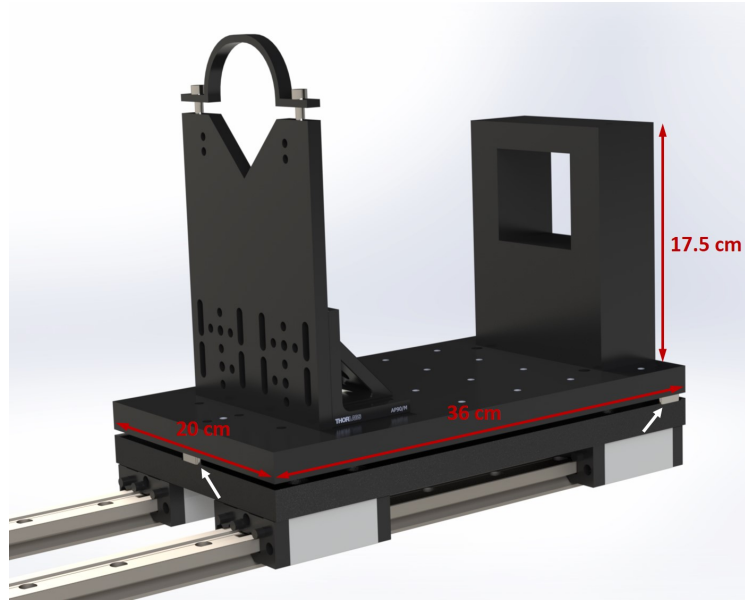


Figure 2.2: The vacuum mounts. The size of the base plates is 36 cm x 20 cm and the mounts are 17.5 cm high. All parts are made from anodized aluminium. The two base plates are connected via three horseshoe shaped spacers used for tilt adjustment. Their position is indicated by the white arrows. The whole ensemble is mounted on a translation stage.

it is ensured that the system is supported in the configuration where it has the least tension.

The system is mounted on two separate plates to enable very precise tilt adjustments. This adjustment is done by small spacers of different heights, ranging from 5 mm up to 5.2 mm in steps of 20  $\mu\text{m}$ . The spacer locations are distributed such that there are two near to the glass cell (on the right hand side in Fig. 2.2) and one on the far left. Distributing it like this makes the system as stable as possible at the position of the large mount, which acts as the anchor point for the system. The number of spacers is set to three as three points fully define a plane and adding more spacers would over-define the system.

By using different height for the pair of spacers on the right compared to the single one, a tilt in direction of the long axis of the plate, i.e. around the y-axis, is achieved. The resolution of the tilt adjustment is 0.06 mrad at a full tuning range of  $\pm 3$  mrad, which follows directly from the position of the spacers on the plates and the step size of their thickness. To also adjust the tilt in the short axis direction (around the z-axis) one can change the spacers on the right side. To decouple both angles however, it is necessary to always subtract the width of one of the spacers when adding it to the other. For example, when putting in a 5.1 mm + 40  $\mu\text{m}$  spacer on the one side,

a 5.1 mm - 40  $\mu\text{m}$  spacer has to be put on the other position. Otherwise, the plate would not only tilt along the short axis, but also in the long axis direction. As a result, the resolution is slightly reduced to 0.23 mrad at a full range of  $\pm 2.9$  mrad. The tilt adjustments is important to match the coordinate system, chosen as the global coordinate system, with the one given by the optical table. This is done using 3-axis acceleration tilt sensors [9] to measure the relative tilt of glass cell and optical table and then set it to zero using the spacers. The knowledge about this matching allows to conclude from tilt measurements done on the table to the tilt with respect to the glass cell and other parts of the vacuum set-up. For example, a measurement of beam angle and position on the table can directly give information about the beam angle and position at the position of the atoms inside the vacuum cell. In general, this fine adjustment DOF is needed as the tolerances of machined parts is always much larger than the those allowed by optical components. Therefore, as one does not know how well the vacuum parts are machined, a tuning knob for compensation of machining inaccuracies is required.

With the same argumentation of propagating measurements throughout the system, this allows for the design of powerful optical modules (see Section 5.2.5) which can be put together on the table and still have a fixed orientation with respect to the glass cell. Each of the modules can be described as a "Black Box" or "Look-up table" connecting the systems input and its output without caring about anything happening in between. This offers a versatile tool to interconnect separately built modules with one another, while still passively matching them to the vacuum hardware used.

## 2.2.2 Linear translation stage

Another fundamental design choice made for the experiment is the use of a linear translation stage (LTS), the vacuum system is built onto. The LTS offers the possibility to separate the vacuum and most importantly the glass cell from the optics and coils built around it, yielding advantages, when having to re-bake (see Section 2.4.3) or modify the vacuum, as it can be done without having to disassemble the optical set-ups. Additionally, by taking the glass cell out of the optical assembly built around it, the space at which usually the atoms are located is available to do measurements. Therefore, one can do measurements of the magnetic field or optical potentials directly at the position of the atoms. Hence, a direct measurement of important experimental quantities instead of indirect measurement, detecting the influence on the atoms, is possible. Doing direct measurements to optimize the alignment of the system increases the ability to find a global optimum in the phase space of all tunable experimental parameters, as it yields the possibility to start with the

optimization at the theoretically ideal position in configuration space. A slight optimization can still be necessary due to some unknown variables, but it shouldn't be far away from the theoretical optimal configuration. Consequently, it prevents the alignment to gradually worsen when the system is iteratively re-aligned from time to time, acting as a probe for the modular optical systems described earlier. For example, if the beam angle and position at the atoms position drifts over time, instead of re-aligning the system to compensate for the drift, one can detect the deviation from the optimal configuration, by measuring the wavefront at every interface, and propagate it back from module to module until finding the unstable part. In this manner, instead of spending time to optimize the influence of the system on the atoms, the time is used to optimize the system itself and by this automatically the performance of the experiment.

It is clear that putting the experimental apparatus on a movable stage yields powerful advantages compared to mounting it at one fixed position. However, there are some requirements the LTS has to fulfil in order for these advantages to actually be of use, in particular a high degree of stability and repeatability. Stability means that when the LTS is in a final position and locked, there are no long term drifts which would influence the alignments of vacuum and optics. Repeatability means that when pulling the vacuum out and putting it back in it will be located at the same position again. In other words, by taking advantage of the features of the LTS the alignment of vacuum and optics is not harmed. Quantitatively, the repeatability should be much better than the fine tuning range of the spacers to always be able to adjust the system back into the same configuration.

In the set-up a linear translation stage by Igus<sup>®</sup> is used [11]. It has the main advantage of not using lubricants, but using specific sliding bearings, that are lubricant free. The "dry" usage explains the name of the system, DryLin<sup>®</sup> T. One of the carriages (four are used in this set-up) can carry up to 1000 kg and withstand torques of  $> 50 \text{ Nm}$ . As the experiment is small and light and fairly symmetrically built, reducing the amount of torque onto the bearings, the pure force onto the bearings is of no concern. To make sure the bearings of the carriages on the two rails (two carriages on each rail) do not get stuck if the rails are slightly off-parallel to each other, the bearings on one rail are floating. The carriages can get heated up to  $90 \text{ }^\circ\text{C}$ , which has to be taken into account when baking the vacuum.

Before using the LTS, it has to be confirmed that it fulfils the requirements on stability and repeatability. To ensure stability, long term measurements will be carried out. For the time being, the experiences of Jendrzejewski et al. [12][13] which state that there has been no issues with the LTS for many years regarding stability suggests

	H <sub>2</sub>	H <sub>2</sub> O	CO	N <sub>2</sub>	CH <sub>4</sub>	Argon
Z100	150	100	75	40	15	6
Z200	290	180	140	80	15	6

Table 2.1: The Pumping speed in l/s for the Z100 and Z200 NexTorr Ion-Getter pumps, implemented on the HV and UHV side of the differential pumping stage, respectively. Data taken from [14].

that it is usable also in this set-up. After setting up the LTS, repeatability measurements have been carried out by sliding the carriage with the attached mounting plates away and back to a fixed stop and then measuring the deviation of the position of a collimated laser beam on a wall 4 m away. It has been found that the deviation is smaller than 1 mm (resolution of the measuring device), which corresponds to a repeatability, regarding the angles, of lower than 0.25 mrad. As the angles have to be fixed to better than 0.3 mrad, due to the sensibility of the high NA objective, this LTS seems to be a good fit. It should be noted however that if at any point the translation stage seems to limit the stability of the experiment it can be easily removed. Also, to further increase stability and repeatability it has been suggested to clamp down the carriages to a fixed stop in the final position.

## 2.3 The vacuum components

After the general concepts of how to mount and characterize the vacuum system has been introduced in the previous section, in the following the different vacuum components are introduced.

**Ion-Getter pumps** To ensure a vacuum required to do quantum simulation, while still reducing the size of the experiment, Ion-Getter pumps by SAES are used. In particular, the NEX Torr Z100 and NEX Torr Z200 [14] are used on the HV and UHV side of the vacuum, respectively. The Z200 pump is shown in Fig. 2.3. These machines combine a sputter ion pump and a non-evaporable getter pump into one compact and efficient engine with high pump speed for various gases. The pumping speeds can be found in Table 2.1. For long pumping times, the main load during the bakeout will be hydrogen outgasing from the stainless steel walls. For hydrogen the NEX Torr pumps have a particularly high pumping speed of 150 and 290  $\frac{1}{s}$  for the Z100 and Z200, respectively. All gases which cannot be gettered i.e. which do not stick chemically to a getter surface, like for example noble gases, are pumped by the ion pump.

These pumps are also comfortable to use as they only weight about 2.2 kg and are connected to the system via a CF40 flange making the apparatus a lot smaller compared



Figure 2.3: The Z200 NexTorr Ion-Getter pump. The getter element below the CF40 flange is inserted into the vacuum system when assembled. It is shaped in a way to have as large of a surface area as possible to optimize pumping rates.

to e.g. Titanium-sublimation pumps. One requirement of the pumps is that the getter element has to be mounted pointing downwards as otherwise it would start bending when heated up during the activation of the getter elements at  $\sim 500^\circ\text{C}$ . This poses some limitations to the design, but is still easily implementable. The large pumping speeds suggest that it might be possible to use smaller pumps which are mounted on a CF16 flange making the system even smaller. This can be a consideration for future upgrades.

**Ultra-high vacuum gauges** In the spirit to monitor and control all critical parameters of the system to fully characterize it at any point in time, also the pressure in the HV and UHV section of the vacuum has to be monitored. At pressures below  $10^{-11}$  mbar this poses actual difficulties. There are only very few vacuum gauges that can reliably measure down to those pressures. For this experiment the IONIVAC IE414 and 514 sensors by Leybold GmbH are used [15]. In Fig. 2.4 a) the IE414 gauge is shown. In the top part of the picture there is a small cage with an electrode used to measure the amount of residual gas molecules. The gauge is connected via a feed-through CF40 flange to the 5-way cross on the HV side and to the 4-way cross on the UHV side. A picture of the gauge in the experiment is shown in Fig. 2.4 b). The pressure ranges these gauges can measure are  $2 \cdot 10^{-11} - 1 \cdot 10^{-2}$  mbar for the

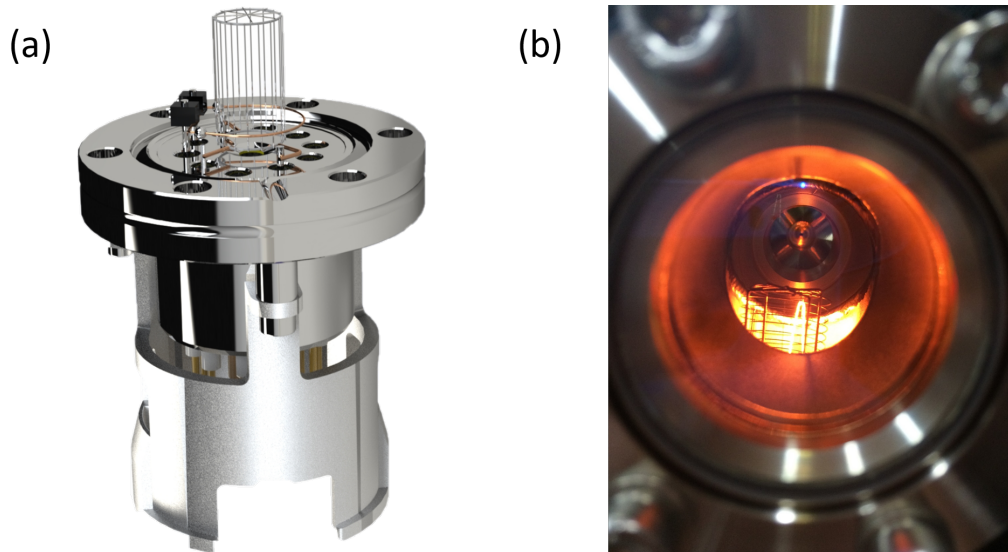


Figure 2.4: a) The IE414 high-vacuum gauge. The small cage on top contains an electrode a high voltage is applied to ionizing surrounding atoms which hence can be detected. b) A picture taken through the push beam view-port. One can see the glowing electrode in the foreground and smaller in the background the differential pumping stage.

IE 414 sensor implemented in the HV section and  $2 \cdot 10^{-12} - 1 \cdot 10^{-4}$  mbar for the IE 514 sensor implemented in the UHV section. In particular, the reliable measurement range down to  $10^{-12}$  mbar is important. Having trustable gauges on both sides of the DPS proved to be helpful in locating leaks as well as controlling the different stages in the baking process.

**Oven** The starting point of every experimental cycle is to evaporate lithium atoms from the oven. However, the oven in this experiment is only a small bucket made from stainless steel connected to the 2D-MOT chamber from below via a small tube and a CF16 flange (see Fig. 2.5 a)). In the small bucket the lithium is heated to approximately  $350^\circ\text{C}$ , leaves the bucket after evaporation through the tube and enters the 2D-MOT chamber. The exact dimensioning of the different parts of this otherwise simple object determines the flux distribution of the outgoing lithium as well as the total amount of lithium leaving the oven. It is important to realize that the oven is close to the 2D-MOT and the optics surrounding it and poses a strong source of heat which can affect the system either by heat flowing onto the vacuum system over the tube or by radiating the heat away possibly leading to thermal lensing effects on the MOT beams.

Therefore, the final oven design has to factor in the desired amount of lithium leaving it per second and its spatial distribution, the life time until lithium has to be refilled

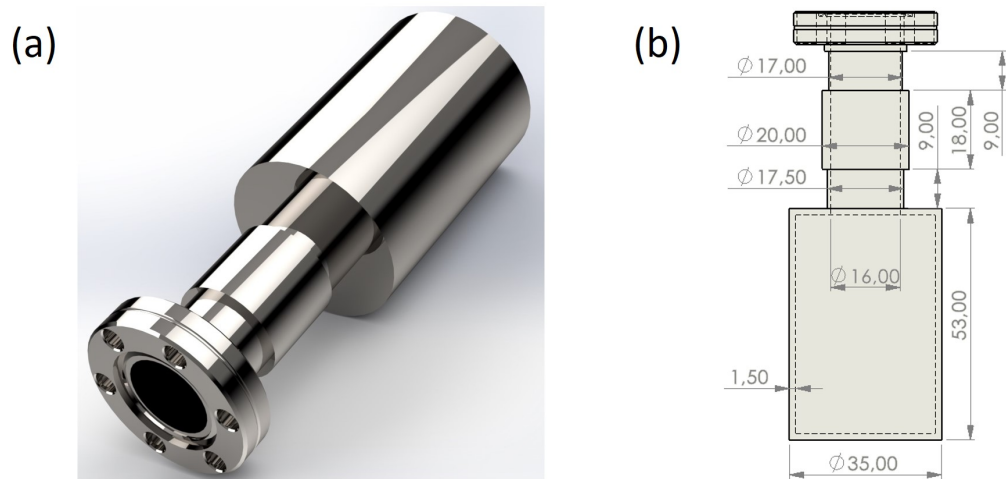


Figure 2.5: a) The final design of the Lithium oven. b) The physical dimensions of the oven. Here, the three parts of the tube connecting the lithium reservoir to the CF16 flange can be seen. All lengths are given in mm.

and a proper insulation.

First, the flux and its distribution is investigated. One fact about lithium is essential to know for this consideration, namely its large sticking coefficient of  $\approx 1$ . A lithium atom touching a surface will therefore nearly certainly stick to it. Assuming that only in the bucket the temperature is high enough for a substantial amount of lithium to evaporate, the walls of the tube limit the divergence cone of the evaporated lithium to the solid angle in which there is no contact with a wall before entering the 2D-MOT chamber. This consideration is important because the 2D-MOT trapping beams have a certain size and the lithium entering the chamber has to see the trapping region. Hence, the extent of the divergence cone at the center of the chamber has to be smaller than the MOT beams. Additionally, the cone has to be small enough to make sure that there is no direct line of sight from the hot lithium in the bucket to the viewports as otherwise these would get coated with lithium, worsening the ability to bring lasers into the 2D-MOT chamber. To change the extent of the cone one can either vary the length of the tube or its inner diameter. However, to maximize the outgoing flux the inner diameter should be as big as possible. Therefore, the diameter of the tube is fixed to the largest size a CF16 flange supports ( $r \approx 8$  mm) and only the length is varied to fix the divergence angle. The final dimensions are shown in Fig. 2.5 b). The inner dimensions of the tube are therefore fixed and hence the spatial distribution of flux. With this knowledge the total flux leaving the oven can be calculated. To do so the oven opening connecting to the tube is approximated as an infinitely thin walled aperture with a large reservoir behind. Hence, the aperture can be described as a

cosine emitter and therefore the flux is given as:

$$dN = \frac{d\Omega}{4\pi} n \bar{v} \cos \Theta A \quad (1)$$

Here,  $dN$  is the number of atoms in the solid angle  $d\Omega = d\Theta d\phi$ ,  $n$  is the number density of lithium at the temperature of the oven  $T$ ,  $\bar{v} = \sqrt{\frac{8k_B T}{\pi m}}$  is the mean velocity of an atom at  $T$ , with  $m$  being the mass of the atom,  $\Theta$  is the polar angle and  $A$  is the area of the aperture. The number density is obtained by using experimental data [17] of the saturated vapour pressure of lithium. This can be summarized in the formula:

$$p_s = p_a \cdot \exp\left(\frac{L_0}{k_B T}\right) \quad (2)$$

Where  $p_s$  is the saturated vapour pressure,  $p_a = 1.15 \cdot 10^{10}$  Pa is a phenomenological constant,  $\frac{L_0}{k_B} = 18474$  K is the latent heat and  $T$  is again the temperature of the oven. Using eq. (2), the number density is calculated by approximating the lithium gas as an ideal gas and using the ideal gas law.

To obtain the flux entering the chamber one needs to put in the geometric dimensions of the oven tube and calculate the solid angle. Here, the solid angles of hitting the tube wall  $\Omega_t$ , hitting the wall of the chamber  $\Omega_c$  and entering the chamber  $\Omega_{2D}$  are given,  $\Omega_t \approx 97.8\%$ ,  $\Omega_c \approx 1.6\%$  and  $\Omega_{2D} \approx 0.55\%$ . The distribution where the atoms end up after being evaporated from the oven is calculated using Eq. 1. The total flux leaving the oven amounts to  $\dot{N} = 1.32 \cdot 10^{16} \text{ s}^{-1}$  at  $T = 623$  K (350 °C) and to  $\dot{N} = 1.2 \cdot 10^{17} \text{ s}^{-1}$  at  $T = 673$  K (400 °C).

The next step is to calculate how much lithium has to be put in the oven to work for many years without refilling it, i.e. having to break the vacuum. For the dimensions of the oven shown in Fig. 2.5 b) and the resulting outgoing fluxes it was calculated that 10 g of lithium ensure a life time of about 20000 hours (2.3 years) at 623 K. This is approximately five to ten times more than what has been put into the existing experiments [16] which had an effective life time of a few years. Therefore, the oven reservoir is designed to contain up to 10 g of lithium to ensure a working experiment for the next decade. This is critical because there are no valves connecting oven, HV and UHV section. Thus, breaking the vacuum at any position results in the need to clean, bake and pump the full vacuum system again.

The last thing that has to be fixed is the thermal insulation of the oven. As was described earlier this is important because a heat source of up to 400 °C near the optics can worsen the experimental performance significantly. To prevent this, the two ways of heat influencing the system, namely radiation and heat flux along the tube, are addressed.

Heat flowing along the tube onto the chamber is in this design prevented by varying the heat resistance of the tube. The heat resistance is increased significantly when decreasing the wall thickness of the tube. Hence, by making the walls thinner in some sections the heat flux and the steady state temperature along the tube can be engineered. All heat resistances have been calculated using:

$$R = \frac{d}{A \cdot \lambda} \quad (3)$$

Where  $R \left[ \frac{\text{K}}{\text{W}} \right]$  is the heat resistance,  $d$  the length of the section,  $A$  the cross-section and  $\lambda = 15 \frac{\text{W}}{\text{K}\cdot\text{m}}$  the heat conductivity of VA 4571 stainless steel. The approach to engineer the temperature gradient along the tube can be explained in the same way as for electrical resistances connected in a row. The difference in temperature corresponds to the voltage and the heat flux to the electrical current. By changing the total resistance the total current flow is varied, whereas changing the relative size of the resistors fixes the voltage drops over each tube section. This presents a tool to also tackle another potential problem, namely the clogging of the tube with lithium and a consequently reduced flux. The underlying idea is to build the tube out of three sections with different length and thickness, acting as heat barriers of different strength (see Fig. 2.5 b)). As a result, the temperature of the tube even close to the chamber is above the melting temperature of Lithium ( $180^\circ\text{C}$ ), while the heat flow onto the chamber is still small. Also, the tube is designed in a way that directly after the oven bucket there is a step temperature drop thus only very little lithium evaporates to ensure the divergence cone to be defined by the tube dimensions and therefore preventing the windows from getting coated. The temperature along the tube is engineered as follows. First, a drop of about 100 K ensures low evaporation, then a slow drop of 70 K keeps the temperature above the melting point and lithium sticking to the walls can flow back into the oven, by this preventing clogging and recycling a lot of otherwise unused lithium. The last section fixes a drop of 160 K to decouple chamber and oven to let only very little heat through.

The heat loss due to radiation is minimized by isolating the oven with insulating material and aluminium foil. Additionally, in this experiment a normal thermocup with double walled vacuum insulation is put around the already insulated oven, minimizing the influence of radiation. To ensure best quality different thermo cups have been tested and the best performing one is used in the experiment.

In summary, the improved oven design offers a larger life time while supporting a larger flux at the same temperature compared to previous designs and being well insulated.

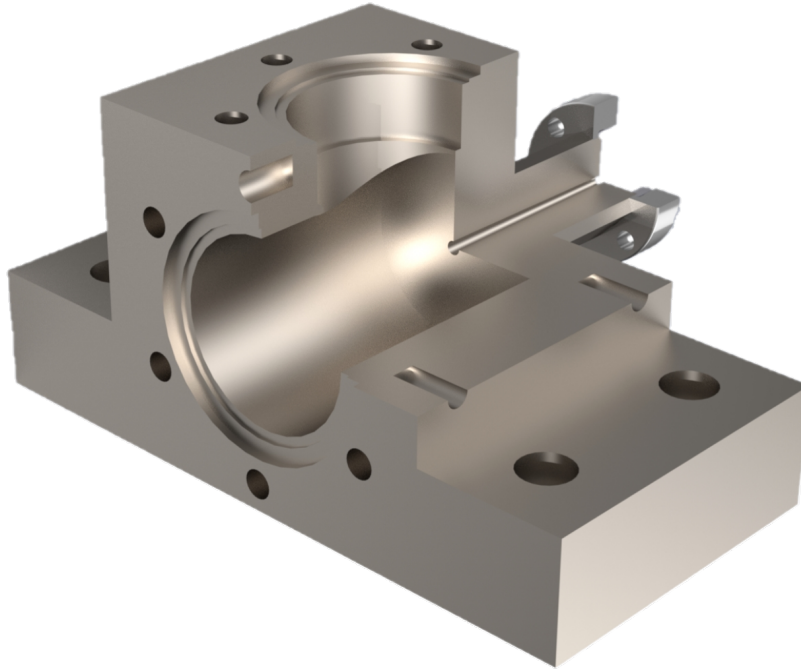


Figure 2.6: A cut out of the connector between 2D-MOT chamber and glass cell. The DPS is located in the CF16 tube.

**HV-UHV connector and differential pumping stage** The HV-UHV connector is a custom designed part machined from VA4571 stainless steel by the institute’s workshop. The part is an adapter from the CF16 flange of the 2D-MOT chamber to the CF40 flange of the glass cell that allows to install a second CF40 cross on top to attach gauge, pump and all-metal valve. Inside the CF16 tube the differential pumping stage is located. The DPS is a conical tube with small diameter (2 mm on the HV side, 2.89 mm on the UHV side) and a length of 44.5 mm used to decouple high vacuum and ultra high vacuum. The part is shown in Fig. 2.6. The decoupling of HV and UHV section is necessary because there will be a high load of non-lithium atoms coming from the oven as the lithium is only 95% enriched which limits the vacuum in the HV regime. However, in the UHV regime typically a pressure two to three orders of magnitude smaller than such a load allows is desirable. Decoupling using a thin tube is possible because the conductance of the DPS is very small and in the low pressure regime, where the mean free path between two particles is larger than the dimensions of the vacuum system, the low conductance can effectively keep up a pressure ratio of, for this case, above 1000. A pressure in the HV of  $10^{-(8\cdots9)}$  mbar therefore corresponds to a pressure of  $10^{-(11\cdots12)}$  mbar on the UHV side. The parameters of the tube have also been chosen to not clip the divergent atom beam coming from the 2D-MOT. For a discussion how to fix the tube dimensions see [18].

**2D-MOT chamber** The 2D-MOT chamber and the surrounding optics are shown in Section 4.3.1, Fig. 4.11. The design is taken from [12][13]. The chamber is made from titanium to ensure minimal magnetic permeability and was manufactured by SAES [19].

This part consists of four CF40 flanges for the four MOT beams, two CF16 flanges, one for the oven and one for a viewport as a possible pre-cooling stage. This can be done using the concept of a Zeeman slower for the atoms leaving the oven to pre-cool the atoms and hence increase the amount of capturable atoms. However, it is not implemented in the experiment as the Zeeman slower viewport would need constant heating due to its direct line of sight to the oven to prevent it from getting coated. In the final set-up this viewport is sealed using a blind flange.

Furthermore, the chamber has orthogonally to these ports a CF40 port to bring in a push beam and to have a large cross-section to pump and a CF16 flange to connect to the UHV section. Additionally, there are four places to put permanent magnets to provide the quadrupole field required for the 2D-MOT. The mounting of the chamber was originally intended to be done by putting rods under the wings on the sides of the chamber, but because there are no additional bellows in the design to absorb the tension which such a rod would bring into the system the mounting has been done differently (see Section 2.2.1).

For future consideration the area intended for mounting could be used to put CF16 viewports to have unoccupied axes to look at the 2D-MOT and probe it. Also, directly putting the differential pumping stage (DPS) inside the CF16 flange of the chamber might be an improvement to bring it closer to the MOT.

**Science chamber** The small 2" (50.8 mm) diameter glass cell acts as the heart of the experimental set-up. In the glass cell the atoms are captured, cooled to degeneracy, manipulated and detected. All the above operations require the use of laser light from various angles. Therefore, the glass cell has an octagonal shape with seven 0.5" (12.7 mm) viewports on the sides and two large 1.5" (38.1 mm) viewports from top and bottom to provide large optical access (see Fig. 2.7). The glass cell is manufactured by the company "Precision Glass Blowing" [20].

The optical access is further facilitated by the use of nano-coating structures on the in- and outside of all windows, which is done by the company TelAztec [21]. The coating allows for angles of incident of over  $50^\circ$  while still having reflectivities of below 1%. Also, it is very broadband and achieves these reflectivities for wavelengths ranging from UV light at below 200 nm up to long wavelength IR light at above



Figure 2.7: The octagonal glass cell with glass-to-metal transition to the CF40 flange.

1.5  $\mu\text{m}$ . The exact nano-structures used for the glass cell are called "RAR.L2". Hence, the use of a high numerical aperture (NA) objective of 0.7 or higher becomes possible as there is no decrease of collected photons comparing the middle and the edges of the window due to scattering at surfaces. The size of the top and bottom windows supports a NA of up to 0.9 while the side windows support a still large NA of 0.3. Therefore, the glass cell enables a variety of different tools and ideas to detect and manipulate atoms with highly increased fidelities.

The implementation of the glass cell has the further advantage to be made all from glass, with even the support structure of the windows being made exclusively from quartz glass. Hence, there are no Eddy currents induced when magnetic fields are switched rapidly nor is there a screening behaviour against RF or microwave pulses done with magnetic field antennas. This might support a substantial increase in preparation fidelities.

One drawback of this cell is the high sensibility of the nano-coating structures which makes handling the glass cell a very delicate task.

## 2.4 Construction

In this chapter the procedure to prepare and assemble the vacuum system as well as how to bake it is described. Furthermore, for every step of this procedure a work flow is established which can be used for future vacuum projects.

### 2.4.1 Vacuum Cleaning

To reach ultra high vacua of  $10^{-12}$  mbar every source of contamination can pose major problems. To get a feeling for this a small order of magnitude calculation is done. To estimate the amount of particles in the assembly before starting to pump, the molar volume of air ( $V_m = 29 \frac{\text{g}}{\text{mol}}$ ) and its density ( $\rho = 1200 \frac{\text{g}}{\text{m}^3}$ ) as well as the volume of the chamber and bellow ( $V \approx 41$ ) is needed. As a result there are an estimated  $10^{23}$  particles inside the chamber to start with. The goal for the bake out is to reach a vacuum 15 orders of magnitude lower, thus only a total of  $10^8$  residual gas atoms. To put this into perspective, the number of particles in one grain of dust ( $r = 0.01$  mm, consisting of silicon) is on the order of  $10^{14}$  particles. This shows the importance of a thorough cleaning of the parts to take any macroscopic contamination out of the assembly before starting to seal and pump.

For the cleaning a work flow has been established, based on [22] and expertise already existing in the group. Here, a differentiation between viewports, bellows and other components with large surface area and standard vacuum components is done as all need slightly distinct ways of cleaning to ensure as good of a vacuum as possible. In all cases contaminations from the people cleaning the parts have to be avoided. Therefore, the use of powder-free gloves, hairnets and masks, lint-free cloths as well as oil-free aluminium foil to cover all surfaces the parts touch, is inevitable.

**Standard vacuum components** The standard work flow to clean CF and KF components is as follow:

1. First, all obvious contaminations have to be removed using lint-free cloth or lens paper and solvent. As a solvent one can use isopropanol or, if the contamination is persistent, acetone. Note that after using acetone it is required to clean all surfaces exposed to the vacuum in the final assembly also with isopropanol afterwards to get rid off residues left by the acetone.
2. For very critical parts like those machined by the workshop or with direct line of sight to the glass cell, where the best vacuum is desirable, a first bake out is done at  $300^\circ\text{C}$  for at least several hours. In [23] and [24] it is shown that doing several bakeouts can significantly decrease the outgasing rate of the baked part which becomes relevant in Section 2.4.3.
3. After this, and as next step for all other components, the part is put in a ultrasonic bath of soapy water. Here, a mixture of Tickopur R36 (a tenside-free soap for ultrasonic baths) and VE water (de-ionized) is used. This step should be done at least two times for every part at  $\approx 70^\circ\text{C}$  for 15 minutes each time.

Between the runs the parts are rinsed with VE water and carefully dried with lens paper.

4. After the last run of soapy water the insides of the parts should not be touched anymore not even with gloves or lens paper. To erase leftover soap the parts are put in a ultrasonic bath of pure VE water (2 times at 70 °C for 15 minutes each).
5. As a last step, the parts are put on a new sheet of aluminium foil to dry, in a clean environment. If bottled air is blown onto the part to dry it off it has to be made sure that there are no solvents in the bottle which can come out and that the air used is clean.
6. The openings of all cleaned parts are covered with aluminium foil until the part is assembled in the system.

**Bellows and valves** For bellows and the inside of valves the cleaning procedure is different because of the large surface area of the ruffles of the bellow or the springs inside the valve. On these surfaces any residues of soap or acetone are very hard to get rid off and can consequently degrade the vacuum.

1. One residue-free solvent is isopropanol. This is used to clean all large surface area parts. The bellows are sealed on one side and then filled with isopropanol. At the top, several centimetres of space have to be left unfilled as the isopropanol will expand when heated.
2. Then the bellow is sealed also from the other side and put in a ultrasonic bath of VE water several times for 15 min each.
3. Afterwards, the bellow is unsealed and the isopropanol is put away. The bellow can either be rinsed in water or put down to dry immediately. Note that if the inside comes in contact with water the bellow has to be heated afterwards to evaporate the water fully. This can be done for example with a heat gun as the evaporated water is also immediately blown away.
4. Valves are cleaned only in closed position with the vacuum side filled with isopropanol and sealed like the bellow.

**Viewports** The manufacturer of the viewports (Kurt Lesker) does not recommend cleaning the windows in an ultrasonic bath [25]. Therefore, an alternative procedure is established.

1. First, all coarse contaminations have to be cleaned away which is done by using acetone as a solvent and lint-free cloth or lens paper. It is important to not apply a strong force while cleaning as large grains could scratch the viewport surface.
2. After using acetone the residues have to be washed away with isopropanol.
3. In a third step the viewport is cleaned with water and lens paper in small circles going outwards. One should use a lot of fresh lens paper and try not to wipe a cleaned part of the viewport with a cloth which was used for another part already.
4. Steps 1-3 are repeated many times until the viewports look clean. Particular attention has to be put on the glass-to-metal transition.
5. As a last step it has proven useful to clean the viewport a few times with VE water and to not do small circles, but wide ones to get rid off water stains.
6. The viewports are stored in lint-free cloth.

Note: Never blow the viewports dry with any gas, whatsoever! The sudden blow can cause the remaining liquid to rapidly evaporate, which actually is the intention, however this will also result in a rapid cooling of the viewport, posing a danger to the glass-to-metal transition and its sealing quality and hence can destroy the viewport. With this cleaning procedure a pressure of  $10^{-10}$  mbar was easily achieved without baking the vacuum, with the Ion-Getter pumps on. After baking a pressure of  $10^{-10}$  mbar in the HV and  $10^{-11}$  mbar in the UHV section is reported which is still falling at the time the thesis is written.

### 2.4.2 Mechanical set-up

Here, a brief summary of the assembly procedure is given. First, the mounting set-up was built up and put on the rails. Then, the middle three parts of the vacuum, i.e. the 5-way cross, 2D-MOT chamber and HV-UHV connector are put together with the connector attached last so as little torque as possible acts on the thin CF16 tube. Afterwards, the three pieces are put onto the mounts and fixed, like described in Section 2.2.1. Next, the Ion-Getter pumps are attached as well as the gauges, followed by the all-metal angle valves. These are connected with a T-piece and a bellow to a turbomolecular pump. The viewports and the oven are attached to the system last. This describes the compact high vacuum part of the system.

Behind the turbo pump a low vacuum gauge and a leak detector with scroller pump are implemented with KF components.

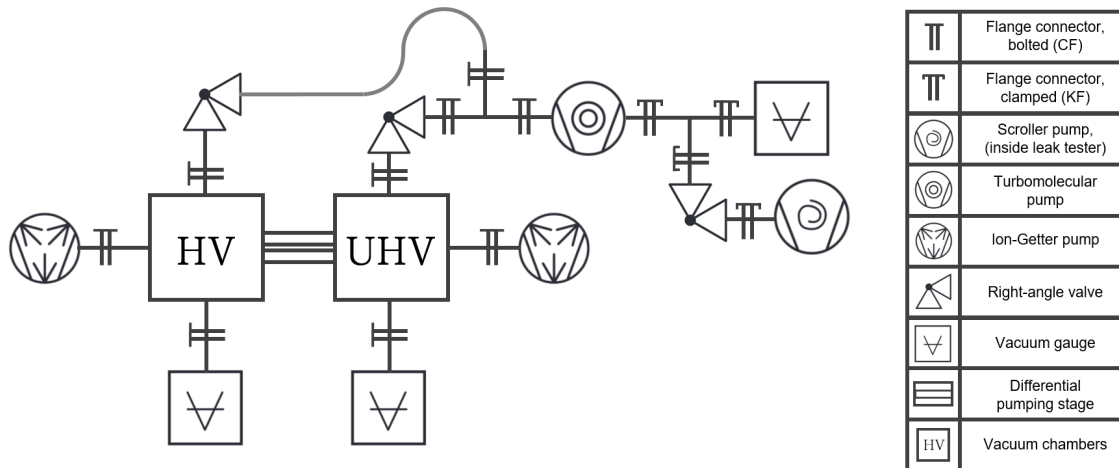


Figure 2.8: A schematic drawing of the final vacuum set-up.

### 2.4.3 Bake out

The term "Bake out", in the context of vacuum assemblies, describes the heating up of the full vacuum set-up that is supposed to have a very low final pressure (hence not the KF section). The temperatures range between 100 and 200 °C to stimulate the outgassing of contaminations and especially hydrogen from the walls. The increase in outgassing rate is due to the increase of saturated vapor pressure with rising temperature. Therefore, it is advisable to bake the vacuum set-up as long as possible for all the contaminations to evaporate from the walls and get taken out of the system by the turbomolecular pump. One week of pumping at 200 °C can therefore result in the same final pressure as pumping years at room temperature. With the same reasoning, it is sometimes advisable to "pre-bake" machined or other dirty parts in an oven at 300 - 400 °C before assembly. During the bake out process there are different critical steps which are briefly summarized:

- **Heating up:** During the initial heating it is important to not exceed a gradient of  $2-3 \frac{\text{K}}{\text{min}}$ . This can inflict tension on the glass-to-metal transition of the viewports possibly resulting in the windows getting leaky. The exact threshold has to be specified for every viewport individually, but in general a gradient of maximally  $1 \frac{\text{K}}{\text{min}}$  seems to be generally accepted to work well [22]. In the bake out of this apparatus a gradient higher than  $1 \frac{\text{K}}{\text{min}}$  was therefore avoided. To monitor the temperatures at different positions thermocouple sensors were implemented in the set-up and especially on all viewports.
- **Activation of the Ion-Getter pumps:** To avoid the getter elements to get coated by the contaminations coming from the walls while baking they

should only be activated during the cooldown process. They should also not be activated at room temperature because the dirt coming from the getters can stick better to the walls at lower temperatures. Also, the Ion pumps should be flashed a few times before activating the getters so the dirt evaporating from their surface does not coat the getter elements.

- **Cooldown:** Similar to the heating up a small temperature gradient has to be ensured at all times. At that time, the pressure should start falling as the load from the walls shrinks.

The exact pressure and temperature curves for the bake-out are not presented as the vacuum had to be broken several times for leak detection after the bake-out procedure. For the final bake out after the glass cell is attached to the system the pressure and temperature curves will be presented elsewhere. Given these points, the pressures of  $< 10^{-10}$  mbar in the UHV section and  $< 10^{-9}$  mbar in the HV section after less than 30 hours of pumping as well as the fact that pressures are continuously falling indicates that the CF section is leak free and ready for the glass cell to be attached to, as soon as it arrives from the manufacturer.

## 2.5 The experimental set-up

After discussing the individual parts as well as the set-up procedure, the final experimental set-up is presented. The experiment (08/2021) is shown in Fig. 2.9.

In summary, the compactness of the set-up with a total length of less than half a meter shall be emphasized. Additionally, other than the advantages mentioned above, the small size of the experiment also yields practical advantages like easy transportability of the complete vacuum set-up and a decrease in required laboratory space.

After discussing the design and assembly of the vacuum set-up in this section, in the next section one key component of the surroundings of the science chamber, namely the magnetic field coils are presented.

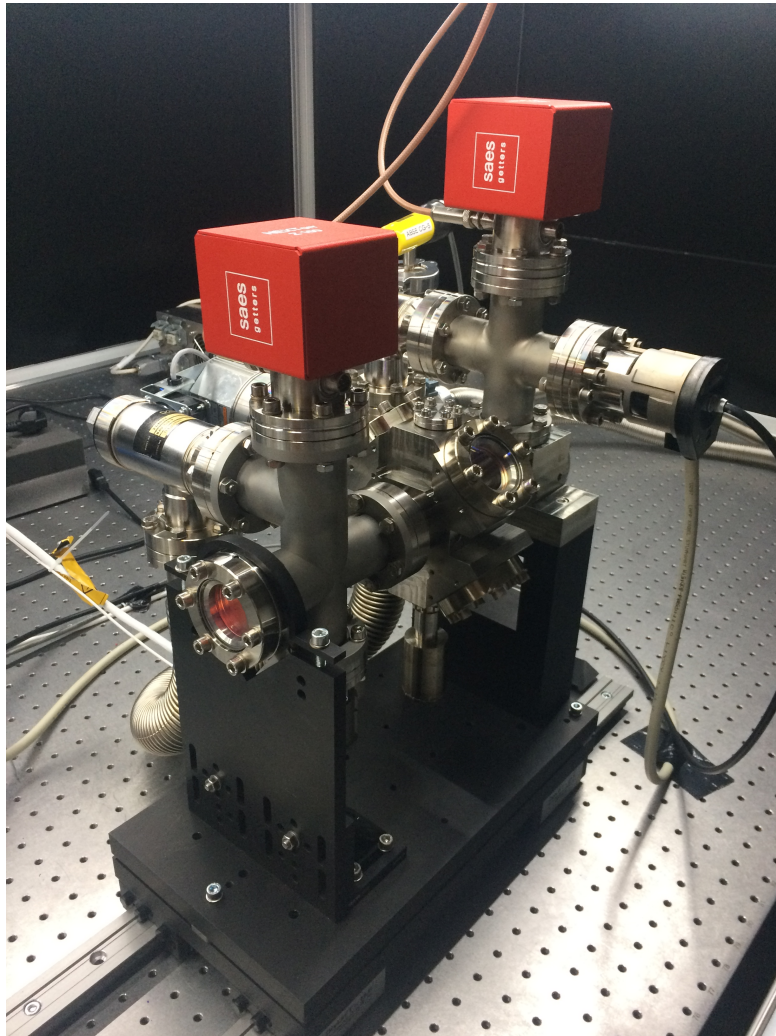


Figure 2.9: The vacuum assembly at the end of this thesis.



## 3 Magnetic field coils

Ultracold atom experiments offer a large toolbox for manipulating the quantum mechanical state of atoms. One of the most powerful tools in this process are magnetic fields. They are key in all parts of an experimental cycle, from initial loading of the 2D- and 3D-MOT where a quadrupole field configuration is required, to the last steps of the cycle, in which the interaction strength is tuned via offset fields, or for the precise manipulation of the hyperfine spin projection via radio-frequency and microwave fields. With the exception of the quadrupole fields in the 2D-MOT chamber which are produced by permanent magnets (see Section 4.3.5) all magnetic fields in this experiment are created using coils. These coils differ strongly in dimension, number of windings and geometry of the wires, depending on the task they need to fulfil.

In this chapter the main emphasis is put on the design of the coil arrangement around the science chamber i.e. the glass cell.

### 3.1 General principles of coils

Normally, magnetic fields are produced with current conducting wound coils. Following Maxwell's equations, a moving charge induces a magnetic field (B-field), encircling the charge. As a result, a charge moving along a circular path builds up a B-field which is oriented perpendicular to the plane of the circle at its origin and closes the field lines by going once around the wire. By putting a second coil parallel to the first one, some field lines do not directly close the loop, but go first through the second coil and just then close the loop. The magnetic field lines for two coils in this configuration is shown in Fig. 3.1. It is apparent that the field lines are oriented parallel to each other between the two coils. Therefore, one can produce very homogeneous fields.

By solving Biot-Savart's equation for the two coils one can show that for a current running in the same direction in both coils (clockwise or counter-clockwise) the field  $\vec{B}(r)$  in the center between the coils, denoted as the  $z = 0$  plane with  $z$  being the coordinate in the axial direction, is given by a sum of even powers in the radius and

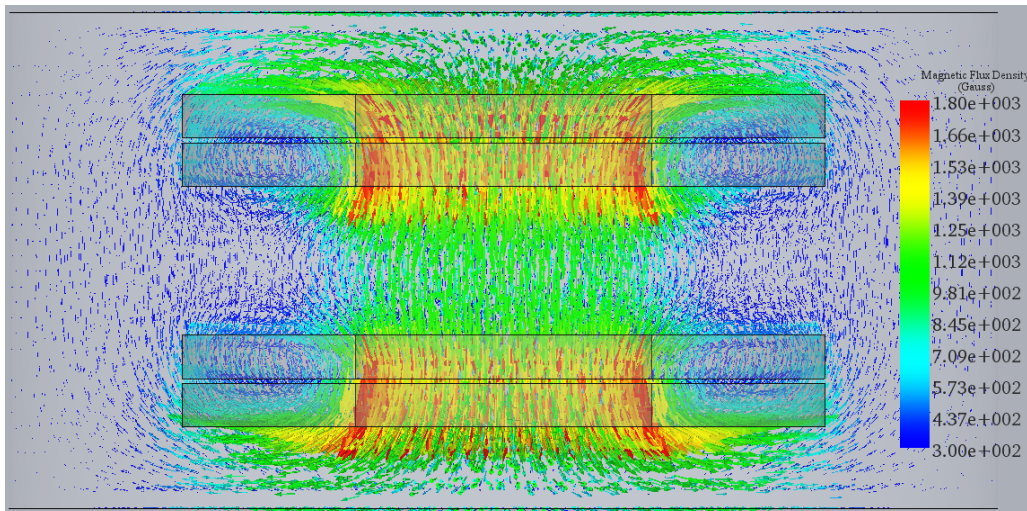


Figure 3.1: Streamline plot for a coil assembly in Helmholtz configuration. The simulation is done in a finite element analysis. Resulting from this, there are large magnetic fields at all edges as the boundary conditions are not well-defined there. The path of the magnetic field lines is vertical between the coils, leaves the lower coil in radial direction and re-enters the assembly through the upper coil, closing the field lines. Colour and length of the vectors denote the magnetic field strength. The simulation was done using software provided by EMWorks [30].

an offset term:

$$\vec{B}(r) = (B_0 + B'r^2 + B''r^4 + \dots) \vec{e}_z \quad (4)$$

Where  $B_0$  denotes the radius independent offset term,  $B'$  is the curvature of the field and  $B''$  describes the coefficient of the fourth order term. The fact that all uneven orders have to vanish can be explained by radial and mirror symmetry arguments. The offset term will later be used to set the interaction scale of the contact interaction of two atoms via the Feshbach resonance (see Fig. 3.3) while the second derivative or curvature is used for trapping.

It can further be shown that for a certain relationship of the distance  $d$  between the coils and their radius  $R$ , the second order term of the field strength vanishes and only the fourth order term persists. This condition is met when the radius of the coils equals their distance:

$$R = d. \quad (5)$$

This configuration is referred to as Helmholtz configuration. To make the field even more homogeneous a third coil in the  $z = 0$  plane could be added to make the fourth order contribution vanish as well. This is referred to as Maxwell configuration. For the newly designed experiment a pair of coils in Helmholtz configuration is used due

to the lack of space to put coils in the  $z = 0$  plane as all laser optic is located there. Differing from condition (5) solidifies in an emergence of a quadratic potential in the form of a magnetic field saddle. The potential is confining in the radial and anti-confining in the axial direction or vice versa depending on if  $R \lesseqgtr d$  and if the atoms are in high- or low-field seeking hyperfine states.

For two coils Biot-Savart's equation can be solved analytically on the  $z$ -axis, yielding:

$$\vec{B}(z) = \frac{\mu_0 N I}{2} \cdot \left( \frac{R^2}{(R^2 + (z - d/2)^2)^{3/2}} \pm \frac{R^2}{(R^2 + (z + d/2)^2)^{3/2}} \right) \vec{e}_z \quad (6)$$

$$\stackrel{z=0}{=} \left( \frac{4}{5} \right)^{3/2} \frac{\mu_0 N I}{R} \vec{e}_z \quad (7)$$

Where  $\mu_0$  denotes the vacuum permeability,  $N$  the number of windings,  $I$  the current,  $R$  the radius of the coils,  $d$  their distance from each other and  $z$  the coordinate in axial direction. It shall be noted that this formula is only valid on the  $z$ -axis and for coils placed at  $z = \pm d/2$ . The  $\pm$  in eq.(6) implies the current in both coils to flow either in the same (+) or opposite (-) direction. Also, the equation only holds true for thin coils with all windings located at the same position. For extended coils corrections have to be applied.

From eq.(6) and eq.(7) some general things for the design can be deduced. The most important of which is that bringing the coils closer to the atoms, in other words lowering  $d$  and hence  $R$ , to stay in Helmholtz configuration, will result in less current needed to achieve the same field strength and consequently in less produced heat.

$$P = R_{\text{Ohm}} \cdot I^2 \quad (8)$$

Here,  $P$  is the produced heat,  $R_{\text{Ohm}}$  the ohmic resistance of the wires and  $I$  the current required to produce a certain magnetic field. As  $R_{\text{Ohm}}$  depends linearly on the radius, the produced heat has a cubic dependence on the radius. Therefore, the first take away is that the coils should be designed such to be as near to the atoms as possible. Because Helmholtz relation  $d = R$  should be obeyed, this will be limited by the radius of the objective at about 3 cm and the height of the glass cell at 2.54 cm. Additionally, there is the further constrain that the coils also have to be properly mounted.

Furthermore, one finds that the current goes anti-proportional with the number of windings as there is no difference between a current flowing twice around the coil or double the current flowing around only once. This relation is vital for reaching a current range in which power supplies are available. Also, a lot of windings are desirable as it reduces the influence of non-perfect winding as well as the influence of

the supply lines which break circular symmetry. However, the fact that hollow core wires will be used to cool the coils sets a lower limit on how small the wires can be and therefore on the number of windings (see Section 3.3.1).

The geometry how to wind the coils, in other words the cross-section, is also dictated by Helmholtz's relation. In order to stay as close to the configuration as possible for an extended coil, the diagonal of the coil and the diagonal marking the positions where Helmholtz configuration is fulfilled should lie on top of each other. This is indicated by the grey dashed lines in Fig. 3.5. Therefore, the cross section dimensions of the coils should have a ratio of 2:1 of length in radial and height in axial direction. The area itself is not much limited by the surroundings of the glass cell and it also does not scale critically with produced heat, pressure drop of the cooling water (see Section 3.4.1) or current, making the size of the coils a prime candidate for coarse tuning while designing. Reason for this is that although many parameters do not scale critically with the size of the coils, a larger area can give other design parameters like wire cross-section or winding number a larger range to be optimized which may scale critical with above mentioned parameters. For example, larger coils enable the use of larger wires enabling the wires to have larger hollow cores and hence critically influencing the water flow.

With these considerations and the requirements on the coils discussed in the next section an optimized design is developed.

## 3.2 Requirements on the coil design

First, the requirements on the coil design are formulated. These are on the one hand given by the experimental realizability like the necessary power supplies and cooling circuits and on the other hand by the physical requirements the magnetic fields need to meet to realize certain quantum mechanical systems. Here, the basic idea of the design is to realize the quadrupole fields necessary for the 3D-MOT and the offset fields required for the tuning of interaction strength via Feshbach resonances using the same coils. This is possible because in the MOT loading phase the interaction of the particles does not have to be controlled and later when control is required the atoms have already been transferred into an optical dipole trap. Therefore, all different requirements on magnetic field gradient, offset field and curvature, required for different tasks in the experimental cycle, the final coil design has to combine.

### 3.2.1 Magnetic field range

The magnetic field range is given by two factors. First, the coils need to provide a magnetic field gradient of up to 70 G/cm. This range lets one freely optimize the 3D-MOT with respect to the size of the MOT beams, in particular the vertical beam which passes through the objective. The largest size achievable for the vertical beam will fix the maximal gradient. This is explained by taking into account the energy shift of the  $2^2S_{1/2}$  ground state of Lithium and especially the transition of the  $F=1/2$  manifold into the Paschen-Back regime at high fields (see Fig. 3.2).

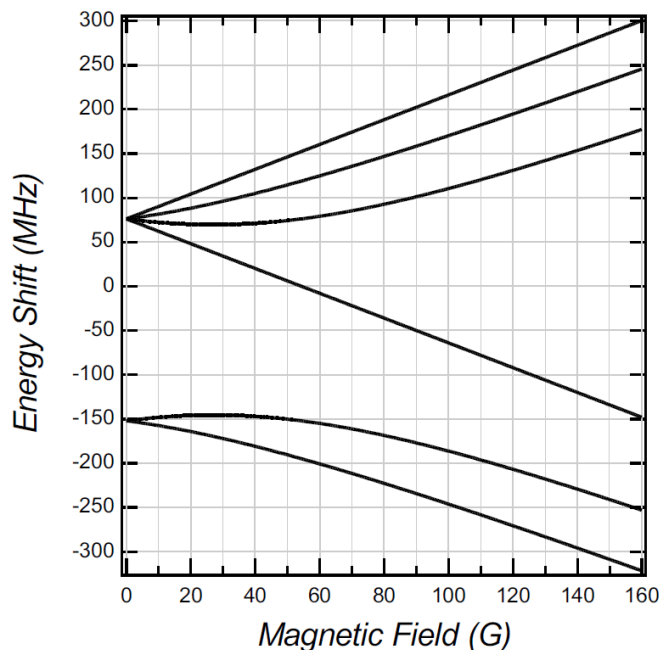


Figure 3.2: Energy shift of the  $2^2S_{1/2}$  ground state of  ${}^6\text{Li}$ . A special focus should be put on the lower doublet, i.e. the  $F = 1/2$  manifold. There, the  $m_F = -1/2$  state goes down, while the  $m_F = +1/2$  state goes up at low magnetic fields. The difference is used for the realization of the MOT (see chapter 4.1.2). At about 26 G however, the  $m_F = +1/2$  manifold exhibits a maximum and at the zero crossing of this state the effectiveness of the MOT is strongly degraded. Taken from [26].

As the  $m_F = +1/2$  state exhibits a maximum at 26 G and a zero crossing at slightly larger fields of around 50 G the magnetic field at the edges of the MOT has to be lower than 50 G for the MOT to function properly. Thus, the maximal magnetic field at the edges of the MOT beams limits the gradient.

Secondly, the coils have to be able to produce offset fields of up to 1500 G because the broad Feshbach resonance for Lithium 6, depicted in Fig. 3.3, is located between 689 - 832 G, depending on spin states. To explore physics deep in the BEC or BCS

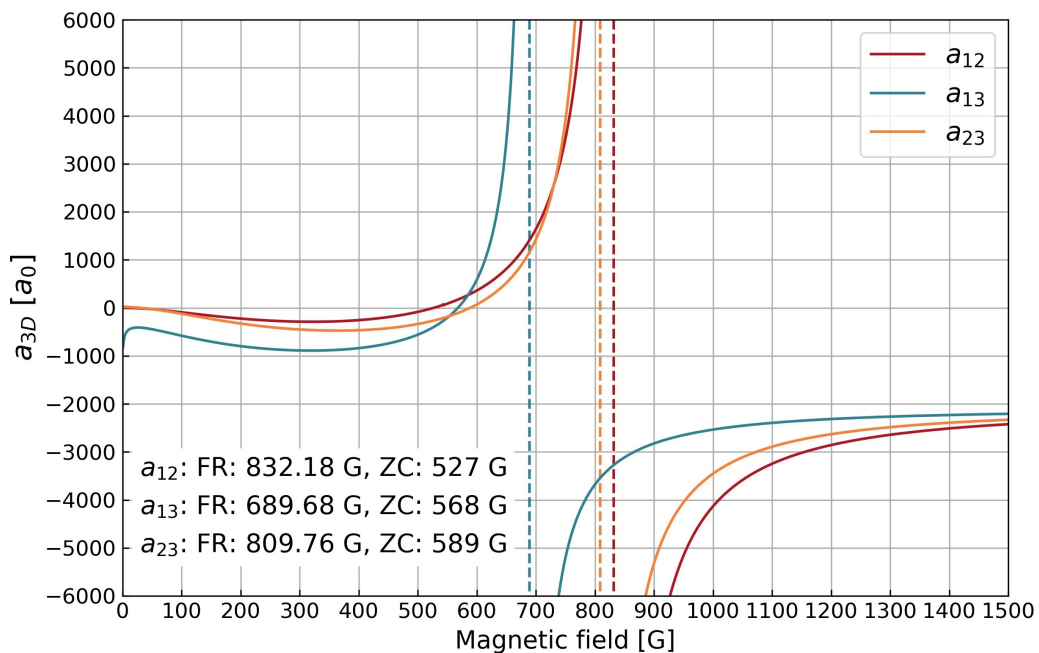


Figure 3.3: The Feshbach resonance in  ${}^6\text{Li}$ . On the y-axis the 3D scattering length  $a_{3D}$  is plotted in terms of the Bohr radius  $a_0$ . FR: Feshbach Resonance, ZC: Zero crossing (non-interacting particles). Data taken from [27].

regime it is necessary to apply magnetic fields some hundreds of Gauss above and below the resonance.

As all real coils are weaker than the ideal design due to for example non-perfect winding, the simulations have been done in a way that the coils are able to theoretically produce a field of 2000 G at the maximum current flow of the power supply which will be 400 A.

### 3.2.2 Temperature stability

To produce fields in the range described above, a lot of power is necessary which is dumped as heat in the coils (see eq. (8)). Reason for that are the high currents of up to 400 A and the ohmic resistance of the wire which is on the order of some tens of  $\text{m}\Omega$ . The heat load on the coils is on the order of a few kW. Hence, if the heat is not actively taken out off the system by active cooling, this would result in a rise of the coil temperature of some tens of Kelvin every second, making continuous operation impossible.

The temperature fluctuations shall be low because on the one hand they can inflict stress on the coils due to mechanical expansion which can lead to long term drifts of the magnetic field saddle and a deviation from optimal performance in general.

On the other hand high operation temperature limits the life time of the coils due to stress at soldering points and a degradation of the used epoxy. Having a large heat source directly next to the high NA objective, the glass cell and the surrounding "normal" optical components can additionally ensue thermal lensing effects limiting the performance of the optical set-up.

Therefore, an efficient cooling mechanism is needed to reliably take out 3-4 kW. In the designs used in the group up to now this has been done by an external water cooled heat sink [28]. In that case the outgoing heat flux is limited by the interface between coil and heat sink which was done using diamond filled epoxy. The limitation imposed on the cooling capability leads to a steady state temperature at continuous operation of about 60 °C. Therefore, there is much room for improvements and a reliable and powerful cooling technique will be a central part of the coil design.

### 3.2.3 Switching times

After this very technical requirement on the coil design there are two more aspects given by the physics of interest that have to be taken into account. The first one is the switching time of the coils, i.e. the timescale with which the coil can switch its magnetic field from one value to another. The timescale is fundamentally limited by Lenz's rule, which states that a changing magnetic field always induces a voltage in order to to slow down the change. Hence, if the current in the coils is quenched to zero there is a characteristic timescale given by the inductance of the coils in which the B-field and the current actually fall to zero. The timescale can be shortened by snuffer circuits over which the induced voltage falls off (an overview is given e.g. in [29]). There, the timescale is given by the electrical parts used and the power it can dissipate at a certain voltage. Usual examples are MOSFETs or IGBTs, which typically take voltages up to 80 V or 1000 V respectively before becoming conducting. The physical requirement for such rapidly changing fields is the idea to jump the magnetic field fast enough for the atoms to not being able to adiabatically follow and hence quenching the system into a different state. Advantages might be increased fidelities or having the possibility to project the wavefunction of the system onto some new basis more cleanly.

This may offer the possibility to prepare atoms on the attractive side of the Feshbach resonance and by quenching to the weakly repulsive side possibly increasing preparation fidelities.

The goal for the design is to be able to jump some hundreds of Gauss in about 1  $\mu$ s.

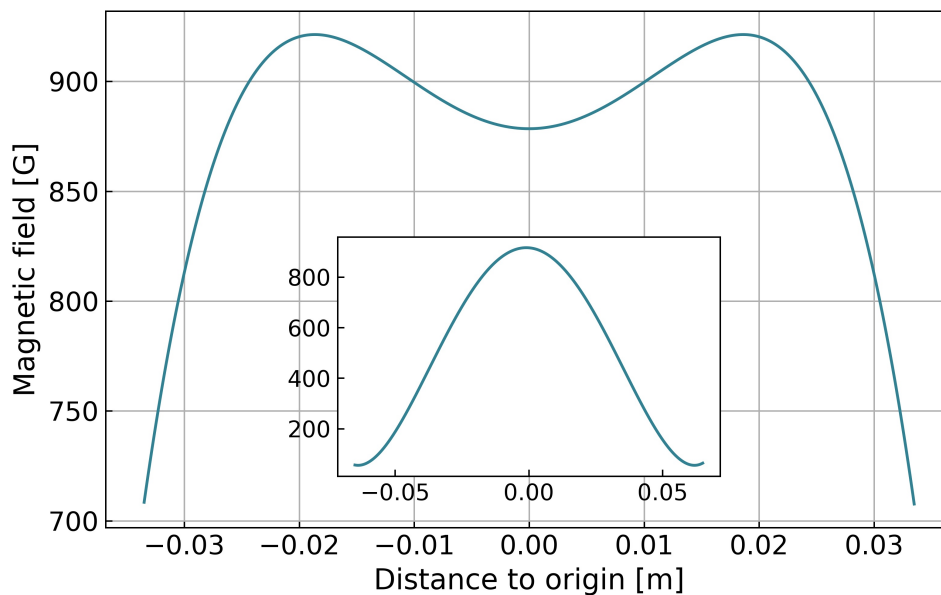


Figure 3.4: The magnitude of the axially pointing field on the symmetry axis (large plot) and in the  $z = 0$  plane (inlet) for a pair of coils with  $d > R$ . On the abscissa the distance to the center of the coil pair in axial and radial direction is shown, respectively.

### 3.2.4 Curvature control

The second aspect the coils shall be able to do is control the curvature of the magnetic field at the position of the atoms. In general, the second order derivative of the field is non vanishing if the coils are not placed in perfect Helmholtz configuration. The curvature can be used to trap the atoms in the radial direction in a very homogeneous, harmonic magnetic trap which can be used also for matter wave optics (see Section 5.2.1). To have an increased tuning range in this regard, the curvature of the field shall be tunable from zero up to  $\sim 30$ -40 Hz trap frequencies. In Fig. 3.4 the saddle potential for coils with a distance larger than their radius is shown, resulting in a local field minimum in the axial direction and a maximum in radial direction. As the three lowest lying hyperfine states of  ${}^6\text{Li}$  in the Paschen-Back regime are high-field seeking (see Fig. 3.2) hence move towards the point of largest field, this potential is confining in the radial and anti-confining in the axial direction. As both curvatures are linked, it has to be noted that increasing the curvatures in order to trap the atoms more tightly in radial direction, simultaneously leads to an increased anti-confining force in axial direction. Hence, an additional, typically optical confining potential with large trap frequency has to be introduced to capture the atoms in the axial direction.

### 3.3 Features of the design

Before describing the actual design of the magnetic field coils, the basic features are summarized. In Fig. 3.5 a possible design, incorporating all the features described below, is presented.

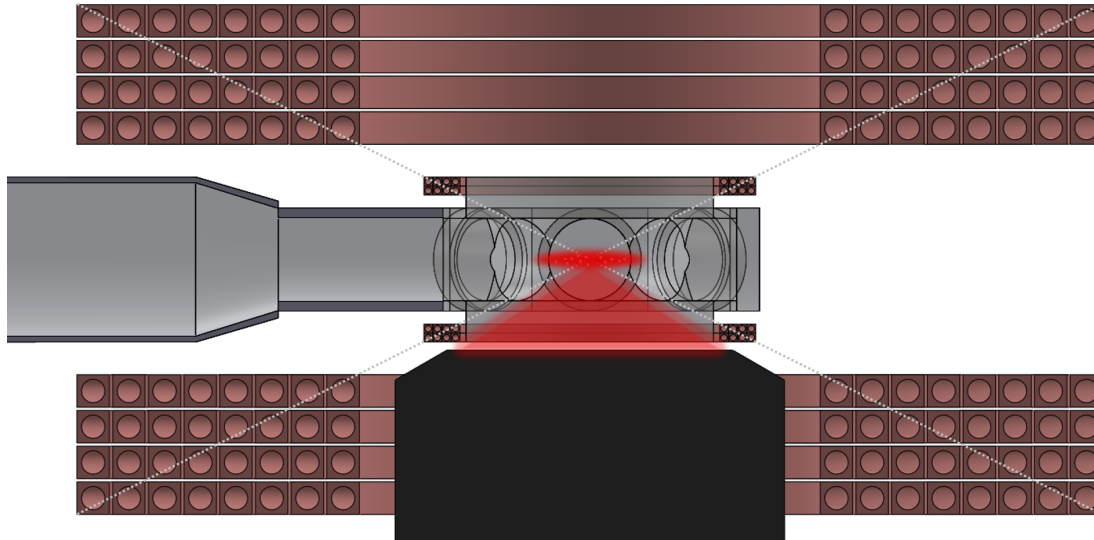


Figure 3.5: A vertical cut through one possible final design of the coil assembly surrounding the glass cell shown in the middle. Next to the upper and lower viewports the jumping coils are located and further out the Feshbach/MOT coils. The outer coils are split in the middle between the second and third row of windings and have individual current and water supply lines, which are not shown here. All coils are wound with hollow core copper wires. The thin grey dotted lines indicate the positions at which Helmholtz configuration is fulfilled. In black the size of a possible high NA objective design is indicated with the atom cloud position and the laser path shown in red.

#### 3.3.1 Hollow core wires

The main difference to the coils used in the standing experiments for which the designs are described in [28] is the different cooling interface. For the first generation of coils in this group the wire shape was 5 x 1 mm, hence the wires were flat bands and the cooling was done by water flooded copper heat sinks glued on top. In that design the total amount of heat that could be taken out of the system per second was severely limited by the interface between copper heat sink and coil and in particular by the epoxy used to connect both. A lot of effort was put into optimization of the interface by for example using diamond-filled epoxy with a large heat conductivity

or by engraving outlet slits on the top side of the coils to avoid the formation of air bubbles and give excess epoxy space to minimize the thickness. However, these optimized heat sinks still resulted in a temperature gradient along the vertical axis of the coils, as well as the need to control the duty cycle of the Feshbach coils to avoid overheating.

For that reason, a more efficient way of cooling is desirable. This is implemented by using hollow core copper wires which are nothing else than normal copper wires with a hole inside through which a coolant can flow. As a result the surface area of the copper-water interface is increased tremendously while also getting rid of the limiting epoxy-copper interface. Hollow core wires are typically used whenever a lot of heat has to continuously be taken out of a system, like for these coils. There is however a main disadvantage, namely the increased size of the wires. The increase in size is due to the limitation that the inside tubing cannot be arbitrarily small as this would result in a strong increase of the required pressure to enable a certain water flow. This is described by Hagen-Poiseuille's law (see eq. (11)), stating that the pressure scales inversely with the radius of the tube to the fourth order. Consequently, a wire with double the radius of tubing requires sixteen times less pressure to conduct the same amount of water and hence take away the same amount of heat from the the system. This prohibits the use of very small cables and therefore sets a limit on the amount of windings of the coils for a fixed total size. But, as shown in Section 3.4, there is a parameter regime of available wires satisfying both the need of efficient cooling as well as required current and winding number.

#### 3.3.2 Center tap

In Section 3.2.4 the idea to have complete control over the parameters of the field and especially its curvature was introduced. This is realized by splitting the Feshbach/MOT coils into two separate pairs of coils, one sitting slightly above and one slightly below Helmholtz configuration (see Fig. 3.5). In the following, the procedure to split the coils in the middle and providing them with individual water and power supply lines is called "Center tap". Therefore, each coil pair on its own will have a curvature as it is out of Helmholtz configuration and only when the current in each coil is tuned accordingly, there will be no curvature on the total magnetic field. Furthermore, the difference in current in the outer and inner coil pair acts as a tuning knob for the residual magnetic field curvature. The influence is simulated by solving Biot-Savart's law for all four coils and calculating the first and second derivatives at the position of the atoms.

The implementation of a center tap also has the advantage of shortening the coil wire

by a factor of two. This linearly propagates to reduce the required pump pressure for the cooling circuit by a factor of two as well.

One disadvantage is the increase in the number of currents that have to actively be stabilized from two to four, resulting in double the number of current transducers and read-out electronics necessary to realize this configuration of coils.

An important aspect to mention is the fact that, resulting from Earnshaw's theorem, there cannot be a maximum of a static magnetic field in all spatial directions. As the three energetically lowest spin states of the Lithium ground state are high field seeking in the Paschen-Back regime (see Fig. 3.2), there cannot be a completely confining purely magnetic field configuration for these states. In fact, the curvature produced by using a center tap manifests itself as a saddle potential, being a local maximum in the radial directions and a local minimum in the axial direction. Hence, while the atoms are magnetically trapped in a harmonic potential in the radial direction they are anti-trapped in the axial direction posing the need for some additional, non-magnetic confinement. This is usually done by an optical lattice in z-direction.

Remark: For atomic species which have low field seeking ground states the implementation of Ioffe-Prichard or Cloverleaf coil configurations might be a possibility, in order to produce magnetic field minima in all spatial directions, yielding a fully confining potential. For these configurations curvature control can also be achieved.

### 3.3.3 Jumping coils

The last new feature compared to the coils used in the older experiments of the group [28] is the implementation of an additional pair of coils. These will be mounted around the upper and lower viewport of the glass cell, having a radius of approximately 2 cm. Their purpose is to enable fast magnetic field jumps of about 300 G to, for example, quench interactions between the atoms. As the switching time of coils is limited by the total energy stored in the magnetic fields and the timescales on which this can be dissipated, the volume enclosed by the coils is minimized. Therefore, the radius of the jumping coils is decreased with the lower limit set by the diameter of the glass cell viewport. Additionally, the inductance  $L$  is minimized, therefore the number of windings  $n$  has to be rather small because  $L \propto n^2$ . This poses a challenge as the coils are supposed to produce fields of several hundred Gauss. Hence, a sweet spot needs to be found between switching time, availability of current sources and cooling power.

The coils are located near to the glass cell and the high NA objective, thus it is essential for them to be cooled efficiently because even a few Watts dumped continuously into the system can influence the whole set-up. Therefore, also for the small jumping

coils hollow core wires are used as there is no place to install some other kind of heat sink. Due to increased flow resistance for small tubes this is a challenging design task and a solution is proposed in Section 3.4.2.

## 3.4 Design of first generation magnetic field coils

### 3.4.1 Determination of mechanical parameters

In this section the process of how to arrive at the final design of the magnetic field coils is discussed. This is done with the requirements (see Section 3.2) and general design restrictions in mind. For the simulation the inside radius of the coils is fixed at 45 mm ( $> \varnothing_{\text{objective}}$ ) which enough space to comfortably mount the coils. If the high NA objective, currently limiting the radius, becomes smaller than expected at the time these simulations are done, the size can be slightly reduced, simplifying the design procedure.

First, it is summarized what was simulated. The simulation uses eq. (6) and its first and second derivatives to calculate magnitude, gradient and curvature of the field on the symmetry axis. This is done for all six individual coils (two fast coils and two Feshbach/MOT coils, which are split into two separate coils each) and the results are summed up. The input parameters of the simulation are the geometry of the wire cross-section, the size of the coils, their inner radius and the maximal field the coils are required to produce. The results are the maximally necessary current, the total water flow to cool the coils and the pressure required to achieve this flow. Hence, the simulation takes in a design choice and gives out the requirements this poses on the power and cooling supplies. In Fig. 3.6 **a**), the dependence of the current needed to produce a maximum field of 2000 G and the cable width is shown. The dependence of current  $I$  and cable width  $w_{\text{cable}}$  is given by:

$$I \propto w_{\text{cable}}^2 \propto n \quad (9)$$

Here,  $n$  denotes the number of windings. The relation of  $I$  and  $n$  is directly deduced from eq. (7). As magnetic field  $B$  and radius  $R$  are input parameters of the simulation, the required current can easily be calculated. In plot **b**) of Fig. 3.6 the relation of total water flow needed to cool the coils and the size of the hollow core tubes is depicted. On the x-axis the ratio of the current carrying ( $A_{\text{copper}}$ ) and the water carrying ( $A_{\text{water}}$ ) area is plotted.

$$\text{Ratio} = \frac{A_{\text{water}}}{A_{\text{water}} + A_{\text{copper}}} \quad (10)$$

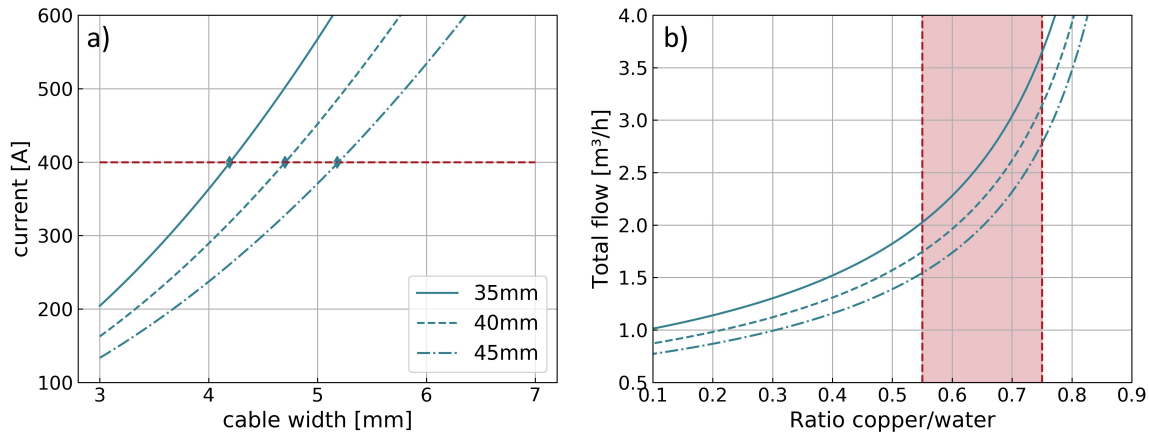


Figure 3.6: **a)** Dependence of the current needed to produce a field of 2000 G and the width of the hollow core wires. **b)** Total water flow needed to cool the coils in dependence of the size of the hollow core tubes. The red shaded area indicates the available range in the copper/water ratio. The different lines mark different overall sizes of the coils.

This is fully determined by the geometry of the wire cross-section chosen. The flow is calculated by the amount of heat the coolant can take out of the system if it is heated up by 1 K and the heat load on the system described by eq. 8.

In Fig. 3.7 the pressure required to achieve the water flow necessary for efficient cooling is depicted in false colors in dependence of the wire geometry described above. The red line marks the cable width determined as upper limit from Fig. 3.6 **a)**. In particular, it is plotted for three different sizes of the overall coil, more precisely a side length of 35 mm, 40 mm and 45 mm (left to right). This is calculated using Hagen-Poiseuille's law:

$$\Delta p = \frac{8\eta L Q}{\pi r^4} \quad (11)$$

Here,  $\Delta p$  denotes the pressure to drive a water flow  $Q$ ,  $L$  is the total length of the wire,  $\eta$  describes the dynamic viscosity of water and  $r$  is the radius of the hollow core. The x- and y-axis in Fig. 3.7 are identical to the x-axes of the plots in Fig. 3.6. Therefore, it is possible to interconnect between the plots to optimize the magnetic field coil design. The parameters which are varied for the optimization are the cable cross section, the hollow core diameter and the side length of the coils. To determine if a design is good, the three plots are used in the following way.

From Fig. 3.6 **a)**, the maximal cable width (assuming square cross-section cables) is determined as the width at which the current exceeds 400 A. The current has been chosen as up to that threshold there are custom available solutions that have already been tested and have proven to be feasible for this purpose.

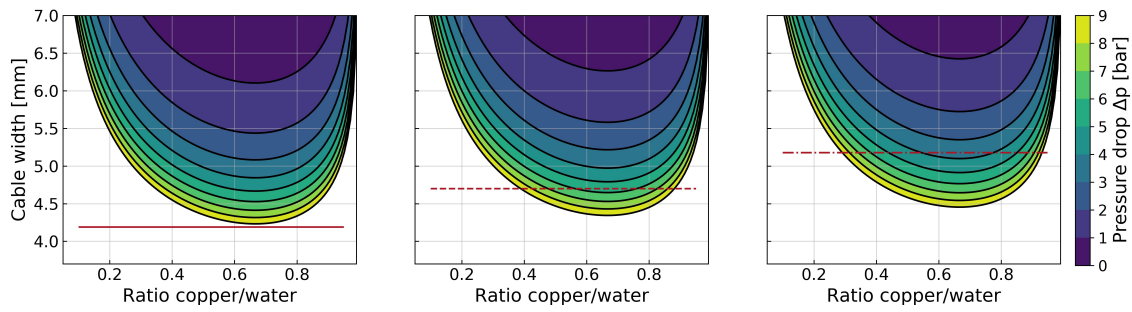


Figure 3.7: The pressure drop is shown in false colors for different ratios of hollow core size and cable width as well as for different absolute cable widths. This is plotted for three different side lengths of the coils 35mm, 40mm and 45mm (left to right).

Therefore, in Fig. 3.7 only the area below the red line is of interest for possible designs as the area above would exceed the maximal electrical current. Consequently, the minimal accessible pressure regime can be determined by finding the ratio at which, for the maximal cable width, the pressure is lowest. As this has been done for many different sizes of coils, as well as different geometries of the surroundings it has been shown that commonly the minimal pressure drop is realized at a ratio of about 0.65. Furthermore, typically the minimum is quite shallow, resulting in a tuning range of the ratio of about  $\pm 0.1$ , keeping the pressure drop nearly constant. With that range of possible ratios and therefore different cable cross-sections for overall size and core diameter one can determine the complete required water flow to cool the coils effectively from Fig. 3.6 b). The range of available ratios is marked in red. The term "effective cooling" however is very qualitative and has to be specified. In this simulation, the cooling was defined to be effective if the cooling water leaving the coils is less than  $\Delta T = 1$  K hotter than the ingoing coolant. This translates to a temperature gradient along the coils of less than 1 Kelvin which matches the desired temperature stability easily.

The information on pressure and total flow obtained in this way are then compared to the specifications of the pump, i.e. to the pump curves of the water pumps in the secondary cooling circuit. A summary of available pumps by the manufacturer "Van der Heyden" is shown in Fig. 3.8. As four individual, big coils as well as two small ones need to be cooled it is important to multiply the total water current by four and two, respectively. This flow, summed with the flow needed to typically cool cameras and lasers, has to be smaller than the capacity of the finally chosen pump at the calculated pressure.

However, one also has to account for the full cooling circuit, i.e. supply lines, valves,

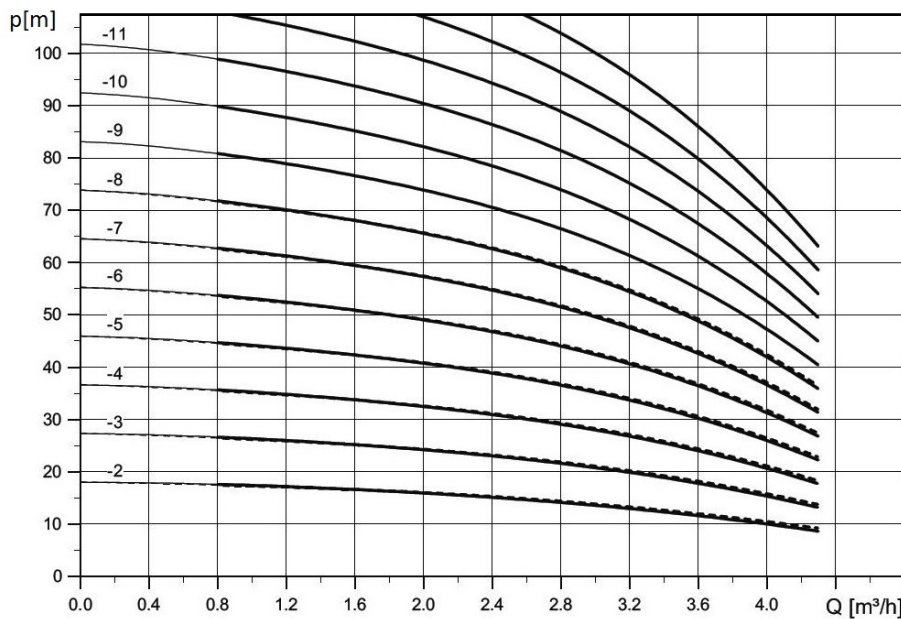


Figure 3.8: The available water flow in  $\text{m}^3/\text{h}$  at different pressures for pumps of variable strength (2 - 11) provided by the company "Van-der-Heijden". The y-axis shows the pressure in vertical meters. Data provided by [31].

connectors, and for the fact that the four large and the two small coils will be connected in parallel. As a result, the water current especially through the small coils can be reduced. To get a quantitative estimation, preliminary calculations were done which show that it is vital to always take into account the full cooling set-up and not only the parts with highest demand but also their relation to all other parts. Preliminary results show that either larger pressures are needed to cool the coils or the cross-section area of the coils has to be increased slightly compared to the calculations shown above by  $\sim 20\%$  to about  $\sim 5$  cm side length or the inner radius has to be reduced. Both are viable possibilities for the final design.

Following these steps, one can see if for a certain overall size of the coils there is a parameter regime in which there are current sources available and efficient cooling is possible. The goal is to minimize the size of the coils while still fulfilling the above described requirements and leaving headroom for deviations from the theoretically calculated values. As an example this is done for a side length of the coils of 45 mm. As a result, a maximal cable width of 5.2 mm is found. This corresponds to pressures between 4 and 5 bar at a width of 5 mm and ratios between 0.5 and 0.8. The total flow lies below  $2 \text{ m}^3/\text{h}$ . From Fig. 3.8 one can read off that to have some flow to spare at least pump 7 should be used as this can provide up to  $3 \text{ m}^3/\text{h}$  at 5 bar.

In this way the size of the coils is iteratively minimized. However, as the final di-

	Feshbach/Quadrupol coils	Jumping coils
Inner radius [mm]	40	20
Coil cross section <sup>(1)</sup> [mm <sup>2</sup> ]	40 x 10	5.4 x 2.7
Cable cross section [mm <sup>2</sup> ]	5 x 5	1.35 x 1.35
Hollow core diameter [mm]	2	0.5
Windings <sup>(1)</sup>	16	8
Cable length <sup>(1)</sup> [m]	5.53	1.14
Resistance <sup>(1)</sup> [m $\Omega$ ]	7.6	18.8
Inductance <sup>(1)</sup> [ $\mu$ H]	15	1.66

Table 3.1: The geometric parameters for the design of the magnetic field coils, in agreement with objective and glass cell dimensions and requirements on cooling and power supply. (1) Parameter for one single of the two coils disconnected via the center tap.

mensions of the high NA objective and therefore the inside radius of the coils is not known at the time this thesis is written only the work flow is established, but the final parameters of the coils still have to be determined for when the objective design is finalized.

### 3.4.2 Theoretical performance

In this section the expected performance of a coil assembly for a distinct choice of parameters which is compatible with the objective and the cooling circuit at the design stage at the time of this thesis is presented. In particular, the magnetic field curvature and its tunability are of interest. In Table 3.1 the geometric dimensions of the different coils and their electrical properties are summarized. In the middle column the large pair of coils with the center tap are listed. These are used to provide the magnetic field gradient during the MOT loading as well as the magnetic offset fields during the preparation of the system of interest. The parameters shown are the same which are used to depict the coil assembly in Fig. 3.5.

The inner radius is chosen in a way to leave enough space for the coils to be properly mounted next to the glass cell and the high NA objective. One aspect attention shall be drawn to is the small inductance of the jumping coils and the strong decrease in switching times.

In Table 3.2 the resulting magnetic field properties are summarized.

	Feshbach/Quadrupol coils	Jumping coils
$I_{\max}$ [A]	400	100
$\frac{B}{I}$ [ $\frac{\text{G}}{\text{A}}$ ]	4.8	3.16
$\frac{dB}{dz \cdot I}$ [ $\frac{\text{G}}{\text{cm} \cdot \text{A}}$ ]	0.94	1.68
$\frac{d^2B}{dz^2 \cdot I}$ [ $\frac{\text{G}}{\text{cm}^2 \cdot \text{A}}$ ]	0.013	0
Switching time $\tau$ [ $\mu\text{s}$ ]	26	153

Table 3.2: The simulated properties of the different magnetic field coils for the parameters presented in Table 3.1.

There, one sees that the Feshbach coils are designed to provide a magnetic field of up to 2000 G at the maximum current the power supply can provide while the jumping coils are designed to do jumps of up to 300 G. For the MOT, gradients of some tens of G/cm are required which is easily achievable with these pairs of coils. The curvature given here is due to the fact that the fields are calculated with the two coils disconnected by the center tap and located at slightly different positions. Hence, it represents the influence of the extent of the coils in comparison to the theoretical ideal case of a single conducting wire. As a feature of the center tap, this curvature can be set to zero by tuning the ratio of currents in both coils. Therefore, the curvature presented here is not the curvature one can actually produce with these coils by changing the ratio of currents but only the curvature acquired due to the extent of the coils and the resulting deviation from Helmholtz configuration.

In Fig. 3.9 the curvature control possible with one particular design choice is presented. On the x-axis of Fig. 3.9 the amount of current taken out of the outer coil and put into the inner one is shown, i.e. half the current difference between both coils at a constant total current. A negative  $\Delta I$  therefore describes a current taken out from the inner and put into the outer coil. On the y-axis on the left hand side the magnetic field curvature converted to the resulting trapping frequencies of the harmonic magnetic trap for  ${}^6\text{Li}$  atoms is shown. On the right hand side the offset fields at the different current configurations are shown.

The different line styles represent different current configurations: The solid lines show the configuration for a mean current  $I_{\text{mean}} = 100$  A and a  $\Delta I \in [-100, 100]$  A. For the dashed lines,  $I_{\text{mean}} = 200$  A and  $\Delta I \in [-200, 200]$  A. For the dotted line the mean currents in both coils differ with the inner coils current varying between -200 A and 200 A and the outer one varying between 400 A and 0 A.

From the plot one can deduce that at different magnetic offset fields, trap frequencies

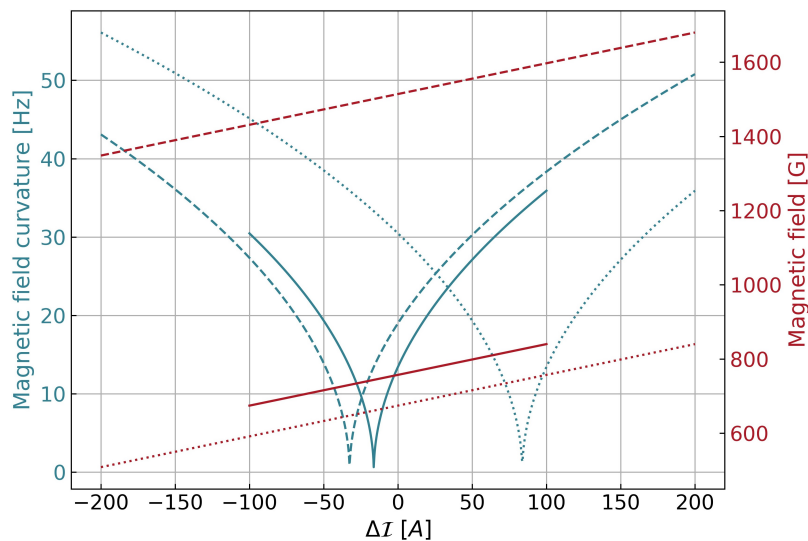


Figure 3.9: Magnetic field curvatures (blue) for different amount of current  $\Delta I$  taken out of the one coil and put into the other. The different line styles depict different current configurations explained in the text. In red the corresponding magnetic offset fields are presented. A negative  $\Delta I$  is equivalent with the current being taken out of the inner and put into the outer coil, hence forming a magnetic field saddle confining in the radial and anti-confining in the axial direction.

of tens of Hz are achievable using the implementation of a center tap. Also, it is shown that it is possible to set the curvature to zero by choosing the ratio of the currents appropriately. If the x-axis is rescaled to the mean current, thus showing the transferred current as a percentage of the mean one, the solid and dashed zero crossings fall on top of each other. Therefore, the same relative amount of current, for these coil parameters about 25%, has to be transferred to cancel out the magnetic field curvatures. This can be gauged in the experiment and function as a starting point for field characterizations in the future.

Lastly, from the dotted line it can be deduced that even larger trap frequencies of up to 60 Hz can be achieved by not only taking current out of one coil and putting it into the other, but by also changing the relation between inner and outer current in a more involved way.

Summarized, this particular choice of parameters enables the use of magnetic fields in all magnetic field regimes required for the experiment as well as enabling control of the magnetic field curvature to achieve a wide range of trap frequencies and also having the possibility to jump the magnetic offset field in a few  $\mu s$ .

## 4 The 2D-MOT - A compact cold atom source

First, a brief motivation on why to use a two-dimensional magneto-optical trap (2D-MOT) as a cold atom source shall be given. In the introduction to this thesis the evolution of one of the most advanced pieces of technology, the computer, is summarized. There, it is evident that improvement can manifest itself in two different ways. Either by a methodical improvement by refining the individual components of a system, but keeping the overall structure intact. Or secondly, improvement can be achieved by changing the underlying idea of operation of the system, but keeping the overall goal what to achieve untouched. The second approach is much more radical and uncertain in its results, as new expertise has to be collected, but also offers higher possibilities for large improvements. Therefore, it is usually wise to not change a set-up drastically at too many points at the same time as then the progress to get a machine running can be very difficult.

Consequently, in the case of the HQA experiment a trade-off is made at which points a fundamental change to the already existing experiments shall be done and at which points designs are adopted. These standing experiments [32][33] consist of a Zeeman slower, connecting the oven chamber to the scientific chamber which is made from stainless steel in an octagonal shape with re-entrant viewports from top and bottom. One strong limitation of such a system is the material the chamber is made of as steel is a conducting material. Hence, Eddy currents are induced by changing magnetic fields near by. Eddy currents limit the speed at which fields can be changed, due to Lenz's rule stating that the induced current always will induce a magnetic field in a way to slow down the initial change. Also, a chamber made from steel can act as a resonator for magnetic waves like radio-frequency (RF) or microwave pulses and in particular can screen all frequencies that are not in resonance. Thus, it can limit the use of microwaves to one frequency which is only resonant to the atomic transition at one magnetic field, making the experimental sequence more complicated.

Consequently, for a new experiment with the goal of increased cycle rates the use

of a steel chamber is not suitable anymore. The installation of a glass cell as the science chamber is one possibility to solve these issues. This replacement acts as one fundamental change in the set-up to achieve the goal of large cycle rates. Therefore, it requires adjustments of the surrounding systems, the biggest of which is the replacement of the Zeeman slower with a two-dimensional magneto-optical trap as the cold atom source.

This exchange is necessary because a Zeeman slower requires a direct line of sight of the hot lithium oven to the experimental chamber. If there is no way to get rid off the contaminations coming from the oven inside of the science chamber this will strongly degrade the vacuum pressure. Therefore, it drastically worsens all preparation fidelities of atomic samples in later stages of the experiment due to collisions with background atoms. Also, the lithium will coat the window opposite to the oven prohibiting the Zeeman slower laser beam to enter the chamber if no countermeasures are taken. Two possibilities to solve that issue are to either attach an exit to the glass cell so the contaminations and excess lithium will fly through and not stick to the glass, or to build a cold atom source without direct line of sight from oven to glass cell. However, a glass cell is a much more delicate piece to produce than a steel chamber, especially due to the glass-to-metal transitions involved which are necessary to match the thermal expansion coefficients of glass cell and steel flange. As a result, the first solution is not pursued for this experimental design. The second solution can be realized by the implementation of a 2D-MOT.

## 4.1 Theoretical background

Already in the early 1980's, first experiments have been realized in which atoms were decelerated with the use of lasers [34] and later also trapped with the additional implementation of magnetic fields [35]. This was done in a three-dimensional magneto-optical trap (3D-MOT). The theoretical explanation of the working principles of a MOT is the same for the case of trapping in all three spatial directions and only two with one axis being unconfined. Therefore, in this chapter the 3D-MOT will be used to describe the different processes leading to trapping and cooling of the atoms as it makes notation more easy because the spatial directions are indistinguishable. The basic derivations are based on [36].

### 4.1.1 Atom-Light interaction

The basics to understand the slow down process of atoms using lasers is the interaction of light and matter in general. For this, in Fig. 4.1 the atomic energy level scheme of

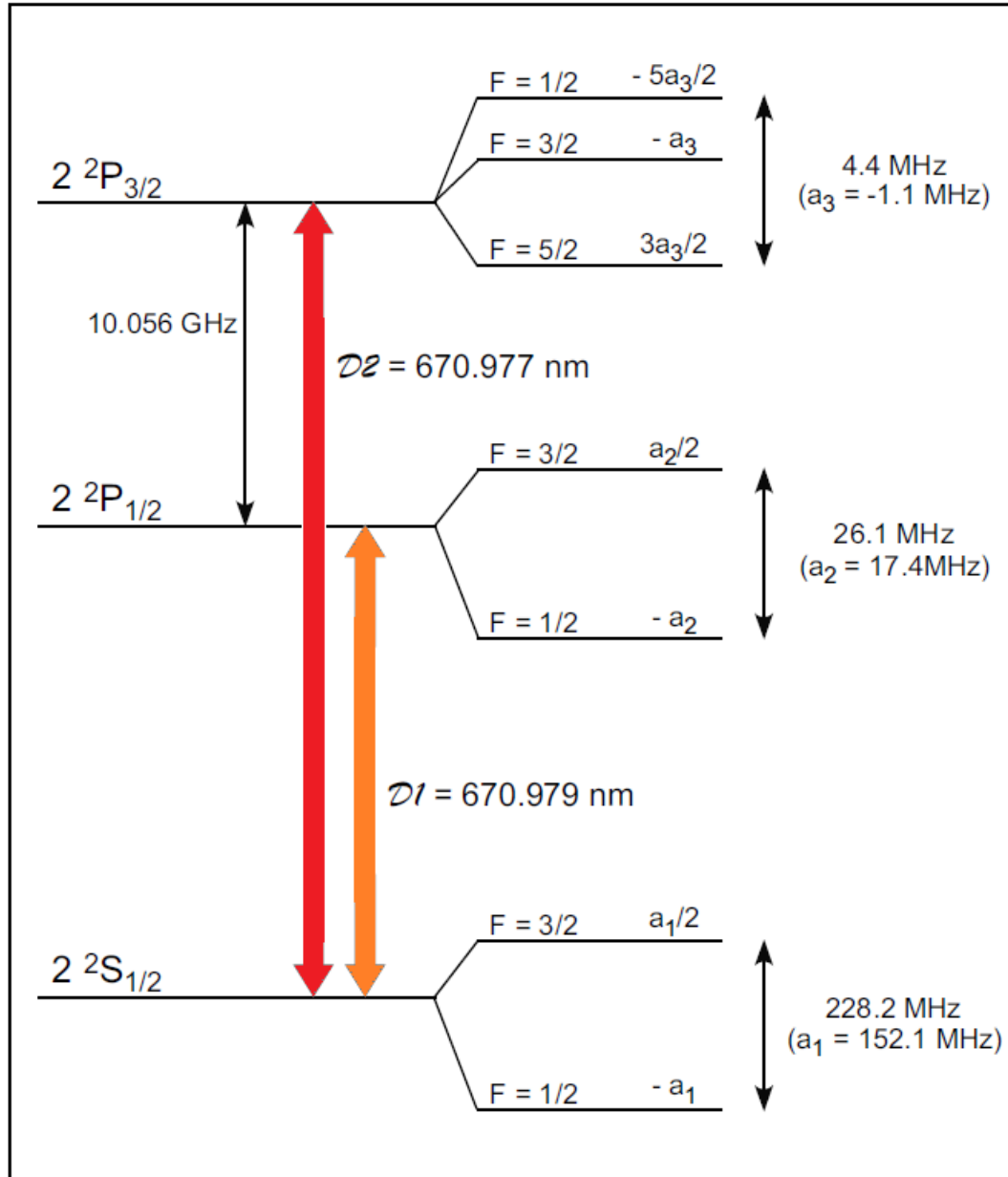


Figure 4.1: The energy level structure of the ground ( $2S$ ) and the first excited state ( $2P$ ) of  ${}^6\text{Li}$ . The  $D_1$  and  $D_2$  line are marked in orange and red, respectively. The ground state splitting is only about 228MHz much smaller than for different alkali elements [37]. Taken from [26].

${}^6\text{Li}$  is depicted. Here, the  $2^2S_{1/2}$  ground as well as the  $2^2P_{1/2}$  and  $2^2P_{3/2}$  excited states are shown. The coloured arrows mark transitions which are quantum-mechanically allowed and define the  $D_1$  and  $D_2$  line. Therefore, a photon incident on the atom with the wavelength of the transition can be absorbed and the atom will get excited into a higher internal energy state. Every excited state has only a finite lifetime as it is not the ground state of the system. The finite lifetime is directly connected to the natural linewidth of the transition. For the  $D_1$  and  $D_2$  line the lifetime is about 27 ns, corresponding to a linewidth of 5.872 MHz [26]. Therefore, the individual levels of the  $2^2P_{3/2}$  manifold cannot be resolved as the spacing is smaller than the linewidth of the transition. This fact will later be crucial as it is the reason why a repumper laser is required to achieve a closed cycle of excitation and deexcitation.

Additionally, it is essential that due to the finite linewidth of the transition, off-resonant excitations are possible. In other words, if the light incident on the atom is slightly detuned the excitation probability will be reduced, but will be  $\neq 0$ . The dependence of scattering probability and detuning can be seen in Fig. 4.2.

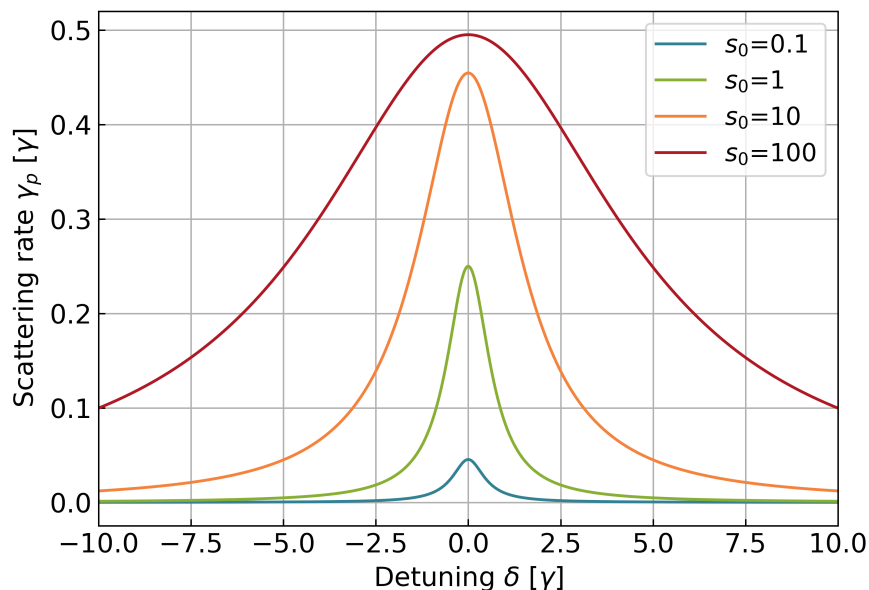


Figure 4.2: Scattering rate in dependence of the detuning of the incident light (both in units of the natural linewidth  $\gamma$ ) for different intensities of the light.  $s_0$  denotes the intensity in units of the saturation intensity  $I_{\text{sat}}$ .

The excitation rate can be calculated in dependence of the intensity of the light, the saturation intensity of the transition  $I_{\text{sat}} = \frac{\pi \hbar c}{3\lambda^3 \tau} = 2.54 \frac{\text{mW}}{\text{cm}^2}$ , the natural linewidth  $\gamma$  and the detuning  $\delta$ . This is given by:

$$\gamma_p = \frac{s_0 \gamma / 2}{1 + s_0 + (2\delta / \gamma)^2} \quad (12)$$

The parameter  $s_0$  denotes the intensity in units of the saturation intensity. In Fig. 4.2 it is apparent that for large intensities ( $s_0 = 100$ ) there is a substantial amount of scattering even many linewidths away from the resonance. Hence, in order to achieve strong interaction of the atom with far off-resonant light a large increase in intensity and therefore either in optical power of the laser or stronger focusing of the beam is necessary.

The reason why this is of interest becomes apparent when looking at the force acting on an atom when it is exposed to laser light. In each excitation process energy-momentum conservation has to be fulfilled, i.e. the energy of the photon is used to excite the atom to a higher internal energy state while the momentum of the photon is transferred to the atom as a kick in the direction of the photon.

$$\vec{F} = \frac{d\vec{p}}{dt} = \hbar\vec{k}\gamma_p \quad (13)$$

Where  $\vec{F}$  denotes the time averaged force over many excitation cycles acting on the atom,  $\vec{k}$  being the wavenumber of the photon and  $\gamma_p$  is calculated using eq. (12). As a result, everytime the atom is excited it gets a push in a well-defined direction. If the intensity is in a regime in which the main contribution of deexcitement processes is by spontaneous rather than by stimulated emission, the emitted photons are distributed homogeneously over the full solid angle. The force each of these emissions exerts on the atom therefore averages out and only the directed force due to the absorption processes remains. Hence, it is possible to apply a force to an atom by shining (near) resonant light on it.

From Fig. 4.2 one can also conclude that the rate of interaction is largest exactly on resonance. This presents the possibility to tune the interaction between atoms and light to different strengths at different points in space and even dependent on other parameters of the atom like on its velocity by manipulating the energy levels of the atom, and therefore the detuning, in a spatially and velocity dependent way. Consequently, fast atoms can be addressed more strongly, hence slowing them down and atoms far away from the center of the MOT can be accelerated in direction of the origin, effectively trapping them in position space. In the following, the two methods to control the detuning are summarized:

**Doppler effect** The Doppler effect describes the phenomenon of a velocity dependent frequency shift. More precisely, a moving spectator experiences the frequency of a wave differently, depending on their state of motion. In particular, a wave is blue-shifted (shifted to a higher frequency) when a spectator is moving towards and red-shifted (shifted to a lower frequency) when moving away from the source of the

wave. The amplitude of the shift is dependent on the absolute velocity of the spectator. For the atoms the laser can hence be on- or off-resonant depending on the velocity of the atom itself. The exact shift of the laser light the atom sees is given by:

$$\delta_{Doppler} = -\vec{k} \cdot \vec{v} \quad (14)$$

Here,  $\vec{k}$  is the wavevector of the laser and  $\vec{v}$  the velocity vector of the atom. A key point to notice is the direction dependence due to the scalar product. This offers a tool to address atoms depending on their velocity.

**Zeeman effect** The Zeeman effect describes the energy shift of atomic levels due to the influence of a static external magnetic field on the magnetic moment of an atom. The detuning resulting from this effect is given by the strength of the magnetic field and the magnitude of the magnetic moment:

$$\delta_{Zeeman} = \vec{\mu} \cdot \vec{B} = (g_{J1}m_{J1} - g_{J0}m_{J0})\mu_B B \quad (15)$$

With  $g_{Ji}$  the Landé factors in the "0" state (ground state) or "1" state (excited state),  $m_{Ji}$  the quantum number describing the orientation of the magnetic moment with respect to the magnetic field vector,  $\mu_B$  the Bohr magneton and  $B$  the magnetic field magnitude. By shaping the magnetic field, the detuning can be varied spatially. With these tools a detuning, and thus an excitation rate, depending on position and velocity of the atom can be engineered.

### 4.1.2 The Magneto-Optical Trap

First, the velocity dependent damping forces will be discussed. That dependence is the reason why it is called "viscous" damping. To closer examine this, the influence of two counter-propagating laser beams on an atom sitting at the origin is examined in 1D. Using eq. (13) the force of each of the two lasers with  $\vec{k}_+ = -\vec{k}_-$  can be calculated. Here, the detuning consists of two parts, one part that is modulated onto the laser beam artificially  $\delta_L$  using an Acousto-Optical-Modulator (AOM) and one given by the Doppler effect  $\delta_{Doppler}$ :

$$\delta_{\pm} = \delta_L + \delta_{Doppler} = \delta_L \mp \vec{k} \cdot \vec{v} \quad (16)$$

Plugging eq. (16) into eq. (13) for both lasers and calculating the total force as the sum of both, neglecting terms quartic or higher in  $\left(\frac{kv}{\gamma}\right)$  leads to:

$$\vec{F} = \frac{8\hbar k^2 \delta_L s_0}{\gamma(1 + s_0 + (2\delta_L/\gamma)^2)^2} \cdot \vec{v} \quad (17)$$

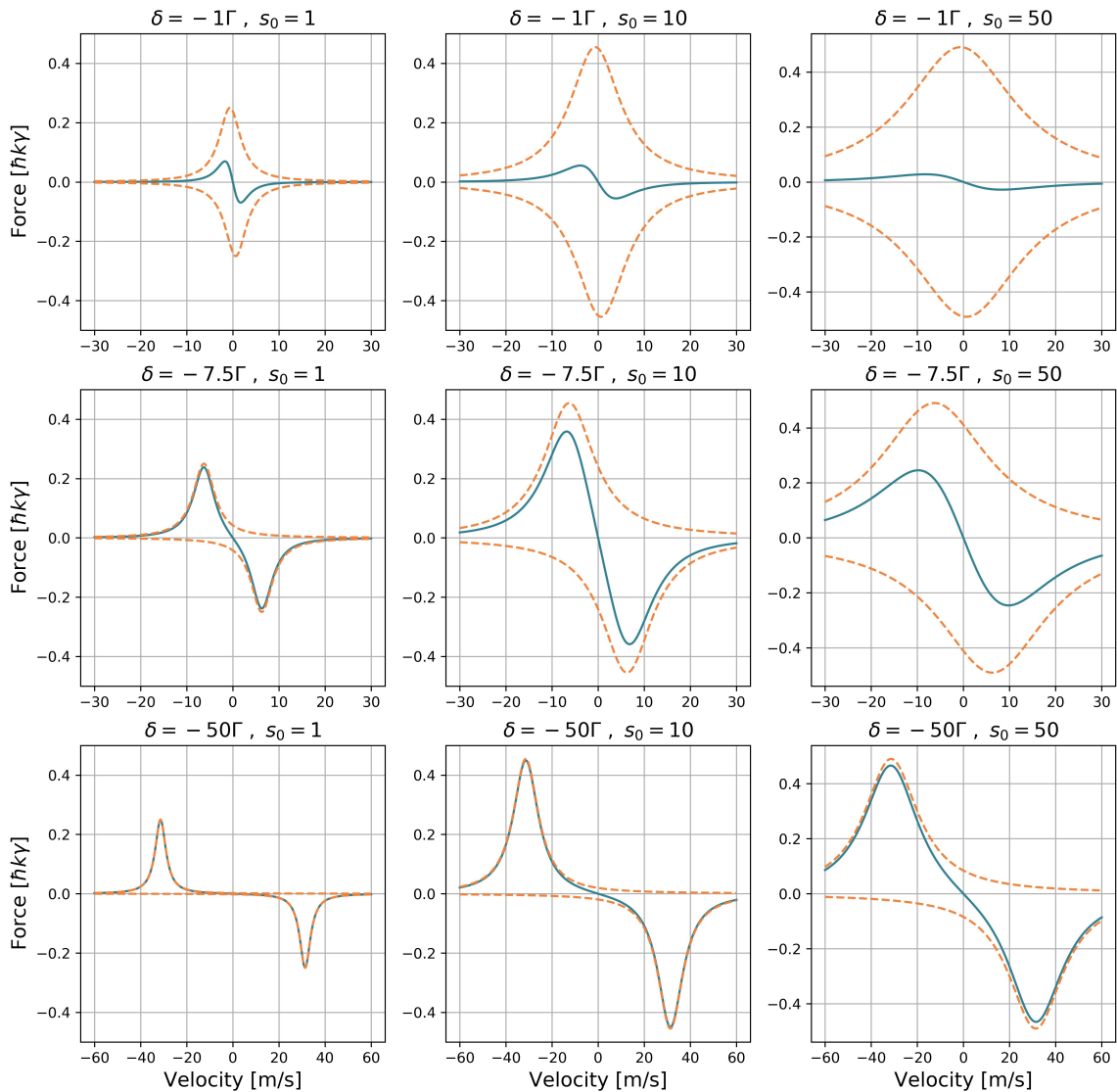


Figure 4.3: The force of both beams combined (blue) as well as the force of the individual, counter-propagating beams (orange) in dependence of the velocity of the atom for different detunings and intensities.

For  $\delta_L < 0$  the prefactor of  $\vec{v}$  becomes negative and therefore the force is acting against the direction of motion of the atom, hence damping it. The approximately linear velocity dependence explains the name "Optical Molasses" of this technique. From eq. (17) it can be seen that for a fixed transition the only two free parameters are the detuning and the intensity of the beam. This was already investigated in Fig. 4.2 and is further elaborated in Fig. 4.3. There, it is depicted how the forces of the two counter-propagating beams (orange) produce an effective damping force (blue). For larger detuning higher velocity classes are addressed, but also a larger

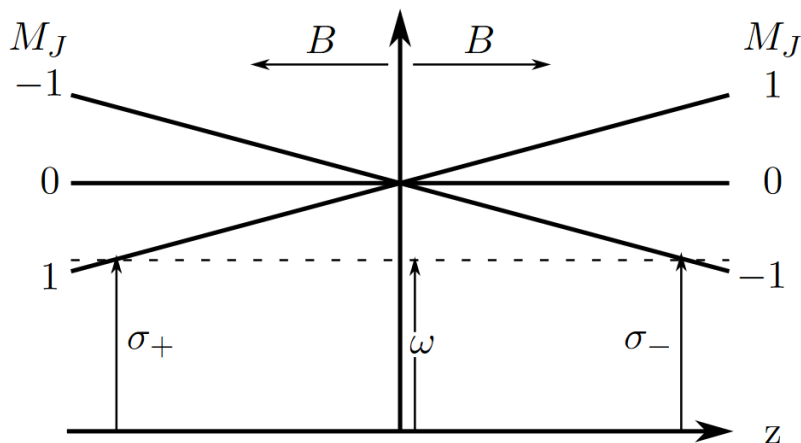


Figure 4.4: The basic procedure to achieve a 1D trap using two red-detuned counterpropagating lasers with opposite circular polarization in the case of a  $J = 0$  ground state and a  $J = 1$  excited state. Taken from [36]

intensity is needed so the influence of both beams does not just decouple like in the bottom left picture. In general, the plots show that there is an optimal intensity for every detuning at which the both beams work together optimally. It does for example not work to just amp up the power as the resulting broadening of the excitation peaks (see Fig. 4.2) leads to a cancelling of both forces over the full range of velocities (top right picture). Reason for this is that it is not important anymore if the atoms are resonant as the scattering rate is already increased because of the large intensities. Typically, the loading rate of a MOT is optimized by adapting the detuning to the available optical power to increase the maximal velocity at which atoms are addressed.

However, this configuration of lasers is not yet a trap, because although the atoms are slowed down, there is no spatial confining force which brings the atoms to one common point. The confinement in position space is achieved by adding a spatially varying magnetic field and in particular a quadrupole field. At the origin and up to a few centimetres away the field has a linear gradient. Additionally, quadrupole fields are in general easy to produce.

In Fig. 4.4 the basic principle how to achieve trapping in the spatial degree of freedom is summarized for the most basic case of an atom described by a two-level system, with a  $J = 0$  ground state and a  $J = 1$  excited state with  $J$  being the total angular momentum quantum number.

The fundamental idea is that by lifting the degeneracy of the total angular momentum quantum number one state is shifted down in energy on the right hand side of the origin and the other state is shifted down on the left hand side. This follows

directly from eq. (15) because  $m_{J0} = 0$  and hence the shift in energy only depends on the sign of  $m_{J1}$ . Only light with the matching polarization can drive a transition with a  $\pm 1$  change of  $m_J$ , therefore it is possible to tune the laser coming from the left towards the resonance on the left side and out of resonance on the right side by choosing the appropriate polarization. The same holds true for the beam coming from the right with the directions inverted. As a result, an atom sitting at  $z \neq 0$  experiences a force accelerating it towards the center.

In the case of Lithium this is more involved as the "cooling beam" drives the transition from the  $F = 3/2$  manifold of the ground state to the  $2^2P_{3/2}$  excited state for which the different  $m_F$  manifolds cannot be resolved. Hence, a transition to each of the four hyperfine manifolds of the  $2^2P_{3/2}$  state are possible and have to be considered. Consequently, the cycle of excitation and deexcitation is not closed, but atoms can relax into the  $F = 1/2$  manifold of the ground state. This poses the need of a "repumper laser" to bring these atoms back into the cooling cycle by exciting them on the D1 line. However, the underlying principle of this more complex case is exactly the same as shown in Fig. 4.4.

Combining the two techniques, namely the red detuning to address atoms moving towards the laser due to the Doppler effect and the installation of a spatially inhomogeneous magnetic field to trap the atoms in position space, also utilizing the red detuned light, enables the trapping in all six phase space dimensions. There, the trapping in the velocity degrees of freedom is synonymous to cooling or decelerating the atoms. The considerations explained in this section are the basis of theory simulations for a two-dimensional MOT which are presented in the next chapter.

## 4.2 2D-MOT simulations

Originally, the goal of the 2D-MOT simulation was to get a qualitative and quantitative insight on the performance of a  $^6\text{Li}$  2D-MOT. The "2D" describes the trapping in two dimensions with one dimension being unconfined for the atoms to exit the trap in a well-defined direction. In the course of the simulation it turned out that getting a meaningful quantitative estimate on the atom flux is highly involved as loss processes as well as the interplay of cooler and repumper lasers, required to describe the cooling cycle of  $^6\text{Li}$ , are difficult to factor in. Therefore, the performed simulations are only in parts quantitative, namely in the parameter space of detuning, magnetic field gradient and intensity. The total atom flux is excluded since it is more susceptible to loss processes than the position of the optimal configuration in parameter space. The influence of the repumper on the optimal values of detuning, magnetic field gradient and intensity is not known for the system and has to be found experimentally.

In general, the simulation calculates the trajectory of an atom leaving the oven, being transversally cooled by the MOT lasers and leaving the chamber through the DPS. The amount of atoms leaving the oven is calculated in Section 2.3. Hence, by extracting the ratio of atoms cooled in the 2D-MOT and leaving it in direction of the glass cell and the atoms not captured, an estimate on the total number of atoms arriving at the 3D-MOT position can be found. The rate of atoms, i.e. the number of atoms per second arriving at the centre of the glass cell, is called the loading rate of the 2D-MOT. The amount of these atoms also captured by the 3D-MOT is called the recapture rate of the 3D-MOT. Typical recapture rates for a system of 2D- and 3D-MOT using  ${}^6\text{Li}$  atoms are on the order of  $10^8 \frac{\text{atoms}}{\text{s}}$  [38].

In the following the results of the simulation and the take away for the final MOT design are discussed.

### 4.2.1 Basic principles of the code

The simulation is done in a semi-classical way by calculating the trajectories of an atom in the force field given by eq. (13). The influence of the Doppler and Zeeman shift is incorporated in the parameter  $\gamma_p$  leading to a force dependent only on the position and the velocity of the atom,  $\vec{F} = \vec{F}(\vec{x}, \vec{v})$ . The strategy for the calculations is outlined in the following.

First, the initial position and velocity of the atom is randomly sampled on the oven aperture, only restricted by the geometry of the oven discussed in Section 2.3. In a second step, the trajectory is calculated iteratively by linearly propagating the position of the atom with its velocity vector for one lifetime of the excited state ( $\tau \approx 27$  ns). Lastly, after one lifetime the position and velocity vectors of the atom are updated, using the force acting on the atom when exposed to the laser beams.

$$\vec{x}_{i+1} = \vec{x}_i + \vec{v}_i \cdot \tau \quad (18)$$

$$\vec{v}_{i+1} = \vec{v}_i + \frac{\vec{F}(\vec{x}_{i+1}, \vec{v}_i)}{m} \cdot \tau \quad (19)$$

As a result, the trajectories for different initial conditions can be simulated and the fraction of the total amount of atoms which enter the differential pumping stage (DPS) is found. This fraction serves as a figure of merit to evaluate the performance of the 2D-MOT for a certain choice of parameters and shall be maximized to ensure best performance.

As the atoms coming from the oven are mainly too fast to be captured by the 2D-MOT, a pre-selection is done by sampling the initial velocities from the low velocity tail of the Maxwell-Boltzmann distribution. A typical choice is shown in Fig. 4.5.

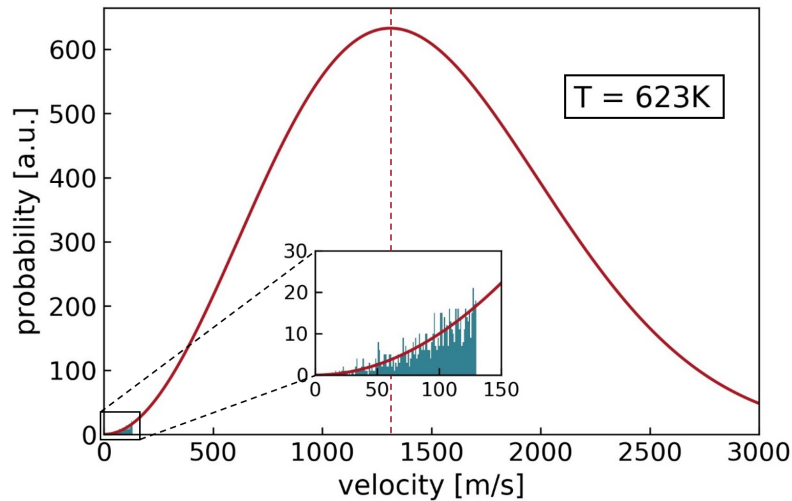


Figure 4.5: The Maxwell-Boltzmann distribution for  ${}^6\text{Li}$  atoms at  $T = 623\text{ K}$  (red). In the inset a typical pre-sampling of low velocity atoms is shown in this case up to a velocity of  $130\text{ m/s}$ .

There, the blue coloured area is the velocity regime of atoms which typically can be captured by a MOT for  ${}^6\text{Li}$  atoms. It is obvious that only a very small amount of atoms leaving the oven is actually captured, in this case only about  $0.07\%$ . For the simulation, this would mean that most of the times the calculation would be done needlessly, hence the pre-selection is done. The results from the simulation are presented in the next paragraphs.

### 4.2.2 Critical velocity

The highest velocity an atom may have for it to still be captured by the MOT is called the "critical velocity". In contrast to common literature it is important to note that the critical velocity is not one number, however it is dependent on the position and angle the atom enters the MOT. To simplify the discussion, in the following the critical velocity describes the maximal velocity an atom may have to still be captured in the MOT given it enters the MOT along the axis connecting the center of the oven aperture and the center of the MOT. In order to get an intuition for this simplification some early simulations are shown in Fig. 4.6.

There, it becomes clear that the critical velocity cannot be constant at all points in space as otherwise either all atoms are captured or none. As expected, atoms entering in the center of the MOT are captured up to the highest velocities because on the one hand they experience the highest intensities and on the other hand because the radius of the MOT is largest in the center and therefore the atom has the most time

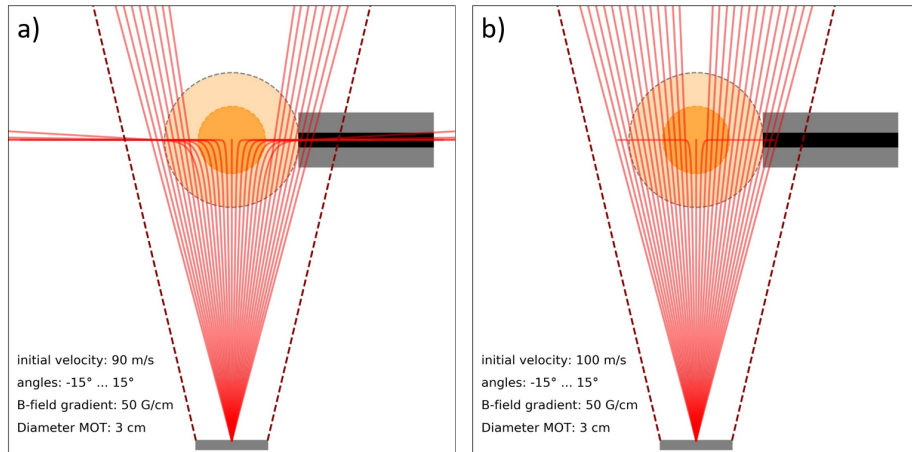


Figure 4.6: A schematic drawing on how to understand the concept of critical velocities. The detuning of the beams is  $-7.5\Gamma$  with  $\Gamma$  the natural linewidth of the transition and the peak intensity is  $10I_{\text{sat}}$  with a gaussian profile shown in dark orange ( $1\sigma$ ) and light orange ( $2\sigma$ ). The absolute initial velocities  $v_0$  are the same for all atom trajectories depicted in red only the initial angle differs. a)  $v_0 = 90$  m/s b)  $v_0 = 100$  m/s. On the bottom the oven aperture (grey) is shown and on the right the differential pumping stage (grey) with the tube opening (black) is depicted.

to scatter a lot of photons to reduce its momentum.

The critical velocity of the MOT is the most important parameter to optimize as the outgoing flux of the MOT scales with  $v_c$  to the fourth power [38]. The critical, also called "capture", velocity of the MOT depends on different parameters. An analytic formula is not given here, but only the qualitative dependencies. First,  $v_c$  depends crucially on the atom and its transition. A broader transition leads to an increase in  $v_c$  since more photons are scattered in the same time. Second,  $v_c$  depends on the size of the MOT beams with a square root. Doubling the size of the MOT beams by a factor of two hence increases  $v_c$  by  $\sqrt{2}$ , resulting in an increase of capturable atoms in the Maxwell-Boltzmann distribution of typically a factor  $\sim 2\dots 3$  in the low velocity regime. Third, an enhancement of the intensity of the beams also raises the capture velocity. However, as shown in Fig. 4.3 this always has to go along with a suitable change of the detuning.

### 4.2.3 Influence of the MOT beam power

The influence of the MOT beam powers on the capture velocity directly translates on the captured flux. The dependence of loading rate and MOT beam power is shown in Fig. 4.7. In the plots the fraction of captured atoms is plotted against the intensity of the MOT beams. The solid line is a guide to the eye. It is surprising that at an

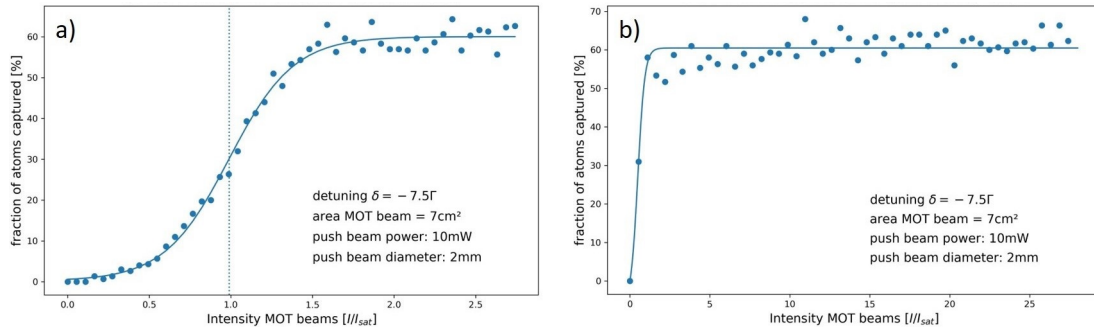


Figure 4.7: Fraction of the pre-sampled atoms leaving the oven aperture that are captured in the 2D-MOT depending on the intensity per MOT beam. On the x-axis this intensity is plotted in units of the saturation intensity  $I_{\text{sat}}$ . a) Low intensity regime b) High intensity regime.

intensity of about two times the saturation intensity ( $I_{\text{sat}} = 2.54 \frac{\text{mW}}{\text{cm}^2}$ ) the capture rate already saturates. One reason could be that the data is obtained by simulations at one specific detuning and to achieve a larger capture velocity the detuning has to be adjusted. However, the influence of the different forces, shown in the first two pictures of the second row in Fig. 4.3, is still weaker than expected. To investigate this further, a comparison to experimental data from an already standing 2D-MOT for  ${}^6\text{Li}$  [38], shown in Fig. 4.8, is done.

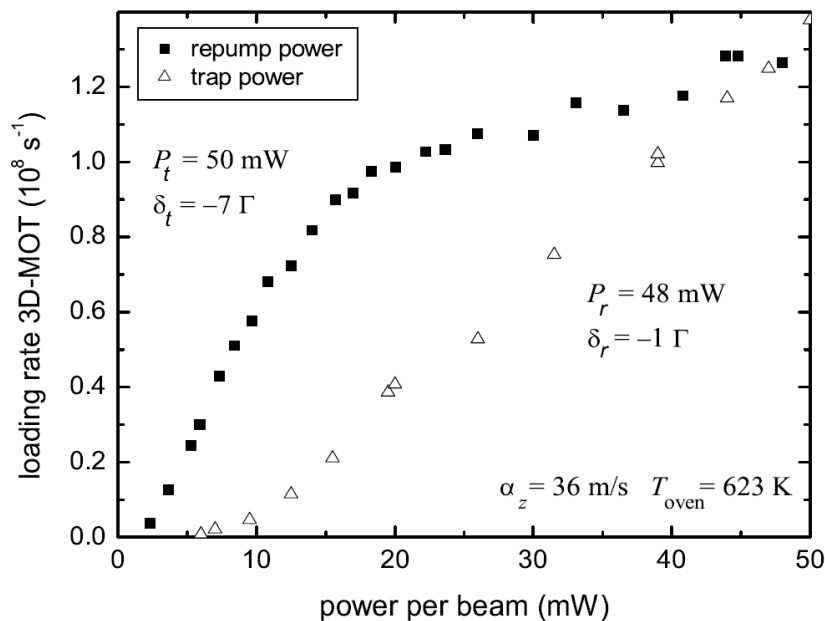


Figure 4.8: The recaptured flux of a 2D-MOT source in a 3D-MOT in dependence of trapping and repumper power. Taken from [38].

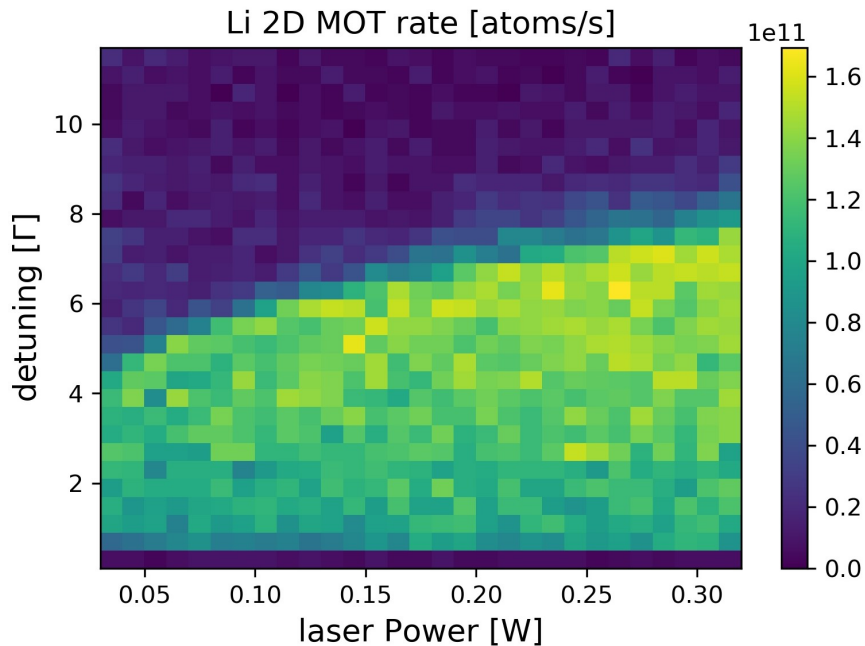


Figure 4.9: 2D-MOT loading rate for varying detuning and optical power. The colourscale is given in atoms/s, however it is possible that these numbers can differ by some factor due to the influence of unknown processes.

There, the fraction of recaptured atoms in the 3D-MOT is plotted against the power in the 2D-MOT beams. The triangles denote the atom flux for different trapping beam and fixed repumper powers while the solid squares show the flux for varying repumper and fixed trapping beam powers. For the repumper beam intensity a starting saturation behaviour is visible. However, for the trapping beam there is no saturation and it even seems that the dependence stays linear over a wide range. The beams in that experimental set-up have a size of about  $2 \text{ cm}^2$ . Hence,  $40 \text{ mW}$  corresponds to  $7.8 I_{\text{sat}}$  in the Fig. 4.7. This discrepancy between theory and experiment could originate from loss effects which are not included in the simulations, but limit the performance in the experimental data. However, this is not yet explained conclusively and will be measured in the new experiment. Concluding from this comparison, a large amount of optical power may still be a possibility for large improvements in the 2D-MOT loading rate compared to already existing experiments.

Therefore, larger beams ( $\varnothing = 3 \text{ cm}$ ) with a lot more total power ( $P \leq 400 \text{ mW}$  per beam) will be realized. It is of large interest if for such high intensities saturation is acquired because if not, it means the flux of a 2D-MOT as the cold atom source is not fundamentally limited in this intensity regime. Hence, more atom flux can be achieved by using more laser power and adjusting the detuning.

Lastly, the plane of power per MOT beam and detuning has been sampled to calcu-

late the influence on the 2D-MOT loading rate. In Fig. 4.9 an increase of loading rate with increasing power and detuning is visible. However, just like earlier the increase is expected to be much larger. The exact reason is unknown and has to be cross-checked with experimental data. In general, the colourscale describing the total atom flux is not to be understood quantitatively, but only qualitatively. A comparison with the measured data shown in Fig. 4.8 is thus not possible.

One additional interesting fact to draw from the simulation is the strong decrease at larger detunings if the intensity is too low. This suggests that in the final set-up the detuning probably won't exceed  $10\Gamma$  which is an important information to plan the optical set-up to prepare the laser beams. In particular, the dynamic range of the AOMs used is mainly determined by this information.

#### 4.2.4 Influence of the push beam

In Fig. 4.6 the mirror symmetry between atoms flying to the right and to the left after being exposed to the 2D-MOT lasers is obvious. If an atom moves to the right after being transversally cooled or to the left is therefore completely dependent on the initial conditions it has when leaving the oven aperture. However, this is undesirable for building a high flux atom source as half of all atoms are lost inherently. One solution to fix this is by using a so called "push beam" to push the atoms in the right direction, i.e. in direction of the DPS. The push beam typically has a small diameter of about 1 - 2 mm and travels in direction of the 3D-MOT to accelerate atoms moving left in Fig. 4.6 to the right and consequently make them capturable for the 3D-MOT. Although, the push beam can increase the atom flux by up to a factor of two as atoms originally moving away from the DPS are accelerated towards it, some caution has to be taken. Reason for this is that the beam will also influence atoms moving in the right direction, even if due to the red-detuning mainly atoms propagating towards the push beam will be addressed. In a worst case, this can lead to atoms being accelerated to velocities faster than the capture velocity of the 3D-MOT. Hence, the effectiveness of a high flux loading scheme using a 2D-MOT is greatly reduced if the longitudinal velocity of the atoms is too large for the 3D-MOT to be loaded.

Furthermore, an increase in push beam power reduces the effective time each atom spends in the 2D-MOT cooling volume. The resulting influence of the push beam on the velocity profile of the atoms entering the DPS is shown in Fig. 4.10. With increasing push beam power (different colours) the center of the longitudinal velocity distribution (Fig. 4.10 a)) shifts to higher values and broadens. The shift is due to the acceleration by the push beam. The broadening on the other hand can be explained because a larger range of initial velocities is acceptable for the MOT to still capture

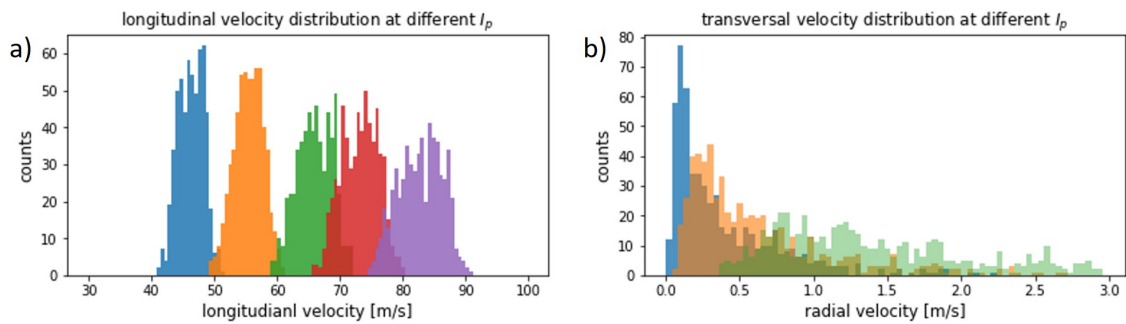


Figure 4.10: Influence of the push beam on the a) longitudinal velocity distribution for different push beam powers  $P = 1, 2, 4, 6, 10$  mW (color scheme left to right) b) radial velocity distribution (colors matching the scale in a)).

the atoms as both initial directions, left and right, are capturable. Resulting from the lower time an atom spends in the MOT, the transversal cooling is reduced which can be seen picture b) of Fig. 4.10 as the transversal velocity distribution broadens and shifts to higher values.

This effectively increases the divergence angle of the cold atom beam and therefore clipping at the edges of the DPS can increase, lowering the overall flux. Additionally, the position atoms inside the cold atom beam hit the 3D-MOT capture volume can be further away from the center, effectively influencing the loading behaviour. The DPS has been designed in a conical manner based on the results of the beam divergence from this simulation.

#### 4.2.5 Conclusions for the design

From these simulations some general requirements for the design of the optics as well as the magnetic fields is drawn. The main take away is the need to maximize the capture velocity of the MOT. This is done by increasing the size of the MOT beams. As long as optical power is not the limitation it is advisable to use as large beams as possible and to use round beams rather than elliptical beams. That is because, although making beams elliptical increases the intensity, it also reduces the capture radius. For this experiment a lot of optical power at 671 nm is available due to the TA-SHG laser system used (see Section 4.3.2), thus round beams are the most practical solution.

Another feature to consider to optimize the 2D-MOT performance is the waveform of the ingoing light. Typically, it is gaussian and therefore the intensity on the edges will be greatly reduced. One could use much larger beams and let them clip on the viewports to make the density on the aperture larger, however this is very inefficient

in terms of power exploitation. As a solution to increase the intensity over the full MOT beam size, optical diffusers which engineer the wavefront to be flat-top-like can be introduced into the system. This is discussed in-depth in Section 4.3.3.

To further increase the power available per MOT beam, the beams can be retro-reflected to recycle the laser power. By building the optics in a "Bow-Tie" configuration (see Section 4.3.1) up to a factor of four in laser power per beam can be gained. These two features will be the main innovations to boost the loading rate of the 2D-MOT.

Besides increasing intensity and detuning to improve the MOT loading rates, also fine tuning of the push beam intensity and detuning showed to have an influence on the loading behaviour of 2D- and 3D-MOT. Therefore, control over beam size, power and divergence of the push beam is desirable. In this context, also the atom beam divergence has been discussed. Consequently, it is desirable to have 2D- and 3D-MOT as close together as possible to reduce the absolute spread of the atoms to increase the recapture rate in the 3D-MOT. Hence, the importance of compactness of the vacuum system is another result found in this simulation. The influence of gravity is negligible in the case of Lithium as the atoms are fast enough and therefore do not have time to cover a large distance during the free fall inbetween the MOTs. In a rough estimation, it turned out for typical values of the longitudinal velocity of atoms leaving the 2D-MOT that the maximal separation from the center of the 3D-MOT due to atom beam divergence is about 3 mm and due to gravity only about 0.2 mm.

The influence of the magnetic field gradient has not been investigated closely, but the simulations have been carried out at a moderate gradient for which the MOT worked well. This gradient and also a wide range of gradients above and below can be reached in the experimental set-up using permanent magnets. The exact positioning of the zero crossing of the magnetic field on the other hand is much more crucial as it is the main tuning parameter for the position of the 2D-MOT and its orientation with respect to the differential pumping tube.

The last aspect to draw from the simulations is the possibility to always increase the 2D-MOT loading rate by increasing the temperature of the oven. An increase of 50 K of the oven temperature yields an increase of one order of magnitude in the outgoing flux, posing as a powerful tuning knob for the 2D-MOT loading rate. However, one drawback is that the lifetime of the oven will be reduced by one order of magnitude, too. For experimental cycles in which MOT loading times start to become a limitation, this could be a temporary solution.

## 4.3 Set-up of the 2D-MOT

In the following, the mechanical set-up of the 2D-MOT and the surrounding components are described. At the time of this thesis a 2D-MOT was not realized yet, therefore a characterization of the individual parts is given.

### 4.3.1 Optical Bow-Tie configuration

As explained earlier, the easiest way to increase the capture velocity of a MOT is by increasing intensity and detuning of the trapping beams. Additional laser power is limited by the available laser sources. It is always best to use the available power as efficient as possible which is even more important in the case of a power-intensive set-up like a 2D-MOT. Here, power can be saved by using one laser beam not only for one of the four MOT arms, but for two respectively four. This can be done by either retro-reflecting a beam onto itself, resulting in the need of two separate laser beams or by reflecting one single beam in a so called "Bow-Tie" configuration to use it for all four MOT arms. This saves a factor of two or four of optical power, respectively. The bow-tie configuration for this experimental set-up is shown in Fig. 4.11.

The optical path for the MOT trapping beams is as follows: The beam is first coupled out from a fibre by an asphere to a collimated size of 2 mm. Then, it is send through a polarizing beam splitter (PBS) to clean the polarization and afterwards send onto an optical diffuser (discussed in Section 4.3.3). The exiting divergent light is collimated again by a 2" achromatic doublet to a flat-top diameter of 30 mm. The polarization is changed to circular polarization by a  $\lambda/4$  waveplate. The beam then passes the atom cloud for the first time and the polarization is changed back to linear by a second  $\lambda/4$  waveplate. Reason for this is that a reflection under an angle on the mirror would induce a change of phase between s- and p-polarized light, effectively disturbing the circular polarization. To keep control over the polarization all reflections are done with linearly polarized light. After the second reflection and before the beam passes the atoms a second time a third waveplate changes the polarization of the light back to circular. A mirror with a quarter waveplate in front closes the cycle, reflecting the beam onto itself. After the reversed cycle, the beam is then dumped next to the PBS cube which was used to clean the polarization. Behind the retro-reflection mirror a photodiode is located to measure the intensity leaking through the mirror. Using this information, the intensity of the MOT beams could be stabilized in the future if necessary.

For both possible configurations (double retro-reflection or bow-tie) there are advantages and disadvantages which shall be discussed in the following. Obviously, the main advantage of the Bow-Tie configuration is the increase in optical power. As

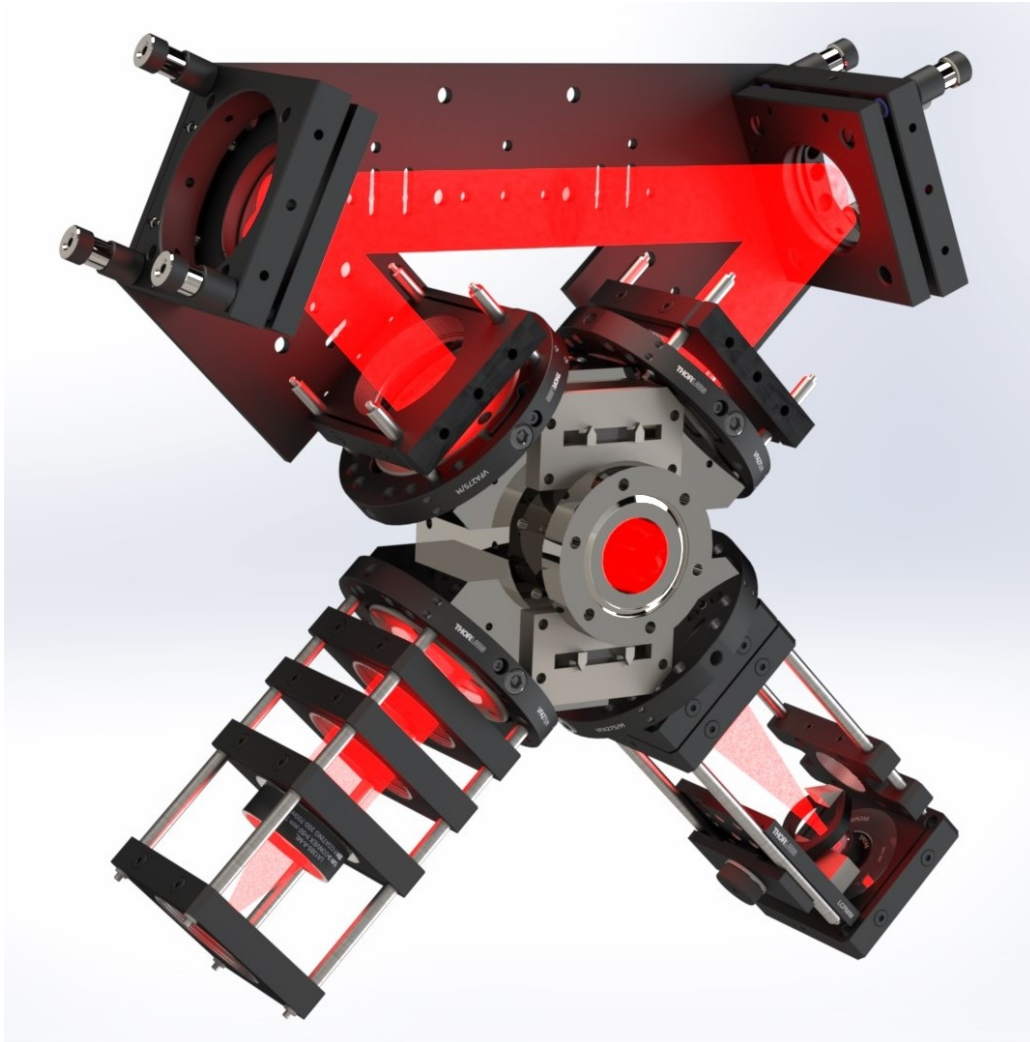


Figure 4.11: The 2D-MOT chamber with the optical bow-tie configuration optics around. The beam gets coupled in on the bottom right side, is reflected by two mirrors on the top mounting plate and finally gets retro reflected onto itself on the bottom left side. The 2D-MOT chamber is made from titanium and on the front side the two mounting plates for the permanent magnets can be seen above and below the CF40 flange.

this can directly increase the loading rates of the MOT and thus decrease the cycle times of the experiment it is an invaluable advantage which should be picked up as long as one is in the regime in which more laser power still corresponds to higher loading rates. A challenge this configuration poses is the coupling of the degrees of freedom for all beams and therefore the inability to tune them independently. That could pose a problem later on when the MOT has to be aligned with the DPS. Then, the alignment of the magnetic field and the direction of the push beam are the only alignment parameters to tune the atom beam direction. However, it shall be noted that the alignment of the MOT with the position of the magnets which produce the quadrupole field is in principle the most accurate way to align the system as it brings it closest to theoretically optimal configuration. On the other hand it is also the most tedious way of alignment. To simplify the alignment procedure, mounting plates for the permanent magnets have been designed to adjust and control their exact position more comfortably (visible in Fig. 4.11).

A physical limitation could be met in a Bow-Tie configuration when the absorption of the atom cloud and correspondingly the optical density is so high that the intensity in the retro-reflected beams is considerably lower than for the first passes through the atom cloud. One result could be an asymmetry of the MOT which has to be compensated. For the 2D-MOT set-up in this experiment it is expected to operate in the well-saturated regime as up to one Watt of optical power is available and therefore the effect of the cloud casting shadows on the reflected beams is expected to be small.

One advantage of the two separated MOT beams is that the ratio of the intensities in both beams is a degree of freedom to align the MOT with the DPS. However, other than fixing the MOT position using the position of the magnetic field zero crossing this approach does not yield a theoretically optimal configuration. It is however much easier to optimize.

As the 2D-MOT system is supposed to be set up once, aligned to optimal configuration and then be stable and not be modified again, the advantage of easier and more versatile tuning does not outweigh the advantage of having double the optical power. For that reason the optical bow-tie configuration is chosen in this experimental set-up.

#### **4.3.2 Laser system TA-SHG**

The main driving force suggesting that in this experiment the 2D-MOT loading rates can be higher than in already existing set-ups is the high power Toptica TA-SHG laser system [39]. The influence of power on the loading rates was discussed in Section 4.2.3. The name TA-SHG is an abbreviation for Tapered amplifier - Second

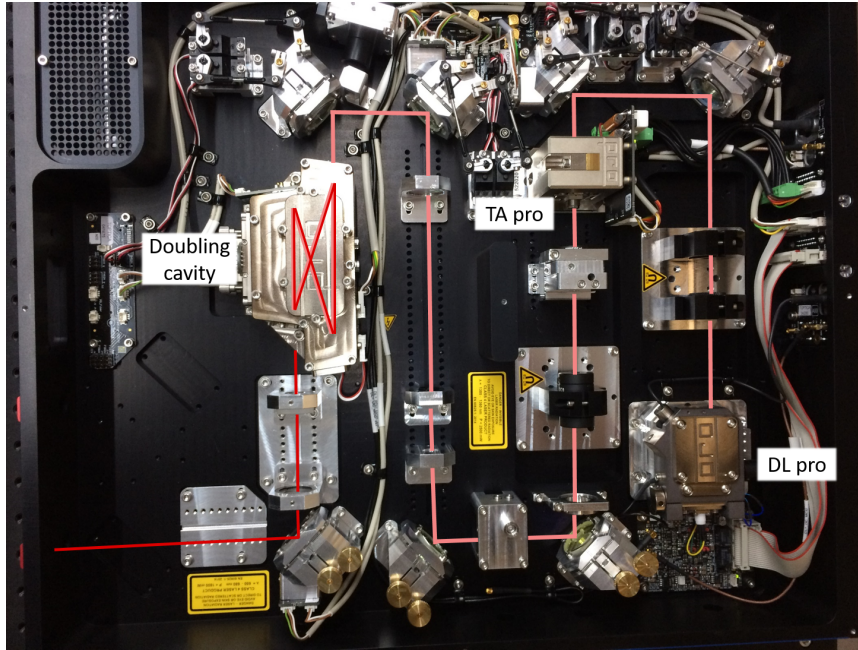


Figure 4.12: The beam path inside the TA-SHG unit. In light red the 1342 nm beam is shown while the 671 nm light is depicted in dark red.

Harmonic Generation. It has an output power of one Watt at 671 nm in a very clean mode which lets one couple about 800 mW of laser light into a fibre. Compared to for example the TA pro system this makes up a factor of  $>2$ . The decisive innovation for the TA-SHG is the frequency doubling cavity which converts laser light at 1342 nm via the non-linear process of second harmonic generation inside a crystal to light of half the wavelength, namely 671 nm red light. The advantage of this is the greater efficiency of tapered amplifiers at larger wavelengths, resulting in powers of up to 2.5 Watts of 1342 nm light coming from the amplifier which is afterwards converted to red light in the SHG. In Fig. 4.12 an inside look of the TA-SHG laser is shown.

In the following, the optical path is summarized briefly. The 1342 nm comes from a DL pro laser diode and its mode gets cleaned first. With two remotely adjustable mirrors the beam is coupled into the tapered amplifier in which it gets amplified to about 2.5 W. Mode cleaning and additional beam expansion is done before coupling into the SHG cavity. In the cavity the beam gets reflected in a "Bow-Tie" configuration, passing the doubling crystal in every cycle. Through the outcoupling mirror only 671 nm light, produced in the crystal, can leave the cavity. After the cavity the light is mode cleaned one last time and send to the output of the laser with a power of slightly above one Watt.

The fact that a cavity is already implemented in the optical set-up has the additional benefit of strong suppression of the incoherent background of the laser diode.

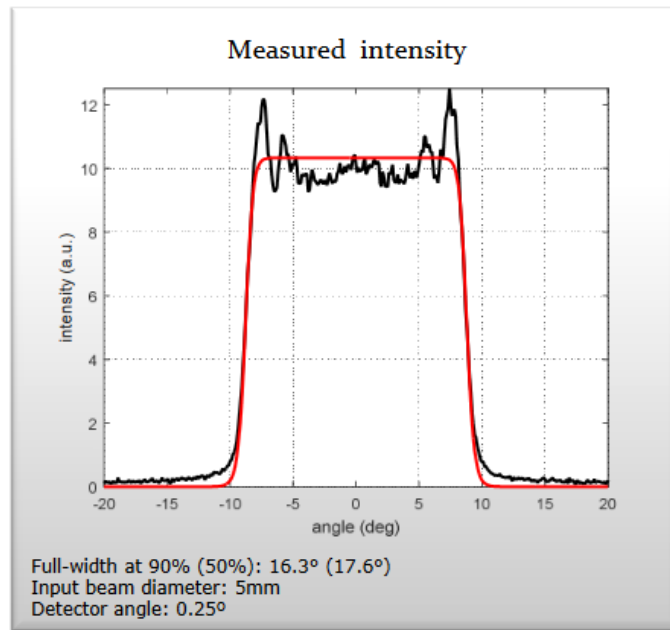


Figure 4.13: The theoretical outgoing intensity profile specified by RPC Photonics. In red the desired intensity distribution is plotted while in black the measured data is depicted. The peaks on the edges of the profile are visible in the measurements below as a bright ring. Taken from [40].

### 4.3.3 Optical diffuser

To optimize the amount of light that can be sent into the 2D-MOT chamber through the viewports with 30 mm diameter with respect to the light that is clipped at the edges, the gaussian profile of the laser beam is converted to a flat-top shape. This is realized by an EDC-15 optical diffuser by RPC Photonics [40]. This diffuser is made from a polymer of varying thickness on the order of some tens to hundreds of micrometer, adhered on a glass plate. The exact height pattern of the polymer converts the gaussian profile to a flat-top by using interference effects of the spherical waves of all points on the diffuser. As a result the diffuser makes the incident collimated beam divergent in a predefined angle. From the angle an appropriate focal length for the collimation lens can be chosen to achieve a final beam size of 30 mm. The theoretical outgoing intensity profile of the diffuser is shown in Fig. 4.13.

Compared to a gaussian profile which has still about 13.5% of its power further than one waist away from the center, the flat-top beam has very sharp edges. This is also visible in the measured profiles in Fig. 4.14. However, while characterizing the diffuser one limitation became obvious, namely the trade-off one has to make between the divergence of the re-collimated beam and the influence of specks on the profile. In other words, improving the quality of the profile increases the divergence

of the beam. The reason can be understood intuitively: The flat-top intensity profile becomes smoother if the size of the incident collimated beam is increased because more individual spherical waves interfere to make up the intensity pattern. The measured intensity profile shown above is for example realized for an input beam size of 5 mm. Using smaller beams worsens the performance as speckles are introduced. On the other hand, it is convenient to work with small beams as the divergence of the re-collimated beam is dependent on the extent of the beam source and increases for larger incident beams. For example, in the limit of an infinitely small beam source, i.e. a point source the divergence length of the outgoing beam is infinitely large for a lens that is infinitely conjugated. However, for an extended beam source there is a residual wavefront curvature and thus the beam is slowly diverging.

In conclusion, the ingoing beam waist shall be as large as possible to still achieve a divergence which allows a bow-tie configuration, i.e. an optical path length of about 1.5 meters. The intensity profile for one possible configuration measured at different distances from the collimation lens is presented in Fig. 4.14.

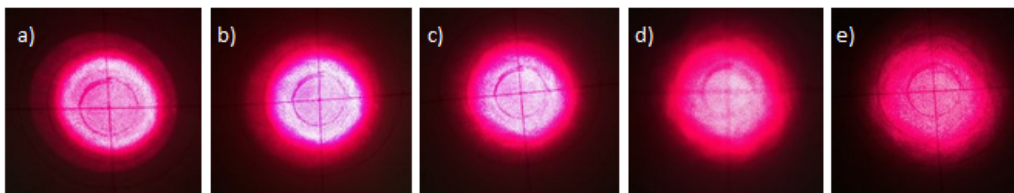


Figure 4.14: A picture of the intensity profile after a) 10 cm b) 50 cm c) 100 cm d) 150 cm and e) 150 cm with different illumination. The inner drawn ring has a diameter of 2 cm. The pictures were taken only qualitatively as there was no large enough camera to characterize a beam of this size.

For larger travel lengths the edges start to blur and more intensity is shifted outwards. Up to one meter the beam still looks very good and especially the sharp edges of the 3 cm wide, bright area in the middle remain well-defined. For 1.5 meters the beam profile starts to worsen, but is still acceptable for a MOT beam.

Some additional comments on the diffusers shall be made: First, the polarization of the ingoing light is not affected by the diffuser. This is crucial for the operation of the MOT. Second, the divergence of the outgoing beam can be slightly reduced by giving the incident light a small wavefront curvature. Third, the dependence of beam divergence and ingoing beam waist shows an approximately linear behaviour from which can be concluded that the ingoing beam should be smaller than about 2 mm in diameter.

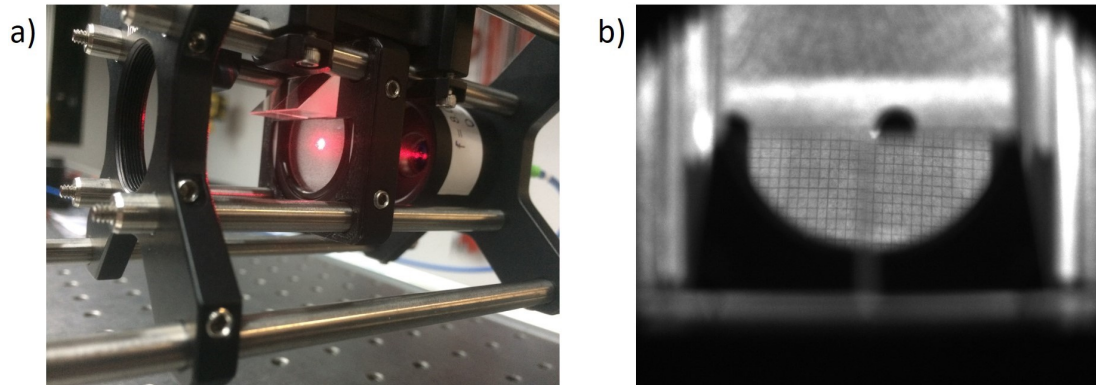


Figure 4.15: a) The imaging set-up along the incoupling beam axis. In the center the optical diffuser with two right-angle mirrors is visible. From the right the light is coupled in and outside the picture on the left the  $f = 100$  mm achromatic doublet and the quarter waveplate are mounted. Above the right-angle mirrors a camera with an  $f = 6 - 15$  mm tunable objective is located. b) A picture of a millimeter paper located in the atom plane taken by the camera. The field of view of this set-up along the extent of the MOT is about 2 cm.

#### 4.3.4 Imaging

One major disadvantage of the design of the 2D-MOT chamber is that it has no unused viewports to image the 2D-MOT as it was designed to be as small as possible. This would be a powerful addition to monitor the performance and the orientation of the 2D-MOT. In the design used for this experimental set-up the 2D-MOT can only be monitored along the push beam axis. However, to triangulate the full orientation of the MOT in 3D a second measurement along a different, partly orthogonal axis, is necessary. As a solution for this task, a more involved imaging procedure is implemented alongside the incoupling beam axis of the MOT. The underlying idea is to have the achromatic doublet which is used to collimate the light from the diffuser to be at a distance from the center of the MOT equal to its back focal length. In this way the fluorescence light of the MOT is collimated by the lens and a small fraction can be reflected out by a right angle mirror onto a camera. The set-up and a picture taken by the camera is presented in Fig. 4.15.

In this way a measurement of the 2D-MOT alongside a second axis, additional to the push beam axis, is possible and hence a complete triangulation of position and orientation of the MOT. The optimization of the imaging set-up will be done in-situ. The coarse alignment was done in a test set-up and resulted in a field of view of about 2 cm in the plane of the 2D-MOT. This is limited by the aperture the 1.5" quarter waveplate imposes and can hence be easily increased if necessary.

To access the light along an already occupied axis works in general, but there are still different parts to optimize. In particular, a custom machined or 3D printed mount to hold diffuser and camera objective could give more flexibility to adjust the camera in a way that it has the largest field of view in the direction of the 2D-MOT. Also, the fine tuning of the magnification of the imaging set-up will be done when a first characterization is done.

Besides these minor improvements an order of magnitude estimation showed that the fluorescence light coming from the atom cloud should be bright enough to get a large enough signal-to-noise on the camera to accurately identify the 2D-MOT in the pictures.

### 4.3.5 Magnetic quadrupole fields

The magnetic quadrupole fields for the 2D-MOT are done with four stacks of permanent magnets located around the chamber. The chamber itself is made from titanium to reach as low magnetic permeability as possible. The choice to use permanent magnets instead of magnetic field coils like for the 3D-MOT is justified mainly by considering the influence of stability and tunability on the system. As described earlier, the 2D-MOT is designed in a way to be optimized once and then run as long as there is lithium in the oven. Tunability of the magnetic fields is therefore only required to optimize the 2D-MOT faster or more easily. Stability on the other hand is the main focus of the set-up and therefore out-weights the tunability aspect. As a result, permanent magnets which are very stable, but more difficult to tune, are used instead of coils. Also, coils require additional cooling and current stabilization which is not the case for the permanent magnets, making them cost efficient and easily usable. The magnets of choice are Neodymium magnets with a magnetisation of  $m = 0.65 \text{ Am}^2$  per magnet. The magnets are distributed to four locations around the chamber in stacks of six to eight magnets, depending on the required magnetic field gradient. The position of the magnets is fixed using custom mounts made from titanium which have a fine scale engraved on the side to precisely measure and control the position of the magnets to make optimizing the MOT more convenient.

The exact simulations of the 2D-MOT fields, depending on the number of magnets and their positioning is discussed in [18].



# 5 Conclusion and Outlook

## 5.1 Conclusion

The main focus of this thesis was the design and set-up of a versatile and fast quantum simulator for fermionic  ${}^6\text{Li}$  atoms in reduced dimensions. The status of the experiment at the time of the end of this thesis is shown in Fig. 2.9. During the construction, not only the vacuum set-up, but also the laboratory infrastructure was built up and adapted to the needs of the experiment.

In summary, a compact vacuum system has been designed, built up and pumped down to pressures of  $p_{\text{UHV}} \approx 4 \cdot 10^{-11}$  mbar and  $p_{\text{HV}} \approx 2 \cdot 10^{-10}$  mbar. In particular, the short timescale of about 30 hours of pumping to achieve these pressures shall be emphasized. This is a direct consequence of the small volume of the chamber as well as the newly incorporated high-performance pumps.

Besides the vacuum set-up, the cold atom beam source was designed and in parts built up, starting from the design of the Lithium oven and its thermal isolation and ranging to the set-up of the optics and their characterization. In this context, a simulation of the 2D-MOT was done and the optics were optimized accordingly by using both optical diffusers, to increase power efficiencies and loading rates, as well as a new imaging scheme. Both accompany the goal of short cycle times and an increased level of characterization of the system. An atom beam flux from the 2D-MOT of  $> 10^{10} \frac{\text{atoms}}{\text{s}}$  is expected due to larger beams, more laser power and an optimized beam profile of the cooling beams.

Additionally, the design of the 3D-MOT quadrupole and Feshbach coil geometry has been worked out, including the implementation of tunable magnetic field curvature, fast magnetic field jumps and efficient cooling.

In general, in the course of this thesis the underlying idea to make the experiment compact and modular as well as implementing possibilities to characterize the system at all essential points was given a high priority in every design step. It again should be stressed out that the basis to enable modularity and characterizability is the precise control and decoupling of the degrees of freedom of the system. By putting effort

in this precise control, various benefits like efficient debugging of the full system as well as of individual subsystems, sophisticated sequences of optical modules and propagation of measurements throughout the experiment are possible.

## 5.2 Outlook

In this Outlook a brief overview on the next steps in building up the HQA experiment and improving it to be a fully operational quantum simulator is given. It should be noted that many of these projects are already in ongoing process and the in-depth description will be given in the theses of coming years.

### 5.2.1 Magnetic field coils

As the theoretical groundwork has been laid in this thesis, the actual construction of the magnetic field coils is still an involved task. Precise winding to achieve high fidelity magnetic fields as well as thorough characterization of the system are key to produce magnetic fields which are capable to match theoretical expectations. In this regard, the usage of 3D-printed guiding forms to wind the coils might improve the overall quality.

Here, one example of a project which is possible with this next generation of coils is presented. The momentum state imaging perfected in this group [41] can be upgraded to enable in-situ imaging with a fixed magnification. The theory and experimental implementation can be found in [41][42]. This is realized by doing a  $T/4$  expansion in a shallow magnetic trap which is present due to the magnetic field saddle. This maps the initial momentum of the atoms onto a spatial position, effectively acting as a Fourier transform. By letting the system evolve for a second  $T/4$  in a trap with larger trapping frequency, a transition to a magnified in-situ space is performed. The ratio of the trapping frequencies yields the magnification of the in-situ image. Therefore, a tunable field curvature enables to tune the magnification of the in-situ imaging and can hence be a valuable tool for improving measurements of momentum and spatial correlations. In combination with an increase in cycle rates this might enable the measurement of higher order correlations.

### 5.2.2 RF and Microwave antennas

As mentioned in Section 2.3 the use of a glass cell supports the use of more involved antenna systems to drive RF and microwave transitions between different hyperfine levels of Lithium. Since there is no metal which could act as a resonator, especially for the microwaves with wavelengths on the order of a few tens of centimetres, one can

think about designing tunable and strong antennas which can increase the Rabi rates of transitions between different hyperfine states. As a result, it can strongly increase the fidelities of the deterministic preparation of ground state systems which becomes even more influential for larger system sizes. Reason for this is that typically a certain transition has to be done for all atoms and hence the final preparation fidelity scales exponentially with the number of atoms in the prepared state.

A well thought through concept for microwave and RF antennas is hence essential for future scalability of systems of interest (like higher particle numbers) and the overall performance of different experimental cycles.

### 5.2.3 SHG Laser set-up

For the 2D- and 3D-MOT five beams at two wavelengths each are required. One for the 2D-MOT in bow-tie configuration, three for the 3D-MOT and one for the push beam. For each of those, cooler and repumper beams to close the cooling cycle transitions are necessary. To adjust the frequency of the beams AOMs are used which should have a dynamic range of some tens of MHz to first capture the atoms in a big MOT at large detunings ( $< 10\Gamma$ ) and then compress the MOT by lowering the detuning to transfer it into an optical dipole trap. The preparation of the beams and their distribution can either be done by a customly available solution (like from Schäfter & Kirchhoff [43]) or by a home build distribution system.

Here, the implementation of the improved secondary cooling circuit will be implemented for the first time to on the one hand cool the base plate of the SHG unit and on the other hand cool the AOM amplifiers in a modular fashion which will make the cooling of various small heat sources on the optical tables a lot easier.

### 5.2.4 532 and 1064 nm laser systems

At 532 and 1064 nm strong laser sources are available with powers of tens or hundreds of Watts. Therefore, they can be used to produce attractive, red-detuned (1064 nm) or repulsive, blue-detuned (532 nm) optical dipole traps. In the standing experiments only red-detuned traps are implemented, but the use of blue traps can also have many advantages. Since the implementation of these laser systems will be realized on a longer timescale, here only one idea why to use blue dipole traps is summarized.

The transition from the MOT into an attractive optical dipole trap or an optical tweezer in which evaporation cooling is done can severely limit the cycle rates of an experiment because the timescale of the transition is limited by the thermalization time of the atoms. This might be improved by increasing the density of the atomic

cloud as it effectively shortens thermalization timescales. One idea is to use a blue detuned ring along the vertical direction and two blue sheets in the horizontal plane to confine the atoms from the MOT in a 3D cylinder and then moving the sheets towards each other. As a result, the density is increased and simultaneously a 2D system is loaded. For increased 2D trap frequencies the implementation of a blue  $\text{TEM}_{10}$  mode is a possibility as it has the additional advantage of only loading precisely one sheet.

The advantages of 532 nm traps are also smaller scale features due to the factor two in wavelength which makes the smallest scales also a factor of two smaller. Additionally, because blue-detuned traps confine the atoms at the position of no light, very homogeneous and large systems like box potentials can be produced. Most likely, a combination of blue and red detuned potentials from the top through the high NA objective as well as from the side through the smaller 0.3 NA Mitutoyo objective will be implemented.

### 5.2.5 Optical modules

One main feature of the final design for this experiment should be the modularity and scalability of the system. Although this was addressed at different points throughout the thesis there is no clear solution yet how to build optical modules which can be easily connected while keeping the beams passively aligned. Here, one proposal is made.

To be able to connect optical modules, an interface between the modules is required. This has to address two tasks. First, it has to connect the two modules always in the exact same configuration to ensure repeatability and interchangeability of different modules and second, it has to enable the characterization of the beam at the interface position. If such an interface is designed, the optics inside the module can be arbitrarily complicated as the only thing which has to be guaranteed to ensure passive alignment is that the wavefront at the interface has some predefined shape. In other words, the center position, the size, the angle and the polarization of the beam going in and coming out of a module must always be predefined and constant. As a result, the optics inside the module can be aligned once to match these conditions and the performance of the module can afterwards be monitored by measuring the above mentioned features of the beam at the in- and outlet, making an optical module effectively a "Black Box".

### 5.2.6 High-NA objective

During the time of this thesis there were intensive discussions on what kind of high NA objective to use. In the already existing experiments, self-build 0.55 NA objectives are implemented which correspond to an half-opening angle of about  $33^\circ$ . As the glass cell supports a NA of up to 0.9 and the nano-textured viewports support large angles of incident of up to  $55^\circ$ , the idea is to increase the numerical aperture of the objective below the glass cell to increase the fraction of captured photons for fluorescence imaging. In Fig. 5.1 the collected fraction of scattered photons for fluorescence imaging in dependence of the numerical aperture is shown, also considering the dipole radiation pattern of the emitted photons.

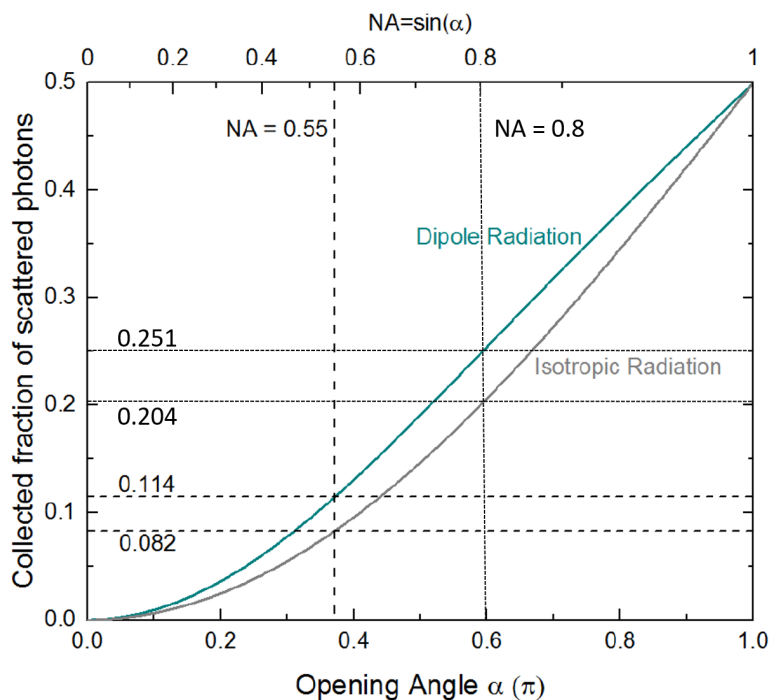


Figure 5.1: The number of scattered photon considering the dipole radiation pattern (blue) or an isotropic radiation (grey) in dependence of the full opening angle (bottom axis) or the numerical aperture (top axis). In the picture the exact values for the existing 0.55 NA objectives as well as for a possible 0.8 NA objective are shown. Adapted from [44].

Hence, one can draw the conclusion that increasing the NA to 0.8 would lead to an increase of captured photons by a factor of 2.2. Consequently, the time of flashing during the imaging process, i.e. the time in which the atoms are exposed to resonant light for imaging, can be reduced by the same factor. As the resolution of images with single-atom resolution taken in free-space [45] is limited by the Brownian motion of the atoms during the exposure time, the resolution of the imaging technique

is effectively increases. The enhanced resolution scales with the flashing time  $t$  like  $\propto t^{\frac{3}{2}}$  [46], hence has a strong influence on the size of pictures of single atoms. On the other hand, this size limits the number of atoms which can simultaneously be imaged in the field-of-view of the objective without the atom images overlapping. Therefore, an increase of the numerical aperture increases the maximal size of systems that can be studied with this apparatus.

By keeping the flashing time fixed, more photons are captured per atom due to the larger solid angle covered by the objective. Thus, a better Signal-to-Noise ratio can be achieved which could in turn reduce the effort one has to put into the imaging set-up and potentially enable the use of different cameras.

On the other hand an increase of the numerical aperture would also enhance the diffraction limited resolution of the objective and therefore enable the observation of smaller features in e.g. optical lattices, using the experiment like a quantum gas microscope, or for the in-situ observation of small few particle systems like a double-well potential or a 2x2 lattice. Due to the larger NA also the trap frequencies of tweezers done by the objective would increase.

Despite these advantages, using a larger NA also poses challenges which have to be addressed. First, the objective becomes larger and heavier as the required lenses become bigger which can pose challenges for stable mounting. Concerning mounting, high NA objectives are also inherently more susceptible to misalignments such as tilt between the objective and the viewport. In the design of an 0.8NA objective by the company "Special Optics" [47] the tilt is required to be below 0.3mrad to ensure diffraction limited performance. This issue was addressed by implementing a precise control of all angles using spacers with different heights, but this solution still has to be verified in the real set-up. Furthermore, as the system becomes more complex it can get harder to use the objective in reverse to get the vertical MOT beams into the glass cell. It also gets even more difficult when the objective has to fulfil additional requirements like in the present case: The idea is to merge different parts of the optical path which normally could pose problems or are difficult to build with the objective. In particular, it means that the input aperture of the objective should be small ( $<1''$ ). As a result, one can work with small lenses making all optical paths shorter and reducing the aberrations of the lenses behind the objective. This could normally be done by a telescope, but as the beams exiting the objective are typically very large (2" optics) the beam paths for such telescopes become very long. Therefore, it is much more convenient to integrate this inside the objective where it can be implemented by adjustment of the lenses in a much smaller space.

Another very powerful feature of an objective would be to have the Fourier plane, i.e.

the plane in which a collimated beam sent through the objective in reverse comes to focus, outside of the objective as it would enable manipulation of the beam in the Fourier plane like small retro-reflecting point mirrors for MOT beams or a vertical lattice.

However, it does not seem possible to merge all of these features together at large NA, in particular to have the Fourier plane outside of the objective at  $NA > 0.65$ . Therefore, a prioritisation is necessary which also depends on the final design of the company. Regarding this, no final decision has been made at the time this thesis is written. In the end, most likely the objective with the largest NA which still has a Fourier plane lying outside of the objective and a small input aperture will be the best option. Thus, the NA will be around 0.65-0.7 NA.

The advantage of these features for the optics leading to the objective and the decrease in susceptibility to misalignment outweigh the advantages from capturing more photons per atom. Reason for this is that with the cameras in use, one is already in the regime of single atom resolution in free space images [46] and will not make fundamental improvements in this regard. Also, the use of for example sCMOS cameras with global shutter to take two consecutive pictures very fast might be already possible with objectives on the order of  $\sim 0.6$  NA.

In summary, the high NA objective as well as all other projects mentioned above are designed and built to do a next step towards programmable quantum simulation in an experiment which is stable, fully characterized and versatile in the systems it can investigate.

## References

- [1] Lande, Daniel R. (2014) "Development of the Binary Number System and the Foundations of Computer Science". *The Mathematics Enthusiast*: Vol. 11 : No. 3 , Article 6.
- [2] A. G. Bromley, "Charles Babbage's Analytical Engine, 1838". *IEEE Annals of the History of Computing*, Vol. 20, No. 4, pp. 29-45, Oct.-Dec. 1998.
- [3] Bardeen, J., 1947, "Surface states and rectification at a metal- semiconductor contact", *Phys. Rev.* 71, 717-727.
- [4] US patent No. US3138743A (1959). URL: <https://patents.google.com/patent/US3138743>.
- [5] Gordon E. Moore: "Cramming more components onto integrated circuits". *Electronics*, Volume 38, Number 8, April 19, 1965.
- [6] Arute, F. et al. *Nature* 574, 505–510 (2019).
- [7] Gary J. Mooney et al. "Whole-device entanglement in a 65-qubit superconducting quantum computer" (2021). URL: <https://arxiv.org/abs/2102.11521>.
- [8] Richard P. Feynman. "Simulating Physics with Computers". *International Journal of Theoretical Physics*, Vol. 21, 1982.
- [9] 3-axis Inclinometer SCL3300 by Murata. URL: <https://www.murata.com/en-global/products/sensor/inclinometer/overview/lineup/scl3300>
- [10] Daniel Dux. "Towards the construction of rapidly rotating optical dipole traps". Bachelor thesis. University of Heidelberg, 2021.
- [11] "T-Schienenführungssystem" used in this experiment. URL: <https://www.igus.de/drylin/schienenfuehrung>

- 
- [12] Lilo Höcker. "Building up a modular Na-K quantum gas experiment". Master thesis. University of Heidelberg, 2019.
- [13] Jan Kilinc. "Starting a Na-K experiment for simulating quantum many-body phenomena". Master thesis. University of Heidelberg, 2019.
- [14] Data sheet of the NexTorr Ion-Getter pumps. URL: <https://www.saesgetters.com/sites/default/files/NEXTorr\Z\datasheets.pdf>
- [15] Data sheet of the UHV gauges by Leybold. URL: [https://www.leyboldproducts.com/media/pdf/65/f3/29/\\_POD\\_CP\\_060\\_EN\\_Measuring\\_Controlling\\_LV\\_2021.pdf](https://www.leyboldproducts.com/media/pdf/65/f3/29/_POD_CP_060_EN_Measuring_Controlling_LV_2021.pdf) pg.72f.
- [16] Friedhelm Serwane. "The setup of a Magneto Optical Trap for the preparation of a mesoscopic degenerate Fermi gas". Diploma thesis. University of Heidelberg, 2007.
- [17] C. B. Alcock, V. P. Itkin, and M. K. Horrigan. Vapor pressure equations for the metallic elements: 298-2500K. Canadian Metallurgical Quarterly, 23:309, 1984.
- [18] Armin Schwierk. Master thesis (preliminary). University of Heidelberg.
- [19] SAES Getters. URL: <https://www.saesgetters.com/>
- [20] Precision Glass Blowing. URL: <https://www.precisionglassblowing.com/custom-solutions/>
- [21] Telaztec. URL: <https://telaztec.com/technology.html>
- [22] K. M. Birnbaum. "Ultra-High Vacuum Chambers". Unpublished manuscript. California Institute of Technology, 2005.
- [23] Paolo Chiggiato. "Outgassing properties of vacuum materials for particle accelerators", 2020. URL: <https://arxiv.org/abs/2006.07124>
- [24] A summary on outgassing of various materials and Bake-out procedures to achieve ultra-high vacua by CERN: URL: [https://indico.cern.ch/event/569714/contributions/2303719/attachments/1336477/2159374/Lecture\\_2\\_Vacuum\\_Systems\\_-\\_V\\_Baglin\\_-\\_JUAS\\_2017\\_-\\_13\\_feb\\_2017.pdf](https://indico.cern.ch/event/569714/contributions/2303719/attachments/1336477/2159374/Lecture_2_Vacuum_Systems_-_V_Baglin_-_JUAS_2017_-_13_feb_2017.pdf)
- [25] Cleaning procedure for viewports recommended by Kurt J. Lesker company. URL: <https://www.lesker.com/newweb/feedthroughs/pdf/viewportscleaningprocedure.pdf>

- [26] Michael E. Gehm. "Preparation of an optically-trapped degenerated Fermi gas of  ${}^6\text{Li}$ : Finding the route to degeneracy". PhD thesis, Appendix A. Duke University, 2003.
- [27] G. Zürn, T. Lompe, A. N. Wenz, S. Jochim, P. S. Julienne, and J. M. Hutson. "Precise Characterization of  ${}^6\text{Li}$  Feshbach Resonances Using Trap-Sideband-Resolved RF Spectroscopy of Weakly Bound Molecules". *Phys. Rev. Lett.* **110**, 135301, 25 March 2013. Supplemental Material.
- [28] Gerhard Zürn. "Realization of an Optical Microtrap for a Highly Degenerate Fermi Gas". Diploma thesis. University of Heidelberg, 2009.
- [29] Eric Wille. "Preparation of an Optically Trapped Fermi-Fermi Mixture of  ${}^6\text{Li}$  and  ${}^40\text{K}$  Atoms and Characterization of the Interspecies Interactions by Feshbach Spectroscopy". PhD thesis. University of Innsbruck, 2009.
- [30] EMWorks is a software add-in for Solidworks to perform magnetic field simulations. An overview can be found here: <https://www.emworks.com/product/EMS>.
- [31] "Van Der Heijden Labortechnik GmbH". URL: <https://van-der-heijden.de/index.php/en/home-en.html>
- [32] Luca Xaver Bayha. "Emergence of Many-Body Physics in Two-Dimensional Few-Fermion Systems". PhD thesis. University of Heidelberg, 2020.
- [33] Ralf Arne Klemt. "Correlations from Microscopic to Macroscopic Quantum Systems: Interactions vs Indistinguishability". PhD thesis. University of Heidelberg, 2021.
- [34] Phillips, W., and H. Metcalf, 1982, "Laser deceleration of an atomic beam," *Phys. Rev. Lett.* 48, 596.
- [35] Phillips, W. D., J. Prodan, and H. Metcalf, 1985, "Laser cooling and electromagnetic trapping of neutral atoms," *J.Opt.Soc. Am. B* 2, 1751.
- [36] H. J. Metcalf and P. van der Straten, "Laser cooling and trapping of atoms," *J. Opt. Soc. Am. B* 20, 887-908 (2003).
- [37] Daniel A. Steck. "Rubidium 87 D Line Data", 2001. Summaries for other atom species like Caesium, Potassium or Sodium can be found at: <https://steck.us/alkalidata/>

- 
- [38] Tobias Tiecke. "Feshbach resonances in ultracold mixtures of the fermionic quantum gases  $^6\text{Li}$  and  $^{40}\text{K}$ ". PhD thesis. University of Amsterdam, 2009.
- [39] TA-SHG data sheet. URL: [https://www.toptica.com/fileadmin/Editors\\_English/11\\_brochures\\_datasheets/01\\_brochures/toptica\\_BR\\_Scientific\\_Lasers.pdf](https://www.toptica.com/fileadmin/Editors_English/11_brochures_datasheets/01_brochures/toptica_BR_Scientific_Lasers.pdf)
- [40] EDC-15 optical diffuser data sheet. URL: <https://www.rpcphotonics.com/wp-content/uploads/2016/05/Fact-Sheet-EDC-15-15132-A.pdf>
- [41] P. A. Murthy, D. Kedar, T. Lompe, M. Neidig, M. G. Ries, A. N. Wenz, G. Zürn, and S. Jochim. "Matter-wave Fourier optics with a strongly interacting two-dimensional Fermi gas". *Phys. Rev. A* **90**, 043611, 2014.
- [42] L. Asteria, H. P. Zahn, M. N. Kosch, K. Sengstock, and C. Weitenberg. "Quantum gas magnifier for sub-lattice-resolved imaging of three-dimensional quantum systems". 2021. URL: <https://arxiv.org/pdf/2104.10089.pdf>.
- [43] One possible fibre port cluster of Schäfter & Kirchhoff. URL: <https://www.sukhamburg.com/products/fiberoptics/multicube/systems/cluster/2.html>
- [44] Jan Hendrik Willibald Becher. "Towards Spin and Site-Resolved, Single-Atom Imaging of  $^6\text{Li}$  Atoms in a Multiwell Potential". Master thesis. University of Heidelberg, 2016.
- [45] Andrea Bergschneider. "Strong correlations in few-fermion systems". PhD thesis. University of Heidelberg, 2017.
- [46] Bergschneider, A. et al. "Spin-resolved single-atom imaging of  $^6\text{Li}$  in free space" *Phys. Rev. A* **97**, 063613, 2018. DOI: <https://doi.org/10.1103/PhysRevA.97.063613>
- [47] Special optics. URL: <https://specialoptics.com/products/microscope-objectives/objectives/customhighna/>



# Danksagung

An dieser Stelle möchte ich mich bei vielen Menschen bedanken.

Zuallererst bei Selim für die einmalige Möglichkeit in deiner Gruppe ein neues Experiment von Grund auf aufzubauen. Vielen Dank für das große Vertrauen, das du in mich setzt und für die vielen Gespräche und Diskussionen, die mich bis hierher und in den nächsten Jahren hoffentlich noch viel weiter bringen werden.

Und dann ein ebenso großes Danke an Philipp P. für die unzähligen Telefonate und Zoom Meetings während des Lockdowns und für alles was ich in den Diskussionen mit dir lernen durfte.

Außerdem möchte ich mich bei Matthias Weidemüller für die Übernahme der Zweitkorrektur bedanken und für die wertvollen Denkanstöße in den Meetings mit dir.

Bei der ganzen Ultracold Gruppe bedanke ich mich für die vielen schönen Momente mit euch und bei Philipp L. und Carl für diverse Schach und Dart Partien, von denen es in Zukunft hoffentlich noch einige mehr geben wird. Ich freue mich auf die nächsten Jahre mit euch allen!

Insbesondere möchte ich mich noch bei Armin bedanken dafür, dass du die turbulente Anfangsphase des Experiments mit mir durchgestanden hast.

Ein großes Dankeschön auch an alle, die diese Arbeit Korrektur gelesen haben.

Und dann bedanke ich mich noch bei all meinen Freunden in Heidelberg für die vielen lustigen Abende und vor allem bei meinen Mitbewohnern Jan und Josef dafür, dass ich nach langen Arbeitstagen immer gerne nach Hause komme.

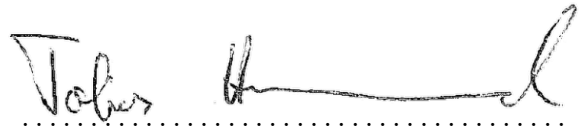
Zuletzt möchte ich meiner Familie danken für eure bedingungslose Unterstützung und für die Zeit mit euch, die ich immer sehr genieße.



Erklärung:

Ich versichere, dass ich diese Arbeit selbstständig verfasst habe und keine anderen als die angegebenen Quellen und Hilfsmittel benutzt habe.

Heidelberg, den 30.08.2021

  
.....